UNIVERSITÀ DEGLI STUDI DI TRIESTE

XXXVI CICLO DEL DOTTORATO DI RICERCA IN

NANOTECHNOLOGY

Tungsten-Carbon Based Nanostructured Hybrid Materials

Settore scientifico-disciplinare: **FIS/03 Fisica della Materia**

DOTTORANDA
AYESHA FAROOQ

COORDINATORE
PROF. ALBERTO MORGANTE

SUPERVISORE DI TESI
DR. CINZIA CEPEK

CO-SUPERVISORE DI TESI
DR. SIMONE DAL ZILIO

ANNO ACCADEMICO 2022/2023

UNIVERSITÀ DEGLI STUDI DI TRIESTE

XXXVI CICLO DEL DOTTORATO DI RICERCA IN

NANOTECHNOLOGY

Tungsten-Carbon Based Nanostructured Hybrid Materials

Settore scientifico-disciplinare: **FIS/03 Fisica della Materia**

DOTTORANDA
AYESHA FAROOQ

COORDINATORE
PROF. ALBERTO MORGANTE

SUPERVISORE DI TESI
DR. CINZIA CEPEK
Cinzia Cepek

CO-SUPERVISORE DI TESI
DR. SIMONE DAL ZILIO

ANNO ACCADEMICO 2022/2023

ABSTRACT

The aim of this thesis was the development of new Carbon-Tungsten nanostructured hybrid materials that potentially can be used in many applications as, for example, first-wall material in fusion reactors, CO_2 reduction, H_2 production, chemiresistor to many hazardous and toxic gases. All the work has been performed in many laboratories of the IOM-CNR Institute, and it was partially funded by the energy company ENI.

We produced many carbon nanostructures (CNs), including isolated single wall carbon nanotubes (SWCNTs), sp^2 dendritic 3-dimensional thin films, carbon nanofibers and CNTs with controlled length and density, that were used as substrate to synthetize novel carbon/tungsten (C/W) hybrids. Our results show that the W deposition via DC magnetron sputtering (DCMS) allows to preserve the pristine CN's morphology, thus proving an effective method to obtain different hybrid carbon/tungsten nanostructures (C/W NS). In the case of CNT forest, depending on tube density and thickness, W can uniformly wet the tubes, or can form a not-uniform coating, up to the formation of a W film on top of the CNTs carpet. The use of the supersonic cluster source AMPHIRO allowed to obtain nanostructured tungsten oxide (WO_x) films (NS-WO_x), whose building blocks were clusters of dimensions of less than 1 nm. In-situ photoemission has shown that, by using the appropriate gas mixture during cluster synthesis, the NS-WO_x films present a variety of different oxidation states, not stable in conventional systems. When deposited on CNTs, NS-WO_x preserve their nanostructured nature, forming a sort of beaded necklace that, to our knowledge, has never been observed in literature.

As preliminary work, we measured the response to ethanol (EtOH) vapours of three significant hybrids for possible use as chemiresistors, monitoring their electrical resistance variation during exposure in UHV to EtOH vapours at room temperature (RT). Our results indicate that W deposition via DCMS on a CNTs forest suppresses the well- known ability of CNTs to respond to EtOH as p-type material. The highly defected and porous NS-WO_x film shows higher sensitivity than the CNTs forest and it behaves as p-type material. The sample with the highest sensitivity was the hybrid formed depositing NS-WOx on a CNTs forest. Beside both the components behave as p-type semiconductors, the new material shows a n-type behaviour, which may be ascribed to a charge transfer between the NS-WO_x and the CNTs. The possibility to obtain n-type doping in CNTs is an important open issue in literature which has important technological implications. The charge transfer between the highly reactive NS-WO_x and the CNTs could not be confirmed, because of the NS-WO_X thickness was higher than the surface sensitivity of the techniques here used (XPS and UPS). Further investigations are scheduled to disentangle this point.

Last but not least, the most promising hybrids are planned to be studied for hydrogen retention and will be exposed to the GyM linear reactor of ISTP-CNR (Milan) to be tested as first wall material in a fusion reactor.

Sommario

Lo scopo di questa tesi è lo sviluppo di nuovi materiali ibridi nanostrutturati basati su Carbonio e Tungsteno per il loro potenziale utilizzo in applicazioni quali, ad esempio, materiali di prima parete nei reattori a fusione, riduzione di CO_2, produzione di H_2, chemiresistori per molti tipi di gas pericolosi e tossici. Il lavoro è stato svolto nei laboratori dell'Istituto IOM-CNR, ed è stato parzialmente finanziato dalla compagnia energetica ENI.

Si sono prodotte molte nanostrutture di carbonio (CNs), inclusi SWCNT, film sottili 3-D dendritici sp2, CNF e CNT con lunghezze e densità controllate, che sono state utilizzate come substrato per sintetizzare nuove nanostrutture di W ed ibridi C/W. I nostri risultati mostrano che la deposizione di W tramite DCMS consente di preservare la morfologia iniziale delle CNs, dimostrandosi un metodo efficace per ottenere ibridi C/W NS. Nel caso di foresta di CNT, a seconda della densità e dello spessore dei tubi, il W può bagnare uniformemente i tubi, oppure formare un rivestimento non uniforme, fino alla formazione di una pellicola di W sopra il tappeto di CNT. L'uso di una sorgente di cluster supersonica ha permesso di ottenere film WOx nanostrutturati (NS-WO_x), i cui elementi erano cluster di dimensioni inferiori a 1 nm. La fotoemissione *in-situ* ha dimostrato che, utilizzando un'appropriata miscela di gas durante la sintesi, i film NS-WO_x presentano una varietà di stati di ossidazione, non stabili in sistemi convenzionali. Se depositati sui CNT, gli NS-WOx preservano la loro natura nanostrutturata formando una sorta di collana di perle, struttura che, a nostra conoscenza, non è stata osservata in letteratura.

Come lavoro preliminare, si è misurata la risposta a vapori di EtOH di tre ibridi significativi per un possibile utilizzo quali chemiresistori, monitorando la variazione della loro resistenza elettrica durante l'esposizione in UHV a vapori di EtOH a RT. I nostri dati indicano che la deposizione di un film di W continuo tramite DCMS sui CNT sopprime la ben nota capacità dei CNT di rispondere all'EtOH come materiale di tipo p. Il film NS-WOx altamente difettoso e poroso mostra una risposta a RT, con una sensibilità maggiore della foresta di CNT e si comporta come materiale di tipo p. Il campione che ha mostrato la maggiore sensibilità è l'ibrido formato dalla deposizione di NS-WOx su una foresta di CNT. Benché entrambi i componenti si comportano come materiali di tipo p, il nuovo materiale mostra un comportamento di tipo n, che può essere attribuito ad un trasferimento di carica tra NS-WOx e CNT. La possibilità di ottenere CNT drogati n è un importante problema aperto in letteratura con importanti implicazioni tecnologiche. Il trasferimento di carica non è stato confermato, poiché lo spessore di NS-WOX era superiore alla sensibilità superficiale delle tecniche disponibili (XPS e UPS), si prevedono ulteriori indagini per chiarire questo punto.

Infine si prevede di studiare la ritenzione di idrogeno degli ibridi più promettenti e di esporli al reattore lineare GyM dell'ISTP-CNR per essere testati come materiale di prima parete in un reattore a fusione.

ACKNOWLEDGEMENT

All praise to Allah, to Whom belongs all that is in the heavens and all that is on earth.

At this point, when I am submitting my thesis, it comes to my realization that this PhD journey could not be achieved by just academic rigor; it required a network of firm support, mentor ship, and encouragement. Therefore, I find myself blessed to have crossed paths with amazing individuals and institutes who have played a major role in making this journey possible.

Firstly, I would like to express my gratitude to my esteemed supervisors, Dr. Cepek and Dr. Dal Zilio.

Dr. Cepek, thank you for being the catalyst in my dream come true. Your generosity, support, and invaluable guidance have been instrumental in shaping my journey. I want to express my sincere appreciation for your patience and believing that this old lady (of course me) will be able to accomplish this task.

Dr. Dal Zilio, I am grateful for your guidance, scholarly insight, and support during my PhD. Despite your multiple engagements and busy schedule, you always took out time whenever I asked for your guidance.

Dr. Stredansky, I appreciate you for your valuable and able guidance to complete this difficult task.

I would like to extend my gratitude to the supervisory committee: Prof. Morgante, Prof. Baraldi and Dr. Rubini, for your time and effort that you dedicated in providing feedback on my work. Your inputs have contributed significantly to my growth as a scholar.

I would like to acknowledge ENI, for partially funding my project, and giving me the opportunity to work in a conducive academic environment. In addition to that I would like to thank CRN-IOM for providing cutting edge resources that facilitated me in completion of my project. Furthermore, elettra and specially Dr. Goldoni for letting me use the CVD facility. Finally, my institutes, University of Trieste, for selecting me and giving me the opportunity to become a proud alumna of this prestigious institute and COMSATS University of Islamabad, for granting me study leave to pursue my goal.

I would like to extend my appreciation to Ms. Rosita and Ms. Ottavia, for their patience and guidance for the administrative matters related to university.

To my friends, even though the list is long, I would like to mention some very special ones. Nour, thank you, you kept me grounded. Elisabetta, showed me around, introduced me to some lovely people, made my stay memorable. Fatima, for long walks and encouragement when I am not at my best. Valeria for always guiding me and supporting me. Teresa, for worrying about me and caring for me. Sumati, for listening and bearing my exaggerated reactions and responses. Cinzia, for being so sweet. Aline, for boosting my Morales. Dr. Grazioli, Dr. Polewcyzk and Dr. Beltrami for their guidance. Lastly, Dr. Ali and Dr. Bhardwaj for teaching me how to handle the equipment during my initial days in lab. All of you have supported me and motivated me during both challenging and rewarding times of my journey. I will cherish every moment spent with you all.

Finally, to my family- the unsung heroes of this academic saga. My mother, for supporting my decision and being available for my kids. Zahid, for letting me chase my dream and took the responsibilities of being both father and mother to the kids for three years. Usman and Beenish, for taking care of kids when Zahid was not around. Umer, for his motivational calls and texts. A. Raffay for helping me with technical software related advice. Most importantly my kids, Eshaal and Hamood for letting me stay away for three years and pursue my dream, I love you both to moon and back.

If my father and my grandmother (jimmy) can see me from above, I want you to know that I miss you both now more than ever.

In short, this dissertation would have not been possible without the collaborative efforts of an extraordinary community of mentors, colleagues and loved ones. All the individual mentioned, has left a permanent mark on this journey, and for that I am humbly grateful.

Contents

Acronyms

AFM	Atomic force microscopy
ALD	Atomics layer deposition
Al_2O_3	Aluminium oxide
BE	Binding energy
C_2H_2	Acetylene
CCVD	Catalytic chemical vapour deposition
CNF	Carbon nanofiber
CNs	Carbon nanostructures
CNTs	Carbon nanotubes
CVD	Chemical vapour deposition
DBTT	Ductile brittle transient temperature
DCMS	Direct current magnetron sputtering
e-beam	Electron beam
EtOH	Ethanol
FIB	Focused ion beam
HC	Hydrocarbon
HiPIMS	Hi power impulse magnetron sputtering
HM	Hybrid material
NC	Nano clusters
NS	Nanostructures
PE	Photoemission
PFW	Plasma facing wall
PMSC	Pulse micro-plasma cluster source
PVD	Physical vapour deposition
RF	Radio frequency
rGO	Reduced graphene oxide
RT	Room temperature
SBCS	Supersonic beam cluster source
SECO	Secondary electron cut off region
SCS	Supersonic cluster source
SEM	Scanning electron microscopy
Si	Silicon
SiO_2	Silicon dioxide
SWCNT	Single wall carbon nanotubes
TEM	Transmission electron microscopy
UHV	Ultra-high vacuum
UPS	Ultraviolet photoemission spectroscopy
VB	Valance band
W	Tungsten
WF	Work function
WO/WO_x	Tungsten oxide
XPS	Xray photoemission spectroscopy
XRD	Xray diffraction

Introduction -Abstract

Human-induced climate change is causing extensive adverse effects on nature resulting in suffering of billions of human beings and animals. Due to excessive pollution mother nature is showing her resentment in the form of increased heatwaves, floods, and droughts [1]. As a result, many plants and animals' species are getting extinct. The quest for improving quality of life is ever increasing. Technological advancements have resulted in rising demand for portable, fit-in-a-pocket, light, and compact devices. The portable nature of such gadgets makes them user friendly. Most used gadgets like mobile phones, smart watches, tabs, laptops, sunglasses and many more gain popularity in public based on their size, weight, and efficiency. All these goals are being attained by reducing the size of the components of the gadget and making it effective. Nanotechnology is a valuable option that is currently explored by various industries [2], as with significantly reduced utility of raw material, nature could be better preserved. Nanotechnology is a way forward as it would ensure technological advancements and cost effectiveness whilst preserving eco-friendly environment.

In this thesis, the well-known ability to tune the morphology of carbon-based materials via catalytic CVD has been exploited to use them as template to synthesize several different composites and hybrids based on Carbon Nano-structures (CNs) and Tungsten (W). The final aim was the development of these new materials for many practical applications, as, for example, first-wall material in fusion reactors [3], CO_2 reduction [4], H_2 production, production of sensors to many hazardous and toxic gases, like CO, H_2, H_2S [5,6]. All the work has been performed in different laboratories of the IOM-CNR Institute, and it was partially funded by the energy company ENI.

The synthesises have been done by employing many states of the art growth techniques as e-beam evaporation, DC magnetron sputtering and chemical vapour deposition (CVD) and a supersonic cluster beam source (AMPHIRO). AMPHIRO has allowed to synthesize tungsten nanoclusters that do not naturally exist in nature and that to our knowledge it has not yet been documented in literature or in industrial applications. To comprehensively analyse these materials, cutting edge technologies were used for both in-situ and ex-situ measurements allowing a chemical and morphological characterization of all the synthesized materials, which includes X-ray photoemission (XPS), Ultra-violet photoemission spectroscopy (UPS),

scanning electron microscopy (SEM), and other techniques, which will be discussed later in the thesis.

The main purpose of synthesized hybrid materials is to be applied in the first wall of fusion reactor, but they can also be used as ethanol gas sensors.

This thesis is organized as follow:

In **Chapter 1**, a brief overview of literature related to tungsten (W) and tungsten oxide (WO_x), encompassing their synthesis techniques and diverse applications, will be presented. Further in this chapter, the discussion will focus on carbon nanotubes/ carbon nanostructures (CNTs/CNs), their synthesis and applications. Then, a thorough literature review will be presented related to hybrid material (HM) based on CNTs/CNs and W/WO_x, their synthesis techniques and applications.

Chapter 2 provides an overview of the experimental techniques used in this research work. In each section, the basic concepts and the importance regarding the specific technique will be discussed. The growth techniques employed are discussed followed by an introduction to the tools used for characterization of the sample. In the last part of the chapter, we will go through the details of the experiments performed to prepare the samples reported in this dissertation.

Chapter 3 will focus on characterization of the obtained CNs (synthesis described in chapter 2) to serve as a template for W/C hybrid material. This Chapter is divided into two main parts: The first part encompasses the characterization of CNs grown on (250 nm) SiO_2/Si commercially available substrate and Nickel (Ni) as the catalyst. The second part incorporates the characterization of CNTs synthesized on (250 nm) SiO_2/Si commercially available substrate and (7.5 nm) Al_2O_3/Si substrate with iron (Fe) as the catalyst.

Chapter 4 encompasses the morphological and chemical characterization of the W/WO_x film grown on Si(100) substrate via DCMS and supersonic cluster source.

Chapter 5 In this chapter we will discuss the characterization of hybrid materials (HM) prepared as a combination of CNs (CNs and CNTs) as template with tungsten coating. The chapter is divided into different sections, initially based on type of CNs (CNs or CNTs) used as templates. In addition to that, the division will be based on type of techniques used for tungsten deposition (DCMS or SBCS).

Chapter 6 presents the application of the samples prepared for this research work. It includes the electrical response to EtOH vapors of three significant samples and two reference samples, described in the previous chapter, for their possible application as chemiresistors.

Reference

[1] Y. Zhao, Z. Weng, H. Chen, J. Yang, Analysis of the evolution of drought, flood, and drought-flood abrupt alternation events under climate change using the daily SWAP index, Water (Switzerland) 12 (2020). https://doi.org/10.3390/w12071969.

[2] A. Ranzoni, M.A. Cooper, The Growing Influence of Nanotechnology in Our Lives, in: Micro and Nanotechnology in Vaccine Development, Elsevier, 2017: pp. 1–20. https://doi.org/10.1016/B978-0-323-39981-4.00001-4.

[3] J. V. Vas, J.Q. Pan, N.L. Wang, J.H. Xu, R. Medwal, M. Mishra, J.Y. Pae, M. V. Matham, L.C.K. Paul, R.S. Rawat, Plasma processed tungsten for fusion reactor first-wall material, J Mater Sci 56 (2021) 10494–10509. https://doi.org/10.1007/s10853-021-05917-y.

[4] F. de Souza, R.K. Gupta, Nanotechnology for CO2 reduction: progress and perspective, in: Revaprasadu Neerish, Dilshad Khan Malik (Eds.), Nanoscience, Royal society of chemistry, 2022: pp. 177–197. https://doi.org/10.1039/9781839167218-00177.

[5] S. Yang, G. Lei, H. Xu, Z. Lan, Z. Wang, H. Gu, Metal oxide-based heterojunctions for gas sensors: A review, Nanomaterials 11 (2021). https://doi.org/10.3390/nano11041026.

[6] S. Wang, Y. Kang, L. Wang, H. Zhang, Y. Wang, Y. Wang, Organic/inorganic hybrid sensors: A review, Sens Actuators B Chem 182 (2013) 467–481. https://doi.org/10.1016/j.snb.2013.03.042.

Chapter 1

Introduction

Commencing this section, a brief overview of literature related to tungsten (W) and tungsten oxide (WO_x), encompassing their synthesis techniques and diverse applications, will be presented. Later in this chapter, the discussion will shift to carbon nanotubes/ carbon nanostructures (CNTs/CNs), their synthesis and applications. Subsequently, a thorough literature review will be presented related to hybrid material based on CNTs/CNs and W/WO_x, their synthesis techniques and applications.

1.1 Tungsten/Tungsten Oxide based nanomaterials

Tungsten (W) originates from a Swedish term 'tung sten' meaning 'heavy stone'. W, because of its exceptionally high melting point of 3420 °C has many applications. It is considered an important strategic metal based on its distinctive characteristics and economical significance. Industries demanding materials with high strength, density, temperature, and wear resistance makes more use of tungsten [1]. Therefore, in industries like mining, construction, aerospace, defence, fusion energy etc, tungsten is widely used. Tungsten, in most of its applications is used in the form of carbide [2], sulphide [3], alloy [4], and oxide [5]. Since 1900, tungsten and its oxides have been studied, but recently there has been an upsurge in the scientific research related to this transition metal oxide and its alloys with numerous stoichiometries showing suitability for many applications. We will briefly discuss the synthesis techniques to attain these nanostructures and their applications.

1.1.1 Methods to obtain Nanostructured Tungsten and Tungsten oxides (W/WO_x)

Nano-structuring has become a powerful technique for harnessing the complete capabilities of metal/metal oxides. W/WO_x are exceptional materials that have been extensively studied for their mechanical strength, conductivity, photocatalysis, photochromic and sensing properties[6]. Various approaches for the syntheses of nanostructured W/WO_x have been employed using both vapor and liquid phase-based methods. In this section a concise overview of the most common synthetic methods will be provided.

There are two main categories in which we can divide the synthesis process:

1. Vapour phase
2. Liquid phase

Vapour phase

This category involves a broad spectrum of techniques for material synthesis. In general, this comprehends, the condensation of vaporized source material onto the specified substrates. For the synthesis of nanostructured W/WO$_x$, physical vapor deposition (PVD) is generally used. The PVD technique can be entirely physical, starting with the W/WO$_x$ source material in the form of a solid target or powder. The material is evaporated (sublimed) using various techniques like, ion bombardment, heat, electron beam, or laser irradiation. By controlling the process parameters, the evaporated species can condense into nanostructured forms with specific dimensions, crystal structures, and nanoscale morphology.

For the growth of WO$_x$ it is not necessary that the source is WO$_x$. If the source is metallic W in the form of powder or filament, oxygen in the form of a gas or other oxidants are added to the vapor to facilitate the formation of WO$_x$. It is worth mentioning that material synthesized via PVD is WO$_x$ rather than WO$_3$. The colour of the deposited material serves as a reliable marker of the material's stoichiometry. Normally, post-annealing processing can be employed to achieve the desired oxygen content, crystal phase and stoichiometry [7].

References for some of the articles used to synthesize W/WO$_x$, are summed in the following table:

Technique	**Type of structure**	**Reference**
Vapour phase technique	W^0 nanowires	[8]
PVD	WO_3 porous thin films	[9]
PLD	$W_{18}O_{49}$ and WO_3 Nanowires	[10]
Hot filament method	Hot wire WO_x film	[11]
Thermal vapour deposition	WO_{3-x} nanorods	[12]

Table 1. 1 Vapour phase techniques used to synthesis W/WO$_x$ films and nanostructures

Liquid phase synthesis

It is a cost-effective technique. In comparison to the vapor phase syntheses, it gives a better control on material morphology. It can be operated at low temperature, hence during deposition the quality of the substrate with low heat tolerance is not affected. In the past decades, many routes have been introduced for the synthesis of WO$_x$, in different nanostructured forms. Four of the most widely used techniques are hydrolysis, condensation, etching, and oxidation [7].The methods that are used to deposit nanostructured film are solgel, templating, hydrothermal, electrochemical anodization, and electro- deposition. Some of the synthesized films and NS of W/WO$_x$, using the liquid phase synthesis techniques are listed in table 1.2.

Technique	Type of structure	Reference
Hydrothermal treatment	WO_3 powder	[13]
Solgel	Amorphous WO_x thin film	[14]
Solvothermal reaction	$W_{18}O_{49}$ NS	[15]
Electrochemical deposition	Nanocrystalline WO_3	[16]
Electrochemical anodization	WO_3 flower like NS	[17]

Table 1. 2 W/WO_x film and NS synthesized using liquid phase synthesis techniques

1.1.2 Applications of W/WO_x

Naturally as W/WO_x is a versatile material, its applications can be found in various fields. The main areas of research are fusion reactors, electrochemistry, photo and electro chromic properties, microbiology, fireproof textile, Xray screens, devices, catalysis, sensors and many more [6].Ultra-high purity tungsten raw powder has been used in the production of electrodes for high intensity discharge (HID) lamps for increased lifetime by avoiding outgassing impurities [1,18]. High temperature stability, thin films of tungsten and its alloys (W-Ti, W-Si) are the preferred choice in semiconductor devices to develop interconnects, electrodes, and barrier metals [1].Tungsten due to its strength is the most used material in mining and cutting tools. Tungsten carbide is an important material used in end mills, gun drills, and twist drills [2]. Some other reported applications of tungsten and its alloys are in armour piercing [19], gyroscope rotors [20], and advanced medical instrumentation [21].

Importance of tungsten in fusion reactor: Fusion is a process in which two small nuclei fuse together to give a heavier nucleus and immense amount of energy. Fusion reaction is the reaction that takes place in the sun.

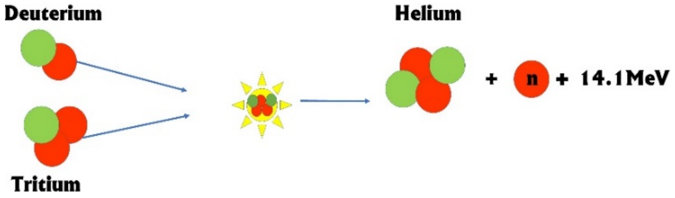

Figure 1. 1 Fusion reaction of deuterium and tritium resulting in helium and immense amount pf energy

The development of fusion energy is something every scientific community dream of. For fusion reaction to take place, high temperature plasma is generated, which enables hydrogen nuclei to fuse together, producing high energy alpha particles and energy in the form of free neutron. However, there are several barriers that cause a hindrance in this development. One of the problems is the stability of the plasma facing wall (PFW). Plasma facing materials must have good thermal properties, erosion resistance, resistant to hydrogen blistering and bubbling, and mechanical properties. Different materials and their alloys have been tested, but tungsten is showing promising results [22]. Tungsten due to its properties mentioned above, is a strong candidate material for plasma facing wall. Due to its ductile to brittle transition temperature (DBTT), its application is hindered. Various tungsten alloys, composites, and hybrid materials are being tested to make tungsten viable for the PFW. Some already reported applications of tungsten in fusion application are listed in the table 1.3

Synthesis technique	**Materials used**	**Problem addressed**	**Ref**
Powder Metallurgy	W-2Y_2O_3 composite	DBTT	[23]
Plasma spraying	Nanocrystalline W	Wall erosion	[24]
Mechanical alloying and spark plasma sintering	W, Ta and W-Ta composite	Blistering	[25]
Mechanical alloying/sintering	W-Ti alloy dispersed with $Y_2Ti_2O_7$	Mechanical properties	[26]
Spark plasma sintering	TiC/W	Thermal conductivity and tensile strength	[27]
Wet chemical process and spark plasma sintering	Pr_2O_3 doped W	Thermal conductivity and tensile strength	[28]
DC magnetron sputtering/ CVD	Carbon coated interface in W fibre	Brittleness	[29]
Combustion synthesis with centrifugal infiltration	W/Cu	PFW material transition material between PFW and heat sink	[30]
Sintering	W-V composite	Mechanical strength	[31]

Table 1. 3 Reported literature on W related advancements for fusion reactor

Both metallic tungsten and its oxide have proved its significance in various industrial and scientific applications. Some of the reported application of WO_x are discussed:

Fasquelle et al., reported WO_3 thin film, deposited on Si substrate. They post annealed the sample at two different temperatures, which resulted in different sizes of WO_3 grains. These samples where then used to detect H_2S, for different concentrations at 350 °C operating temperature [32], and electrochromic properties of WO_3 [33]. It has also been used as a photo anode for water splitting experiments [34].

With the advancement in science and technology WO_x has been investigated for applications in the field of sensors, batteries, renewable energy, microbiology, and environmental sciences [35].

The broad range of applications dedicated to WO_x suggests that due to different stoichiometry it can have different values of bandgap which reflects in interesting optical and electrical properties, chemical stability, and crystalline structures. Nano structuring of WO_x is used to optimize its properties for specific applications [35].

In this thesis we have used the prepared samples to detect ethanol at room temperature. Therefore, our focus would be on the gas sensing properties of WO_x. The basic principle that is used in most of the gas sensors are chemi-resistive method (detailed discussion will follow in section (6.1)). Intrinsically WO_3 is n-type semiconductor but sub stoichiometric WO_x acts as a p-type semiconductor. When WO_3 is exposed to an oxidizing gas (NO_2) or a reducing gas (Ethanol), the resistance will increase or decrease respectively [36]. WO_x use in the field of gas sensor is one of the most common applications. In the table 1.4, some of the gas sensor reported are given with their synthesis method, structure of WO_x, response, operating temperature, and concentration of the gas.

Sr. No.	**Synthesis process**	**Structure**	**Gas**	**Conc. ppm**	**Operating temp**	**Response (to gas)**	**Ref.**
1	Hydrothermal	NF	Ethanol	100	350 °C	62	[36]
2	CVD	WO_x	H_2	4000	100 °C	608	[37]
3	Calcination	Nano-crystallites	NO_2	10	300 °C		[38]
4	Solvothermal	Urchin	Ethanol	100	RT	3	[39]
5	Colloidal process	QDs	H_2S	50	80 °C	57	[40]
6	HFCVD	Thin film	H_2	100	250 °C	87%	[41]
7	sol gel	Anhydrous and hydrous NS WO_3 thin films	NO_2	9.9	175 °C	11	[42]

Table 1. 4 Table showing a brief literature review of the work already being done on WO_x gas sensors. In some of the work response is calculated using R_g/R_a, whereas in some % response is calculated using $((R_g - R_a)/ R_a) *100$

WO_x has been used frequently for NO_2 detection.

1.2 Carbon Nanotubes: growth and application

Carbon based (C-based) materials are one of the most investigated materials in the last decades in the field of science and technology, especially nanotechnology. Due to sp^2 and sp^3 hybridization, pure carbon can assume many different allotropes, presenting many different chemical and physical properties, e.g., diamond, graphite, graphene, nanotubes, nanowires, nano-onion rings, nanoparticles, rods, fullerene, and nano diamond, as shown in figure 1.2 [43].

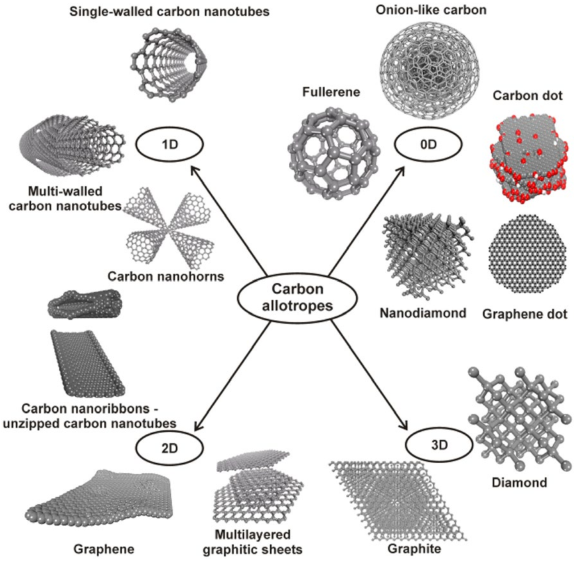

Figure 1. 2 C-based materials based on dimensionality [44]

CNTs are made up of carbon atoms arranged in repeated patterns of hexagon and pentagons with a diameter of 3- 15 nm, as shown in Fig.1.3 and 1.4 (left) below. CNTs belong to the subfamily of fullerenes which is an allotrope of carbon. Due to their hollow structure, high surface to volume ratio, and geometry CNTs are considered favourable for applications in electronic devices, gas sensors, batteries, medicine etc.

Figure 1.3 displays vector structure classification to show the possible ways to roll a hexagonal sheet of graphite to form a CNT. n and m (n,m) are the integers used to determine the chiral vector (**C**). Selecting two atoms on the sheet, considering one as origin. **C** is directed from the first atom towards the second atom. It is given by the following relation:

$$C = na_1 + ma_2$$

Equation 1. 1

Where $\mathbf{a_1}$ and $\mathbf{a_2}$ are the unit cell vectors for graphene sheet. The direction of CNT axis and chiral vector are perpendicular to each other. In addition to that, the CNT's circumference is given by the length of **C.**

$$c = \left| C \right| = a\sqrt{n^2 + nm + m^2}$$

Equation 1. 2

Where a is related to ‘a_{cc}’ the C-C bond length and expressed by the following relation:

$$a = |a_1| = |a_2| = a_{cc}\sqrt{3}$$ Equation 1. 3

using c, we can also calculate the diameter of the CNTs as:

$$d = \frac{c}{\pi}$$ Equation 1. 4

Chiral angle (θ) is between the zigzag direction and the chiral vector. Mathematically it is expressed as:

$$\theta = tan^{-1}(m\sqrt{3})/\,(m + 2n)$$ Equation 1. 5

From the chiral vector and angle, we can see from figure 1.3 below, that we can have three different types of CNTs as zigzag when $m = 0$ and $\theta = 0°$, armchair when $m = n$ and $\theta = 30°$, and chiral when $m \neq n$ and ($0° < \theta < 30°$). The chiral vector enables the determination of whether the CNTs are metallic or semi-conducting. Theoretically, all armchair CNTs have metallic properties and for others (zigzag and chiral tubes) if $|n - m| = 3*i$ (where i is an integer) is satisfied, CNTs are metallic, otherwise they are semiconducting [45].

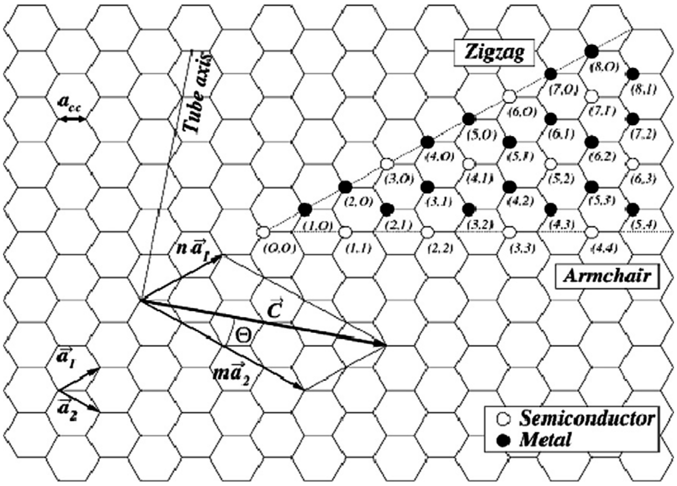

Figure 1. 3 Classification of CNTs structures using 2D graphene sheet diagram [45]

For example zigzag tubes (n,m) with values (3,0), (6,0) etc will be metallic, whereas for chiral (12,3), (15,6), etc will show metallicity.

The categorization of CNTs as metallic or semiconducting depends upon their structural configuration. Armchair CNTs are metallic as there is no bandgap between the valance and conduction band. In contrast, two third of the zigzag and chiral CNTs are semiconducting due to the existence of a gap between the bands[46,47].

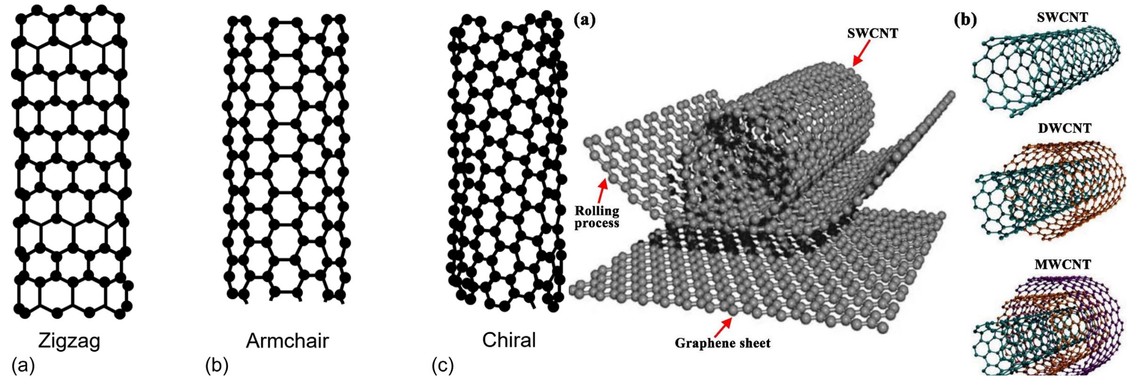

Figure 1. 4 (left) a. Zigzag, b. Armchair, c. Chiral type CNTs, (right) a. Schematic of how a graphene sheet rolls up to form CNTs, b. Types of CNTs, based on no. of tubes and their diameter [46]

CNTs are distinguished from one another by the number of walls, shown in figure 1.4 (right); single wall carbon nanotubes (SWCNTs) have 1 – 2 nm of diameter, Double wall carbon nanotubes (DWCNTs) consist of two walls, or two concentric tubes. The inner tube with diameter 1-3 nm and the outer tubes having 2 – 4 nm diameter, Multiwall carbon nanotubes (MWCNTs) consist of more than two concentric tubes. The arrangement of the tubes can be either multiple tubes arranged in concentric order, or like one big sheet being rolled up. The former is called Matryoshka doll model, and the latter is called a parchment model. The outer radius lies in the range of 2 nm to 30 nm [48].

1.2.1 Synthesis techniques for CNs

There are three different ways to synthesis CNTs/CNs:

Laser ablation: It is the process in which material from a solid or liquid surface is removed by irradiating it with laser. Laser ablation is environment friendly and is a top-down approach of preparing nano materials like quantum dots, nanotubes, nanowires, and core shell nanoparticles [48].

Arc discharge: It is the oldest technique for preparing versatile nanosized materials, especially for synthesising carbon-based nanostructured materials, like fullerenes and CNTs. Two electrodes are placed in a chamber which is either filled with an inert gas or are immersed in liquid. The anode contains the powdered carbon precursor, whereas the cathode is of pure graphite. The distance between the electrodes is 1-2 mm to maintain a steady discharge. The discharge generates high temperature, resulting in sublimating carbon precursor, which is then deposited on the cool end of the anode, forming CNs [48]. Iijima et al. reported revolutionary CNTs synthesized by arc discharge method [49].

Chemical vapor deposition (CVD): CVD is the most used technique for the synthesis of CNs/CNTs, because it is easy to handle and applicable to large scale growth, as compared to the other two techniques mentioned above. CVD is the technique widely used to facilitate reactions involving gaseous reactants. In this method one or more volatile precursors are conveyed into the reaction chamber. Typically, these volatile precursors undergo decomposition upon encountering a heated substrate surface located within the reaction chamber. This decomposition process produces specific chemical by-products, which are then removed from the chamber along with any unreacted volatile precursors. It is advantageous as it allows controlled and selective growth of CNs on substrate as well as in bulk at relatively low temperature as compared to other techniques. (Detailed discussion on CVD can be found in chapter 2) [48].

For the growth of CNs for this research, we have used catalytic CVD (CCVD) method. In CCVD a catalyst is used to reduce the cracking temperature of the precursor and to facilitates the growth of CNs.

Transition metals (Ni, Fe, Co) are frequently used as **catalyst** for the growth of CNTs [50]. These metals have shown high diffusion rate for C and high C solubility at elevated temperatures [51,52]. Subjecting the catalytic film to a reducing gas such as hydrogen or ammonia at elevated temperatures yields several significant effects. Firstly, it leads to reduced island dimensions and a narrower distribution of these islands compared to the effect of mere film annealing. Furthermore, this process reduces the oxidized catalyst NPs. Both effects collectively enhance the efficiency of the catalyst film for CNTs growth [51,52].

The choice of **carbon source** and its vapour pressure can affect the growth rate of CNTs and the lifetime of the catalyst. There are several reported C sources, but the most used are acetylene [53], ethylene [54], methane [55], and CO [56].

Synthesis of CNTs have been achieved through different methods using various precursors and catalysts. For instance, CNTs have been synthesized at 700 °C from catalytic decomposition of C_2H_2 in presence of Fe [57]. Furthermore, cyclohexane and C_{60} were also used as precursors to synthesize MWCNTs [58,59]. In another work, SWCNTs were synthesized at 1200 °C through the disproportionation of CO, with Mo nanoparticles as catalyst [60]. Ethanol has gained popularity for its ability to produce high purity SWCNTs when reacts in the presence of Co-Fe catalyst and zeolite support layer [61]. Ethanol grown

CNTs are almost amorphous C free because of the etchant quality of the OH radical present [62].

In general, CVD growth between 600 – 900 °C, results in MWCNTs, however SWCNTs are usually attained at higher temperature (900 – 1200 °C). This temperature difference suggests that higher energy is required for the formation of SWCNT growth, which in turn limits the choice of precursors (CO, methane, etc) for SWCNTs synthesis. Some precursors show stability at higher temperature (CO, methane, etc), while others become unstable at higher temperatures (C_2H_2, C_6H_6, etc) [63].

Name of precursor gas	**Cracking temperature (°C)**	**Cracking temperature in presence of Ni (°C)**	**Cracking temperature in presence of Fe (°C)**
Acetylene	**700**	**350**	**600**
Methane	1000	500[64]	750[65]
Ethane	900		750[66]

Table 1. 5 cracking temperature of gases without and with catalyst, highlighted gas was the working gas for this research work

1.2.2: Applications of CNTs

There are two ways in which CNTs are usually synthesized depending upon the applications: Vertically aligned CNTs (VACNTs) or randomly oriented CNTs.

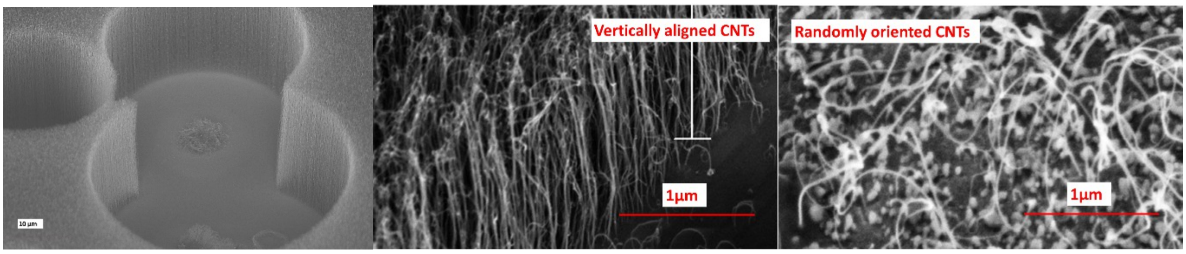

Figure 1. 5 (left) CNT Labyrinth, (mid) vertically aligned CNTs, (right) randomly oriented CNTs (synthesized in this thesis)

We will focus on vertically aligned CNTs, as CNT forest or (vertically aligned CNTs have gained a lot of attention in the past two decades and is undoubtedly the most studied material in the list of aligned structures. They are well oriented and are grown perpendicular to the substrate. Compared to randomly oriented CNTs, CNT forest has shown number of advantages like better coverage, better aspect ratio, improved electrical and mechanical properties, better sensing properties and more. Some of the reported work will be highlighted as following:

In the field of medicine, CNTs find diverse applications. they have been directly injected into experimental animals to increase heart rates. The inherit CNTs properties like thermal, mechanical, and electrical make them suitable for tissue growth and regeneration, specifically, as nervous tissue regenerator within the human body [67]. The following figure 1.6 comprehensively explains the diverse application of CNT forest in biomedicine. CNT forest has been used in biosensing, filtration, cell stimulation, bactericide, cell scaffolding and drug delivery [68].

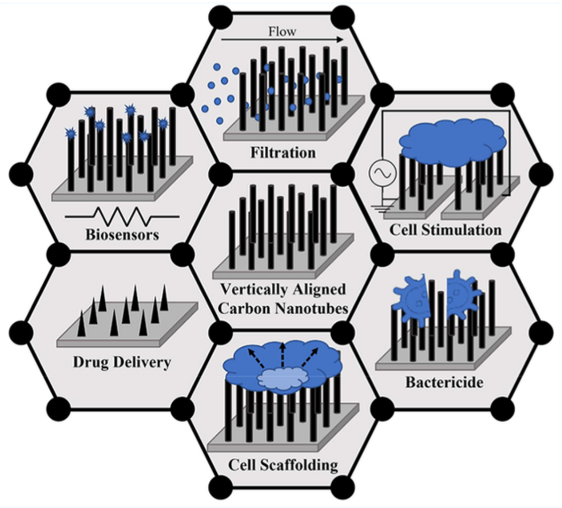

Figure 1. 6 Application of CNTF in the field of biomedical [68].

One of the most common utilities of CNT forest is as a field emitter material. It has been reported that the surface density of the forest plays an important role in field emission. High density causes the electromagnetic field to overlap, and the resultant field emission reduces [69]. Different substrate and catalysts have been used to get better results [70,71].

CNT forest in combination with other materials have shown enhanced Fisher- Tropsch synthesis activity as compared to the catalyst without carbon nanotube forest [72]. A well-defined channel can be created in carbon nanotube forest, in the direction of the ion diffusion which gives rise to better electronic conductivity and ion diffusivity. This will result in better transportation of ions and electrons through carbon nanotube forest to the active material and current collector, respectively [73]. Carbon nanotube forest is the darkest material synthesized. For solar cell application, carbon nanotube forest has shown increased efficiency towards absorption of light and radiation to electricity efficiency. Because of their well aligned long, porous structure, with slight surface randomness, light absorption has increased [74]. Nitrogen-doped CNTs forest have emerged as valuable metal-free electrode, exhibiting superior electrocatalytic activity and long-term stability. Nitrogen doping plays a pivotal role in enhancing the reactivity of CNTs' with metal oxide nanoparticles in lithium-ion batteries, considerably improving their storage capacity [75]. Additionally, due to CNT's high anti-corrosive properties they are replacing ITO coatings in the automobile sector [76].

CNTs and their composites, can be tailored to serve as highly efficient catalysts for sustainable energy applications. Unlike traditional inorganic catalysts, CNTs can form unique network structures, facilitating mass transfer. They exhibit inert characteristics, ensuring stability even in corrosive environment such as strong acids and alkalis. Moreover, CNTs can act as catalyst support to advance alternative catalyst material [77].

As CNTs primarily consist of surface structures, their entire mass is concentrated within their surface layers. This unique characteristic results in an exceptionally large unit surface area for tubulenes, adsorption capabilities, coupled with their sensitivity to atoms and molecules adhering to their surface, holds significant promise for the development of advanced sensors [78,79].

In short, CNTs are contributing across the spectrum of industries, due to their exceptional properties and adaptability to various applications [48].

Scientific community is now exploring the application by introducing the hybrid materials and nanocomposite of W/WO_x with CNs. The composites and hybrid materials have significantly increased the potential application specially in the field of mechanical strength, electric and thermal conductivity, and sensing devices.

1.3 Hybrid Materials

Hybrid material constitutes two entities at nano or molecular scales. Improved properties of hybrid material come not only from the individual components but also from the strong synergy created due to the large hybrid interface. The science of hybrid material has gained popularity over past couple of decades. The incorporation of different components into a single unit will not only present the individual characteristics of the components but also generate different physical and chemical properties than the parent constituents. The integration of these multiscale components can show improved thermal and chemical stability, mechanical strength, electrical and thermal properties [80]. At the nanoscale altering chemical and physical properties are viable, making particle size a very powerful tool for creating better materials, in terms of reactivity, conduction, strength etc. For the past three decades, technology evolution is more focused on organic-inorganic hybrid materials [81].

Naturally, existing hybrid materials were always around us, the best example is our bones [80], but it became more noticeable with the advancement of science. As shown in Figure 1.7, bone is composed of matrix and cellular components. The matrix formation requires interaction between organic and inorganic components [94].

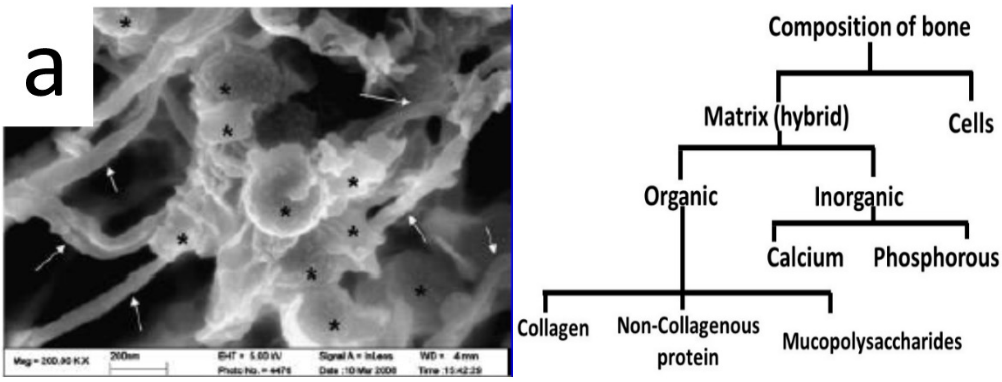

Figure 1. 7 a. SEM image showing collagen (arrows) and calcium (asterisk) [82] *and flow chart giving the composition of bone* [83].

The hybrid materials are in general classified into two categories, depending upon the interaction between the organic and inorganic materials. The nature of bonding between these two components will distinguish between Class I and Class II hybrid materials [80].

Class I: In this type of hybrid materials the interaction of bond between the two component is weak and is called non-covalent interaction. Therefore, the bonding between the components is either Van der Waals, hydrogen, or electrostatic interaction.

Class II: In this class the components share a strong bond like covalent bonding, between the components. Therefore, materials belonging to class II are more stable than Class I [80].

Apart from bonding, the interface of the hybrid material also determines its properties. The material thickness changed from macro to nanoscale will not only change its physical property (quantum size effect) but also the surface area interaction. In case of nanoscale coverage all the atoms are exposed to the other material.

The formation of hybrid material is again further subdivided into two types:

i. building block approach, ii. in-situ formation of the components.

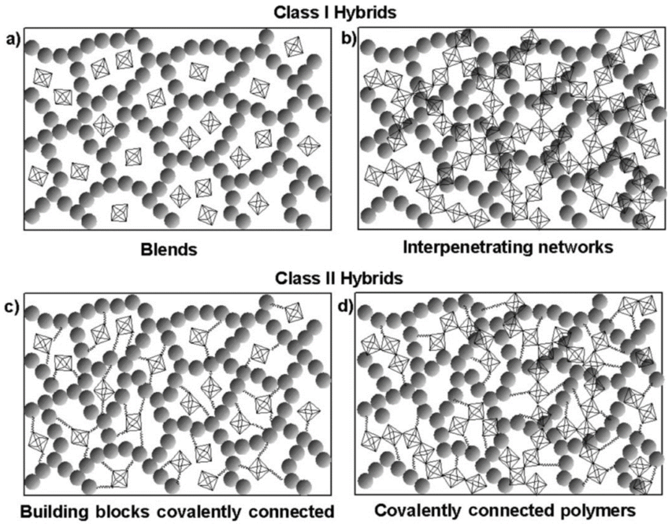

Figure 1. 8 Class I and Class II hybrid materials

i. **Building block approach**: This approach is sometimes also referred to as LEGO approach. In this approach both the components partially retain their identity, and the structural units of the components can be found even after the matrix is formed. The main advantage of this approach is that one of the structural units does not go a major structural change during formation of matrix [80].

ii. **In-situ formation of the components:** It is chemical transformation of the precursors that are used throughout the preparation process. In this approach the final product may have totally different properties than the parent constituents. This type of preparation process also depends upon the parameters used during synthesis process. Changing one parameter can vary the chemical or physical properties of the hybrid material [80].

The available combination of organic-inorganic components is limitless. This results in an exhaustless combination of these components. In modern technology, the application of hybrid material is almost in every field, from biomedical applications to the automotive industry, electronics, the energy sector, and mechanical and chemical engineering.

A brief view of reported research on hybrid material related to W/WO_x and C-based, and their contribution to the community is discussed.

In the fusion reactor plasma facing materials (PFM) are either W or C based materials. One of the problems that these PFM faces is the deuterium retention in the walls resulting in erosion.

Mostly, isotropic graphite and polycrystalline tungsten were used as material for plasma facing wall or in divertor of fusion reactor. When used individually in the fusion application isotropic graphite and polycrystalline tungsten faced the problems of erosion and deuterium retention. It was later suggested that when powders of tungsten and carbon were mixed using hot pressing at 2000 °C, and then exposed to deuterium irradiation in the electron cyclotron resonance (ECR) ion source, the mixture showed reduced deuterium retention that significantly reduced the erosion of the divertor plate of the fusion reactor [84].

Diaminoalkane-tungsten oxide hybrid material was synthesized. It was reported that the intercalation of the amine group into the tungsten oxide results in the increase in bandgap energy than the usual monoclinic WO_3 [85]. It is reported that the hybrid material of WO_3 nanofibers and carbon black holds extraordinary electrochemical activity when mixed with WO_3:C mass ratio equivalent to 10:1. Anodic current density noted for hybrid material was 11.2 mA/cm^2, higher than the commercially available Pt/C catalyst, figure 1.9 (a) [86]. G/MnO_2/WO_3 (where G is for graphene) hybrid material has been applied to the field of supercapacitors as well. It has been reported that hybrid material has shown high performance of supercapacitor as well as outstanding electroconductivity, due to rapid transfer of charge as compared to its counterpart's graphene (G) or G/MnO_2 samples, figure 1.9 (b) [87].

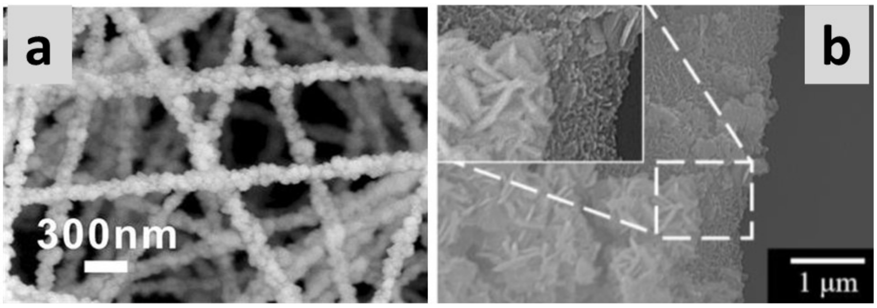

Figure 1. 9 SEM images of (a) WO_3 nanofibers obtained from the precursor fibres electro spun at AMT/PVP concentrations of 15/8 % [86] *(b) G/MnO_2/WO_3 hybrid material* [87]

CVD technique was used to synthesis high density CNTs forest, which was infiltrated by W using atomic layer deposition (ALD). W-carbon nanotube forest photonic crystals (figure 1.10) showed exceptional spectral and angular selectivity of photon absorbance and thermal emission. The composite showed minimal degradation of optical properties after being annealed at 1273 K for 168 hours, which superseded all the previous reported results [88].

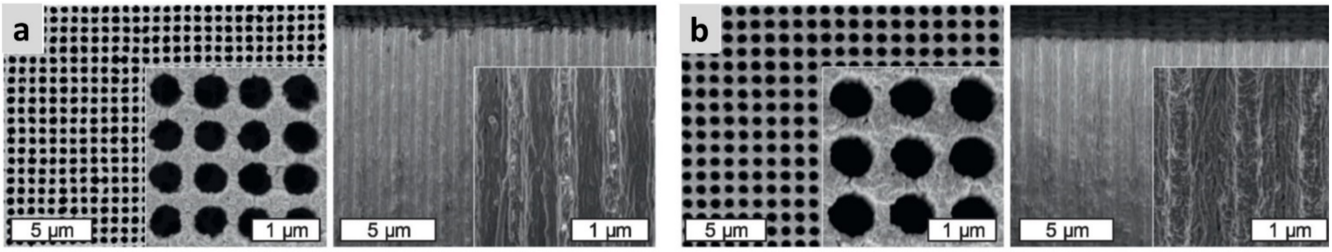

Figure 1. 10 SEM images from Top and side of the W-CNT absorber and emitter after ALD coating [88].

Hybrid material has proven their superiority in the field of gas sensors as well. WO_3/rGO (where rGO is for reduced graphene oxide) nanocomposite was reported as a gas sensing material to detect C_2H_2. The sample was prepared by hydrothermal process. The sample has showed low detection limit, i.e., 1.3 ppm at low operating temperature of 150 °C, with fast response and recovery time [89]. A gas sensitive material was prepared by metal-decorated (oxygen functionalized) MWCNTs dispersed on metal oxide nanoparticles. This material showed better response and recovery time than metal oxide film. It is discussed in the given case that the gas molecules adsorbed at the metal oxide site modifies the depletion layer at the surface of the grain and at the heterostructure formed (n-MO/p-MWCNTs), contributing to the better response of sensor (figure 1.11) [90].

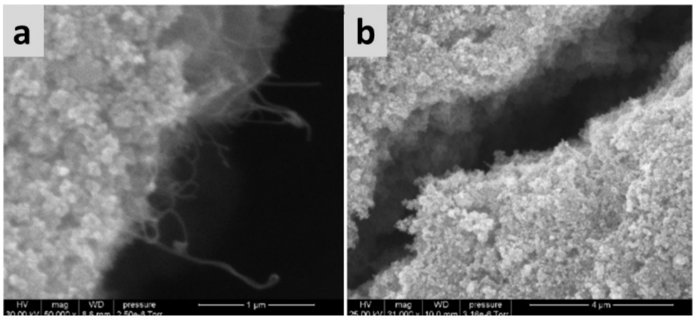

Figure 1. 11 SEM images of: (a) Ag-MWCNT/WO_3 (1/500 wt%); (b) Ag-MWCNT/SnO_2 (1/250 wt%) [90]

Acid precipitation method was used to synthesize WO_3 nanoplates, which were mixed with commercially available CNTs. The sample showed the best response to 300 ppm of NH_3 at RT as compared to acetone and ethanol. The overall response of the composite enhanced as compared to the pristine CNTs and was stable as compared to pristine WO_3, shown in figure 1.12 [91].

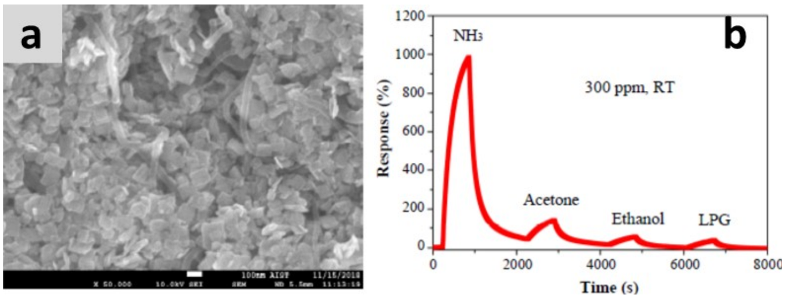

Figure 1. 12 (a) FESEM image showing surface of 0.5% CNT/WO$_3$ NC-based sensor, (b) Response of the 0.5% CNT/WO$_3$ NC-based sensor to different gases at RT and for 300 ppm concentration of gases [91]

Figure 1.13 shows CNT-WO$_3$ composite that was used to detect NO$_2$. When compared to CNTs sample that showed negligible response ($R_a/R_g = 1.05$) to NO$_2$, the composite showed better response ($R_a/R_g = 3.8$) to 5 ppm of NO$_2$ at 200 ºC [92].

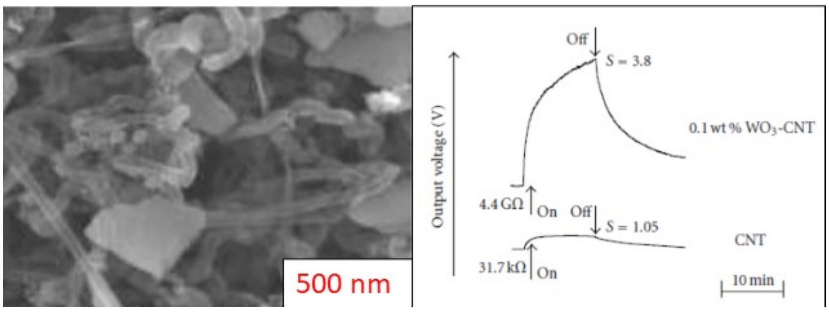

Figure 1. 13 (right) SEM image of 0.1 % WO$_3$-CNT sensor showing chunks or WO$_3$ on CNTs. (left) Response of CNT and CNT-WO$_3$ microsensors to 5 ppm NO$_2$ at 200°C [92]

CNTs and W/WO$_x$ individually have proven their worth in many applications. With every passing hour the demand for better, efficient, and green technology is rising. Hybrid material of W/WO$_x$ with carbon nanotube forest as template has the potential to facilitate many applications with better results than their parent materials. Synthesis techniques and applications discussed in this dissertation is just a step towards better future.

1.4 Reference

[1] Y. Yu, J. Song, F. Bai, A. Zheng, F. Peng, Ultra-high purity tungsten and its applications, Int J Refract Metals Hard Mater 53 (2015) 98–103. ttps://doi.org/10.1016/j.ijrmhm.2015.05.014.

[2] L.D. Beju, P. Dan Brindasu, S. Vulc, Grinding tungsten carbide used for manufacturing gun drills, Strojniski Vestnik/Journal of Mechanical Engineering 61 (2015) 571–582. https://doi.org/10.5545/sv-jme.2015.2594.

[3] Y.W. Chen, M.Y. Shie, C.H. Hsiao, Y.C. Liang, B. Wang, I.W.P. Chen, Synthesis of high-quality monolayer tungsten disulfide with chlorophylls and its application for enhancing bone regeneration, NPJ 2D Mater Appl 4 (2020). https://doi.org/10.1038/s41699-020-00168-y.

[4] Y. Şahin, Recent Progress in Processing of Tungsten Heavy Alloys, Journal of Powder Technology 2014 (2014) 1–22. https://doi.org/10.1155/2014/764306.

[5] M. Mews, L. Korte, B. Rech, Oxygen vacancies in tungsten oxide and their influence on tungsten oxide/silicon heterojunction solar cells, Solar Energy Materials and Solar Cells 158 (2016) 77–83. https://doi.org/10.1016/j.solmat.2016.05.042.

[6] C.M. Wu, S. Naseem, M.H. Chou, J.H. Wang, Y.Q. Jian, Recent advances in tungsten-oxide-based materials and their applications, Front Mater 6 (2019). https://doi.org/10.3389/fmats.2019.00049.

[7] H. Zheng, J.Z. Ou, M.S. Strano, R.B. Kaner, A. Mitchell, K. Kalantar-Zadeh, Nanostructured tungsten oxide - Properties, synthesis, and applications, Adv Funct Mater 21 (2011) 2175–2196. https://doi.org/10.1002/adfm.201002477.

[8] S. Vaddiraju, H. Chandrasekaran, M.K. Sunkara, Vapor phase synthesis of tungsten nanowires, J Am Chem Soc 125 (2003) 10792–10793. https://doi.org/10.1021/ja035868e.

[9] Jyothi Gutpa et al., PVD techniques proffering avenues for fabrication of porous tungsten oxide (WO3) thin films: A review, Material Science in Semiconductor Processing 143 (2022) 106534. https://doi.org/10.1016/j.mssp.2022.106534.

[10] D. Dellasega, S.M. Pietralunga, A. Pezzoli, V. Russo, L. Nasi, C. Conti, M.J. Vahid, A. Tagliaferri, M. Passoni, Tungsten oxide nanowires grown on amorphous-like tungsten films, Nanotechnology 26 (2015) 365601. https://doi.org/10.1088/0957-4484/26/36/365601.

[11] I. Kostis, N. Vourdas, M. Vasilopoulou, A. Douvas, G. Papadimitropoulos, N. Konofaos, A. Iliadis, D. Davazoglou, Formation of stoichiometric, sub-stoichiometric undoped and hydrogen doped tungsten oxide films, enabled by pulsed introduction of

O2 or H 2 during hot-wire vapor deposition, Thin Solid Films 537 (2013) 124–130. https://doi.org/10.1016/j.tsf.2013.04.021.

[12] F.C. Cheong, B. Varghese, Y. Zhu, E.P.S. Tan, L. Dai, V.B.C. Tan, C.T. Lim, C.H. Sow, WO3-x nanorods synthesized on a thermal hot plate, Journal of Physical Chemistry C 111 (2007) 17193–17199. https://doi.org/10.1021/jp074569z.

[13] H. Kominami, K.I. Yabutani, T. Yamamoto, Y. Kera, B. Ohtani, Synthesis of highly active tungsten(VI) oxide photocatalysts tfor oxygen evolution by hydrothermal treatment of aqueous tungstic acid solutions, J Mater Chem 11 (2001) 3222–3227. https://doi.org/10.1039/b104223h.

[14] T. Van Nguyen, H.H. Do, W. Guo, M. Tekalne, Q. Van Le, T.P. Nguyen, J.H. Cho, S.H. Ahn, S.Y. Kim, Tungsten Oxide-Modified ITO Electrode for Electrochromic Window Based on Reversible Metal Electrodeposition, Electronic Materials Letters 18 (2022) 36–46. https://doi.org/10.1007/s13391-021-00320-w.

[15] C. Guo, S. Yin, M. Yan, M. Kobayashi, M. Kakihana, T. Sato, Morphology-controlled synthesis of W 18O 49 nanostructures and their near-infrared absorption properties, Inorg Chem 51 (2012) 4763–4771. https://doi.org/10.1021/ic300049j.

[16] A. Chithambararaj, P. Nandigana, M. Kaleesh Kumar, A.S. Prakash, S.K. Panda, Enhanced electrochromism from non-stoichiometric electrodeposited tungsten oxide thin films, Appl Surf Sci 582 (2022). https://doi.org/10.1016/j.apsusc.2022.152424.

[17] C. Ng, C. Ye, Y.H. Ng, R. Amal, Flower-shaped tungsten oxide with inorganic fullerene-like structure: Synthesis and characterization, Cryst Growth Des 10 (2010) 3794–3801. https://doi.org/10.1021/cg100625m.

[18] Z. Tóth, H. Lovas, Chemistry of materials science phenomena in high-intensity discharge light sources, in: Pure and Applied Chemistry, 2007: pp. 1771–1778. https://doi.org/10.1351/pac200779101771.

[19] G. Di Benedetto, P. Matteis, G. Scavino, Impact behavior and ballistic efficiency of armor-piercing projectiles with tool steel cores, Int J Impact Eng 115 (2018) 10–18. https://doi.org/10.1016/j.ijimpeng.2017.12.021.

[20] A. Arora, V.G. Gopal Rao, Tungsten heavy alloy for defence applications, Materials Technology 19 (2004) 210–216. https://doi.org/10.1080/10667857.2004.11753087.

[21] N. Jamal AbuAlRoos, M.N. Azman, N.A. Baharul Amin, R. Zainon, Tungsten-based material as promising new lead-free gamma radiation shielding material in nuclear medicine, Physica Medica 78 (2020) 48–57. https://doi.org/10.1016/j.ejmp.2020.08.017.

[22] H. Yin, J. Wang, W. Guo, L. Cheng, Y. Yuan, G. Lu, Recent studies of tungsten-based plasma-facing materials in the linear plasma device STEP, Tungsten 1 (2019) 132–140. https://doi.org/10.1007/s42864-019-00004-x.

[23] M. Battabyal, R. Schäublin, P. Spätig, M. Walter, M. Rieth, N. Baluc, Microstructure and mechanical properties of a W-2wt.%Y2O 3 composite produced by sintering and hot forging, Journal of Nuclear Materials 442 (2013). https://doi.org/10.1016/j.jnucmat.2013.01.301.

[24] H. Bolt, V. Barabash, W. Krauss, J. Linke, R. Neu, S. Suzuki, N. Yoshida, Materials for the plasma-facing components of fusion reactors, in: Journal of Nuclear Materials, 2004: pp. 66–73. https://doi.org/10.1016/j.jnucmat.2004.04.005.

[25] R. Mateus, M. Dias, J. Lopes, J. Rocha, N. Catarino, P. Duarte, R.B. Gomes, C. Silva, H. Fernandes, V. Livramento, P.A. Carvalho, E. Alves, K. Hanada, J.B. Correia, Blistering of W-Ta composites at different irradiation energies, Journal of Nuclear Materials 438 (2013). https://doi.org/10.1016/j.jnucmat.2013.01.225.

[26] C.L. Chen, Y. Zeng, Synthesis and characteristics of W-Ti alloy dispersed with Y2Ti2O7 oxides, Int J Refract Metals Hard Mater 56 (2016) 104–109. https://doi.org/10.1016/j.ijrmhm.2015.12.008.

[27] X.Y. Ding, L.M. Luo, H.Y. Chen, G.N. Luo, X.Y. Zhu, X. Zan, J.G. Cheng, Y.C. Wu, Fabrication of W-1 wt.% TiC composites by spark plasma sintering, Fusion Engineering and Design 92 (2015) 29–34. https://doi.org/10.1016/j.fusengdes.2015.01.003.

[28] X.Y. Ding, L.M. Luo, Z.L. Lu, G.N. Luo, X.Y. Zhu, J.G. Cheng, Y.C. Wu, chemically produced tungsten-praseodymium oxide composite sintered by spark plasma sintering, Journal of Nuclear Materials 454 (2014) 200–206. https://doi.org/10.1016/j.jnucmat.2014.07.048.

[29] J. Du, T. Höschen, M. Rasinski, J.H. You, Shear debonding behavior of a carbon-coated interface in a tungsten fiber-reinforced tungsten matrix composite, in: Journal of Nuclear Materials, 2011: pp. 472–476. https://doi.org/10.1016/j.jnucmat.2010.12.254.

[30] G. He, K. Xu, S. Guo, X. Qian, Z. Yang, G. Liu, J. Li, Preparation of tungsten fiber reinforced-tungsten/copper composite for plasma facing component, Journal of Nuclear Materials 455 (2014) 225–228. https://doi.org/10.1016/j.jnucmat.2014.05.026.

[31] K. Arshad, J. Wang, Y. Yuan, Y. Zhang, Z.J. Zhou, G.H. Lu, Development of tungsten-based materials by different sintering techniques, Int J Refract Metals Hard Mater 50 (2015) 253–257. https://doi.org/10.1016/j.ijrmhm.2015.02.004.

[32] D. Fasquelle, N. Verbrugghe, S. Deputier, D. Fasquelle, N. Verbrugghe, S. Députier, Tungsten-Based Cost-Effective Gas Sensors for H 2 S Detection, Chemosensors 9 (2021). https://doi.org/10.3390/chemosensors9110295.

[33] W. Thongpan, D. Louloudakis, P. Pooseekheaw, T. Kumpika, E. Kantarak, A. Panthawan, A. Tuantranont, W. Thongsuwan, P. Singjai, Electrochromic properties of

tungsten oxide films prepared by sparking method using external electric field, Thin Solid Films 682 (2019) 135–141. https://doi.org/10.1016/j.tsf.2019.04.010.

[34] X. Liu, F. Wang, Q. Wang, Nanostructure-based WO 3 photoanodes for photoelectrochemical water splitting, Physical Chemistry Chemical Physics 14 (2012) 7894–7911. https://doi.org/10.1039/c2cp40976c.

[35] C.C. Mardare, A.W. Hassel, Review on the Versatility of Tungsten Oxide Coatings, Physica Status Solidi (A) Applications and Materials Science 216 (2019). https://doi.org/10.1002/pssa.201900047.

[36] S. Cao, C. Zhao, T. Han, L. Peng, Hydrothermal synthesis, characterization and gas sensing properties of the WO3 nanofibers, Mater Lett 169 (2016) 17–20. https://doi.org/10.1016/j.matlet.2016.01.053.

[37] M. Wilken, E. Ciftyürek, S. Cwik, L. Mai, B. Mallick, D. Rogalla, K. Schierbaum, A. Devi, CVD Grown Tungsten Oxide for Low Temperature Hydrogen Sensing: Tuning Surface Characteristics via Materials Processing for Sensing Applications, Small 19 (2023). https://doi.org/10.1002/smll.202204636.

[38] J. Tamaki, Z. Zhang, K. Fujimori, M. Akiyama, T. Harada, N. Miura, N. Yamazoe, Grain-Size Effects in Tungsten Oxide-Based Sensor for Nitrogen Oxides, J Electrochem Soc 141 (1994) 2207–2210. https://doi.org/10.1149/1.2055088.

[39] Y. Yao, M. Yin, J. Yan, S. (Frank) Liu, P-type sub-tungsten-oxide based urchin-like nanostructure for superior room temperature alcohol sensor, Appl Surf Sci 441 (2018) 277–284. https://doi.org/10.1016/j.apsusc.2018.02.004.

[40] H. Yu, Z. Song, Q. Liu, X. Ji, J. Liu, S. Xu, H. Kan, B. Zhang, J. Liu, J. Jiang, L. Miao, H. Liu, Colloidal synthesis of tungsten oxide quantum dots for sensitive and selective H2S gas detection, Sens Actuators B Chem 248 (2017) 1029–1036. https://doi.org/10.1016/j.snb.2017.03.044.

[41] R. Godbole, S. Ameen, U.T. Nakate, M. Shaheer Akhtar, H.S. Shin, Low temperature HFCVD synthesis of tungsten oxide thin film for high response hydrogen gas sensor application, Mater Lett 254 (2019) 398–401. https://doi.org/10.1016/j.matlet.2019.07.110.

[42] M. Breedon, P. Spizzirri, M. Taylor, J. Du Plessis, D. McCulloch, J. Zhu, L. Yu, Z. Hu, C. Rix, W. Wlodarski, K. Kalantar-zadeh, Synthesis of nanostructured tungsten oxide thin films: A simple, controllable, inexpensive, aqueous sol-gel method, Cryst Growth Des 10 (2010) 430–439. https://doi.org/10.1021/cg9010295.

[43] V.D.N. Bezzon, T.L.A. Montanheiro, B.R.C. De Menezes, R.G. Ribas, V.A.N. Righetti, K.F. Rodrigues, G.P. Thim, Carbon Nanostructure-based Sensors: A Brief Review on Recent Advances, Advances in Materials Science and Engineering 2019 (2019). https://doi.org/10.1155/2019/4293073.

[44] V. Georgakilas, J.A. Perman, J. Tucek, R. Zboril, Broad Family of Carbon Nanoallotropes: Classification, Chemistry, and Applications of Fullerenes, Carbon Dots, Nanotubes, Graphene, Nanodiamonds, and Combined Superstructures, Chem Rev 115 (2015) 4744–4822. https://doi.org/10.1021/cr500304f.

[45] I. V. Zaporotskova, N.P. Boroznina, Y.N. Parkhomenko, L. V. Kozhitov, Carbon nanotubes: Sensor properties. A review, Modern Electronic Materials 2 (2016) 95–105. https://doi.org/10.1016/j.moem.2017.02.002.

[46] T. Maruyama, Carbon nanotubes, in: Handbook of Carbon-Based Nanomaterials, Elsevier, 2021: pp. 299–319. https://doi.org/10.1016/B978-0-12-821996-6.00009-9.

[47] A. Aqel, K.M.M.A. El-Nour, R.A.A. Ammar, A. Al-Warthan, Carbon nanotubes, science and technology part (I) structure, synthesis and characterisation, Arabian Journal of Chemistry 5 (2012) 1–23. https://doi.org/10.1016/j.arabjc.2010.08.022.

[48] S. Rathinavel, K. Priyadharshini, D. Panda, A review on carbon nanotube: An overview of synthesis, properties, functionalization, characterization, and the application, Mater Sci Eng B Solid State Mater Adv Technol 268 (2021). https://doi.org/10.1016/j.mseb.2021.115095.

[49] S. Iijima, Helical microtubules of graphitic carbon, Nature 354 (1991) 56–58.

[50] H. Ur Rashid, K. Yu, M. Naveed Umar, M. Naveed Anjum, K. Khan, N. Ahmad, M. Tariq Jan, CATALYST ROLE IN CHEMICAL VAPOR DEPOSITION (CVD) PROCESS: A REVIEW, Rev. Adv. Mater. Sci 40 (2015) 235–248.

[51] G.N. Ayre, T. Uchino, B. Mazumder, A.L. Hector, J.L. Hutchison, D.C. Smith, P. Ashburn, C.H. De Groot, On the mechanism of carbon nanotube formation: The role of the catalyst, Journal of Physics Condensed Matter 23 (2011). https://doi.org/10.1088/0953-8984/23/39/394201.

[52] A. Malesevic, H. Chen, T. Hauffman, A. Vanhulsel, H. Terryn, C. Van Haesendonck, Study of the catalyst evolution during annealing preceding the growth of carbon nanotubes by microwave plasma-enhanced chemical vapour deposition, Nanotechnology 18 (2007). https://doi.org/10.1088/0957-4484/18/45/455602.

[53] K.E. Kim, K.J. Kim, W.S. Jung, S.Y. Bae, J. Park, J. Choi, J. Choo, Investigation on the temperature-dependent growth rate of carbon nanotubes using chemical vapor deposition of ferrocene and acetylene, Chem Phys Lett 401 (2005) 459–464. https://doi.org/10.1016/j.cplett.2004.11.113.

[54] S. Takenaka, T. Iguchi, E. Tanabe, H. Matsune, M. Kishida, Formation of carbon nanotubes through ethylene decomposition over supported Pt catalysts and silica-coated Pt catalysts, Carbon N Y 47 (2009) 1251–1257. https://doi.org/10.1016/j.carbon.2008.12.051.

[55] V. Sivakumar, A.R. Mohamed, A.Z. Abdullah, S.P. Chai, Role of reaction and factors of carbon nanotubes growth in chemical vapour decomposition process using Methane-A highlight, J Nanomater 2010 (2010). https://doi.org/10.1155/2010/395191.

[56] U.C. Chung, W.S. Chung, Mechanism on Growth of Carbon Nanotubes Using CO-H_2 Gas Mixture, Materials Science Forum 475–479 (2005) 3551–3554. https://doi.org/10.4028/www.scientific.net/msf.475-479.3551.

[57] M. José-Yacamán, M. Miki-Yoshida, L. Rendón, J.G. Santiesteban, Catalytic growth of carbon microtubules with fullerene structure, Appl Phys Lett 62 (1993) 657–659. https://doi.org/10.1063/1.108857.

[58] Z.-J. Liu, R. Che, Z. Xu, L.-M. Peng, Preparation of Fe-filled carbon nanotubes by catalytic decomposition of cyclohexane, Synth Met 128 (2002) 191–195. https://doi.org/10.1016/S0379-6779(02)00005-X.

[59] R.E. Morjan, O.A. Nerushev, M. Sveningson, F. Rohmund, L.K.L. Falk, E.E.B. Campbell, Growth of carbon nanotubes from C60, Appl Phys A Mater Sci Process 78 (2004) 253–261. https://doi.org/10.1007/s00339-003-2297-z.

[60] H. Dai, A.G. Rinzler, P. Nikolaev, A. Thess, D.T. Colbert, R.E. Smalley, Single-wall nanotubes produced by metal-catalyzed disproportionation of carbon monoxide, Chem Phys Lett 260 (1996) 471–475. https://doi.org/10.1016/0009-2614(96)00862-7.

[61] S. Maruyama, R. Kojima, Y. Miyauchi, S. Chiashi, M. Kohno, Low-temperature synthesis of high-purity single-walled carbon nanotubes from alcohol, Cheical Physics Letters 360 (2002) 229–234. https://doi.org/10.1016/S0009-2614(02)00838-2.

[62] Y. Murakami, Y. Miyauchi, S. Chiashi, S. Maruyama, Direct synthesis of high-quality single-walled carbon nanotubes on silicon and quartz substrates, Chem Phys Lett 377 (2003) 49–54. https://doi.org/10.1016/S0009-2614(03)01094-7.

[63] M. Kumar, Y. Ando, Chemical vapor deposition of carbon nanotubes: A review on growth mechanism and mass production, J Nanosci Nanotechnol 10 (2010) 3739–3758. https://doi.org/10.1166/jnn.2010.2939.

[64] M. He, A.I. Chernov, E.D. Obraztsova, J. Sainio, E. Rikkinen, H. Jiang, Z. Zhu, A. Kaskela, A.G. Nasibulin, E.I. Kauppinen, M. Niemelä, O. Krause, Low Temperature Growth of SWNTs on a Nickel Catalyst by Thermal Chemical Vapor Deposition, Nano Res 4 (2011) 334–342. https://doi.org/10.1007/s12274-010-0088-3.

[65] J.C. Acomb, C. Wu, P.T. Williams, Effect of growth temperature and feedstock:catalyst ratio on the production of carbon nanotubes and hydrogen from the pyrolysis of waste plastics, J Anal Appl Pyrolysis 113 (2015) 231–238. https://doi.org/10.1016/j.jaap.2015.01.012.

[66] G. Messina, S. Santangelo, M.G. Donato, M. Lanza, C. Milone, A. Pistone, S. Galvagno, Multi-walled carbon nanotubes production by ethane decomposition over

silica-supported iron-catalysts, Physica Status Solidi (A) Applications and Materials Science 205 (2008) 2422–2427. https://doi.org/10.1002/pssa.200723647.

[67] N. Jain, S. Tiwari, Biomedical application of carbon nanotubes (CNTs) in vulnerable parts of the body and its toxicity study: A state-of-the-art-review, in: Mater Today Proc, Elsevier Ltd, 2021: pp. 7608–7617. https://doi.org/10.1016/j.matpr.2021.01.895.

[68] A. Kohls, M. Maurer Ditty, F. Dehghandehnavi, S.Y. Zheng, Vertically Aligned Carbon Nanotubes as a Unique Material for Biomedical Applications, ACS Appl Mater Interfaces 14 (2022) 6287–6306. https://doi.org/10.1021/acsami.1c20423.

[69] E.G. Rakov, Materials made of carbon nanotubes. The carbon nanotube forest, Russian Chemical Reviews 82 (2013) 538–566. https://doi.org/10.1070/rc2013v082n06abeh004340.

[70] A. Thapa, J. Guo, K.L. Jungjohann, X. Wang, W. Li, Density control of vertically aligned carbon nanotubes and its effect on field emission properties, Mater Today Commun 22 (2020). https://doi.org/10.1016/j.mtcomm.2019.100761.

[71] B.K. Gupta, G. Kedawat, A.K. Gangwar, K. Nagpal, P.K. Kashyap, S. Srivastava, S. Singh, P. Kumar, S.R. Suryawanshi, D.M. Seo, P. Tripathi, M.A. More, O.N. Srivastava, M.G. Hahm, D.J. Late, High-performance field emission device utilizing vertically aligned carbon nanotubes-based pillar architectures, AIP Adv 8 (2018). https://doi.org/10.1063/1.5004769.

[72] Y.H. Chin, J. Hu, C. Cao, Y. Gao, Y. Wang, Preparation of a novel structured catalyst based on aligned carbon nanotube arrays for a microchannel Fischer-Tropsch synthesis reactor, Catal Today 110 (2005) 47–52. https://doi.org/10.1016/j.cattod.2005.09.007.

[73] X. Wang, T. Wang, J. Borovilas, X. He, S. Du, Y. Yang, Vertically-aligned nanostructures for electrochemical energy storage, Nano Res 12 (2019) 2002–2017. https://doi.org/10.1007/s12274-019-2392-x.

[74] B.I. Kharisov, O. V. Kharissova, B.O. García, Y.P. Méndez, I.G. De La Fuente, State of the art of nanoforest structures and their applications, RSC Adv 5 (2015) 105507–105523. https://doi.org/10.1039/c5ra22738k.

[75] H.S. Balasubramanya, P. Gupta, A Review on Applications of Carbon Nanotubes in Automobiles, International Journal of Mechanical Engineering and Technology 11 (2020) 204–210.

[76] M.F.L. De Volder, S.H. Tawfick, R.H. Baughman, A.J. Hart, Carbon Nanotubes: Present and Future Commercial Applications, Science (1979) 339 (2013) 535–539. https://doi.org/10.1126/science.1222453.

[77] X. Jia, F. Wei, Advances in Production and Applications of Carbon Nanotubes, Top Curr Chem 375 (2017). https://doi.org/10.1007/s41061-017-0102-2.

[78] W. De Zhang, W.H. Zhang, Carbon nanotubes as active components for gas sensors, J Sens 2009 (2009). https://doi.org/10.1155/2009/160698.

[79] K.F. Akhmadishina, I.I. Bobrinetskii, I.A. Komarov, A.M. Malovichko, V.K. Nevolin, V.A. Petukhov, A. V. Golovin, A.O. Zalevskii, Flexible biological sensors based on carbon nanotube films, Nanotechnol Russ 8 (2013) 721–726. https://doi.org/10.1134/S1995078013060025.

[80] Guido. Kickelbick, Hybrid materials : synthesis, characterization, and applications, Wiley - VCH, 2007. https://doi.org/10.1002/9783527610495.

[81] Y. Chujo, Organic-inorganic hybrid materials, Current Opinion in SOlid State and Material Science 1 (1996) 806–811. https://doi.org/10.1016/S1359-0286(96)80105-7.

[82] B.P. Chan, G.C. F Chan, B. Pui Chan, T. Yan Hui, M. Yi Wong, K. Hak Kong Yip, G. Chi Fung Chan, Mesenchymal stem cell-encapsulated collagen microspheres for bone tissue engineering, Yissue Enginnering Part C: Methods 16 (2009). https://doi.org/10.1089/ten.tec.2008.0709.

[83] C. Licini, C. Vitale-Brovarone, M. Mattioli-Belmonte, Collagen and non-collagenous proteins molecular crosstalk in the pathophysiology of osteoporosis, Cytokine Growth Factor Rev 49 (2019) 59–69. https://doi.org/10.1016/j.cytogfr.2019.09.001.

[84] T. Hino, F. Hirano, Y. Yamauchi, Y. Hirohata, Hydrogen retention and erosion of carbon-tungsten mixed material, Fusion Engineering and Design (2000) 49–50. https://doi.org/10.1016/S0920-3796(00)00347-1.

[85] S. V. Chong, B. Ingham, J.L. Tallon, Novel materials based on organic-tungsten oxide hybrid systems I: Synthesis and characterisation, Current Applied Physics 4 (2004) 197–201. https://doi.org/10.1016/j.cap.2003.11.008.

[86] X. Zhou, Y. Qiu, J. Yu, J. Yin, X. Bai, High electrochemical activity from hybrid materials of electrospun tungsten oxide nanofibers and carbon black, J Mater Sci 47 (2012) 6607–6613. https://doi.org/10.1007/s10853-012-6596-7.

[87] S.Y. Huang, P.A. Le, P.J. Yen, Y.C. Lu, S.K. Sahoo, H.W. Cheng, P.W. Chiu, T.Y. Tseng, K.H. Wei, Cathodic plasma–induced syntheses of graphene nanosheet/MnO2/WO3 architectures and their use in supercapacitors, Electrochim Acta 342 (2020). https://doi.org/10.1016/j.electacta.2020.136043.

[88] K. Cui, P. Lemaire, H. Zhao, T. Savas, G. Parsons, A.J. Hart, Tungsten–Carbon Nanotube Composite Photonic Crystals as Thermally Stable Spectral-Selective Absorbers and Emitters for Thermophotovoltaics, Adv Energy Mater 8 (2018). https://doi.org/10.1002/aenm.201801471.

[89] Z. Jiang, W. Chen, L. Jin, F. Cui, Z. Song, C. Zhu, High performance acetylene sensor with heterostructure based on WO3 nanolamellae/reduced graphene oxide (rGO)

nanosheets operating at low temperature, Nanomaterials 8 (2018). https://doi.org/10.3390/nano8110909.

[90] R. Ionescu, E.H. Espinosa, R. Leghrib, A. Felten, J.J. Pireaux, R. Erni, G. Van Tendeloo, C. Bittencourt, N. Cañellas, E. Llobet, Novel hybrid materials for gas sensing applications made of metal-decorated MWCNTs dispersed on nano-particle metal oxides, Sens Actuators B Chem 131 (2008) 174–182. https://doi.org/10.1016/j.snb.2007.11.001.

[91] X.V. Le, V.T. Duong, L.A.L. Thi, V.T. Pham, H.L. Nguyen, C.T. Nguyen, Composition of CNT and WO3 nanoplate: Synthesis and NH3 gas sensing characteristics at low temperature, Journal of Metals, Materials and Minerals 29 (2019) 61–68. https://doi.org/10.14456/jmmm.2019.48.

[92] T. Hashishin, J. Tamaki, Conductivity-type sensor based on CNT- WO 3 composite for NO 2 detection, J Nanomater 2008 (2008). https://doi.org/10.1155/2008/352854.

Chapter 2

Synthesis and Experimental Methods

The purpose of this chapter is to provide an overview of the experimental techniques used in our research work. In each section, the basic concepts and the importance regarding the specific technique is discussed. The growth techniques employed are discussed followed by an introduction to the tools used for characterization of the sample that include photoemission spectroscopy (XPS), scanning electron microscopy (SEM), atomic force microscopy (AFM), Raman spectroscopy, and x-ray diffraction (XRD). In the last part of the chapter, we will go through the details of the experiments performed to prepare the samples reported in this dissertation.

2.1 Growth techniques:

A thin film is defined as a low dimensional material deposited on a substrate by condensing sequentially atomic/molecular or species of matter. Thin film thickness varies from few nanometres to tens of microns. The advancement in thin film technology is attributed to the development of vacuum technology, advances in surface sensitive probes, and electron diffraction methods. In modern era of science and technology, many different techniques have been developed for the growth of reproducible thin films. These films are then evaluated and employed in the field of electronics, optics, sensors, and medicine to name a few [1].

Two main categories in the growth of thin films are physical vapour deposition (PVD) and chemical vapour deposition (CVD). PVD is a technique in which a material is vaporized in vacuum and deposited on the substrate; list of techniques that work on this principle are high vacuum evaporator, **electron beam**, **sputtering**, ion implantation, arc discharge and induction evaporator. Whereas in CVD volatile precursors (one or more) react and/or decompose in the presence of substrate to produce the film. CVD can be subdivided into following techniques: low pressure CVD, plasma enhanced CVD, catalytic CVD, metal organic CVD, and hot filament CVD [2].

2.1.1 Electron beam evaporator (e-beam)

E-beam deposition is one of the tools that falls under the category of PVD. With time e-beam deposition has become one of the most used methods to synthesize thin films for scientific research. The main advantage posed by e-beam is that it facilitates the deposition of a wide range of metals and oxides specially, the ones with low vapour pressure, and strongly bonded atoms.

The basic principle of an e-beam is that highly accelerated electrons are used to evaporate the source material under high vacuum conditions for the deposition of thin films [1].

The electron beam is generated by a filament, usually a tungsten filament. The emission of electrons from the filament is obtained by thermionic emission. Once the electrons are emitted, they are accelerated and focused on the target by the application of voltage (up to tens of kilo Volts) between the cathode (filament) and the target. These energetic electrons, when striking the target, transfer their kinetic energy into heat energy, increasing the target temperature till it reaches the correct vapour pressure to obtain the desired deposition rate. This process requires vacuum environment, usually the base pressure is in the range of 10^{-5} - 10^{-6} mbar, allowing the electrons and the target's vapour to have enough inelastic mean free path to reach, respectively, the target and the substrate. The target's vapour then can travel in the vacuum chamber and is deposited on the substrate and the required coating is accomplished [1]. A typical commercial e-beam apparatus is shown in figure 2.1(left), and in the figure 2.1 (right) the position of e-beam source can be customized according to the requirements.

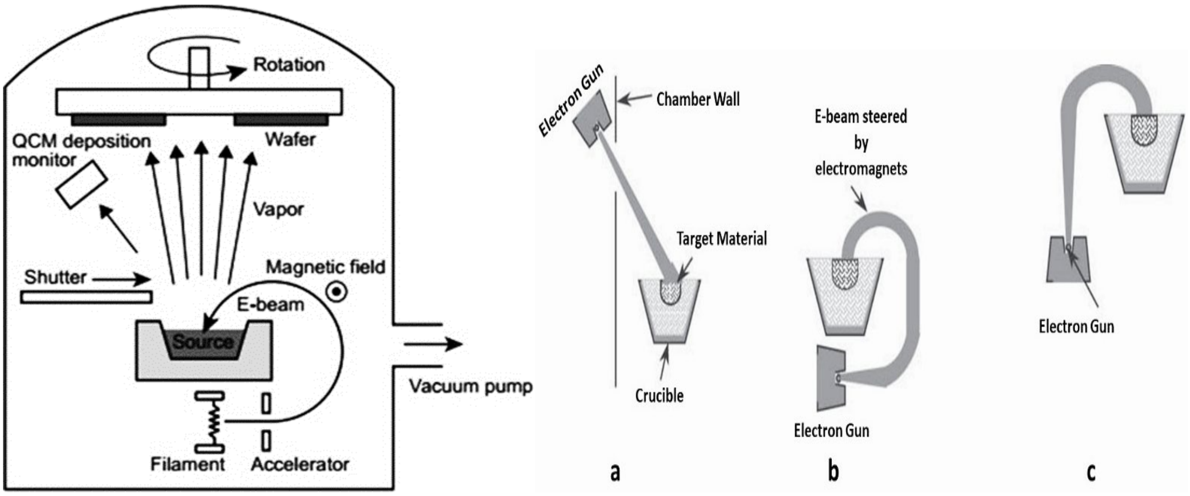

Figure 2. 1 (left) A commonly used commercially available e-beam chamber. E-beam is directed on to the source material, which sublimates (or evaporates) and gets deposited on to the substrate. QCM, monitors the thickness of the sample, whereas shutter can be used to block the vapours to reach the substrate. (right) possible positions of e-beam in a system [1,3]

Resistive heating deposition process is considered as a competitor to e-beam. In resistive heating the material to be deposited is heated directly by using a resistive heater or a filament. In comparison to resistive heating deposition process, the use of an e-beam has several advantages: [1,3]

- lower level of contamination from the crucible as the beam of electrons is focused, resulting in high-purity films.
- Higher deposition rate is achieved, by focusing on a smaller area of the target, thus facilitating the deposition of materials with high melting points or low vapour pressure.
- Better heat efficiency is accomplished, as conduction and radiation losses can be minimized.

There are some disadvantages in selecting e-beam deposition:

- Electron beam deposition is a line-of-sight deposition method, therefore complex geometrical shapes cannot be coated completely using this technique. For example, samples with undercut or gas turbines etc [4].
- It is an expensive tool because it requires high voltage to deposit high melting point materials and vacuum environment.

Like all other deposition techniques e-beam has multiple applications in the field of research:

- ✓ In the field of renewable energy, thin films for solar cells are deposited using e-beam [5]
- ✓ Nobel metals used for the preparation of organic light emitting diodes (OLED) are deposited [6]
- ✓ Reflective and anti-reflective coatings could be performed [7]
- ✓ Thin layers of catalysts are deposited for various applications [1]

2.1.2 Sputtering

Sputtering is widely employed in industrial applications such as cutting tools, semiconductors, and more. It is a preferred technique in industrial settings due to its relatively affordable maintenance costs. Like other growth techniques, sputtering finds applications across various research fields, ranging from biology, semiconductors, and renewable technologies [8–10]

The term “sputter” literally means to spit, but in scientific terms, it refers to the process where high energy ions bombard a target material under specific conditions, resulting in the ejection of atoms from the target. These ejected atoms are then directed towards the substrate, leading to the formation of the desired thin films. This process can be visualized as target spitting atoms onto the substrate.

In general, commercially available sputtering setup is equipped with a cathode (the source material/target) and an anode (the substrate/sample) within a high vacuum discharge unit. The setup also consists of a vacuum system, and a gas inlet assembly (to facilitate plasma generation by introducing an inert gas mostly argon or to create a reactive environment by exposing the chamber to gases like oxygen, nitrogen, or acetylene) [10]

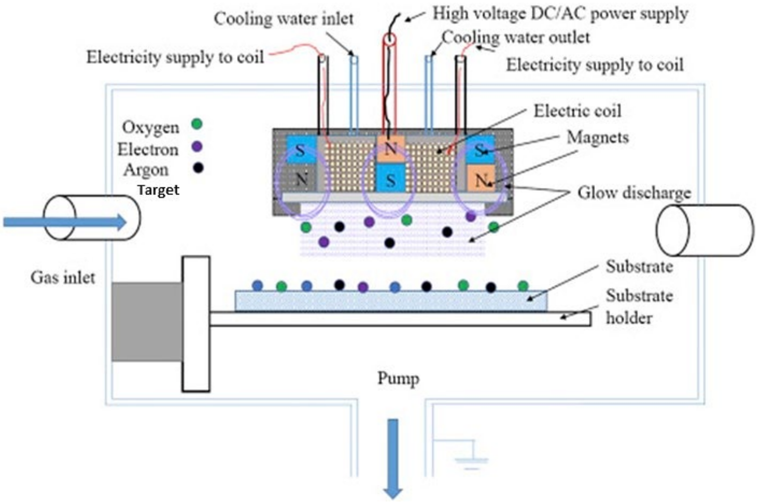

Figure 2. 2 Schematics of commercially available sputtering system. An electromagnetic field is applied between the electrodes which ionized the gas in the chamber. The ions are bombarded onto the target materials causing atoms/particles to eject from it. These ejected atoms/particles get deposited on the substrate [11]

Figure 2.2 depicts the schematics of a sputtering process, which is a plasma based PVD method. To generate plasma, an electromagnetic field is applied between the anode and the cathode while fluxing the desired gas. The gas in the chamber is ionized at low pressure (10^{-5} - 10^{-4} mbar), leading to plasma generation. As illustrated in the figure 2.2, the ions generated by plasma bombard the target, resulting in the ejection of atoms/particles from the target material. These particles are subsequently deposited onto the substrate [12].

Deposition of the film is influenced by various deposition parameters, such as working pressure, distance between the target and substrate, substrate temperature, substrate biasing, and input target power density.

Localized plasma is created at the surface of the substrate when substrate biasing is applied in the presence of partial pressure of the gas. Prior to deposition, this plasma proves beneficial for pre-cleaning, oxidation, or gentle etching of the surface of the sample. During the deposition process, it aids in improved adhesion, material reactivity and surface density. Substrate biasing has a robust effect on the mechanical properties of the film as high energy bombarding ions impart higher compression to the film [10].

Applying temperature to the substrate enhances the mobility of the impinging atoms on the surface of the substrate. The temperature increases the grain size of the material deposited [12].

There are three modes of sputtering that can be employed depending on the requirement and the type of material to be deposited. These modes are direct current magnetron sputtering (DCMS), radio frequency sputtering (RF) and high-power impulse magnetron sputtering (HiPIMS).

In DCMS, a magnetron (permanent magnet system) is used to establish a magnetic field parallel to the target surface. This magnetic field confines secondary electrons in the neighbourhood of the target surface. Leading to a tremendous increase in ion concentration near the target, resulting in high sputtering rate. Consequently, a high sputtering rate can be achieved without increasing the gas pressure, hence maintaining high vacuum conditions [13].

DCMS is conveniently used to deposit metallic films, while for insulating materials, the charging of the target due to interaction with positive ions, hinders the process of deposition [14].

RF sputtering employed to address the challenges associated with depositing insulating materials. An alternating current (AC) RF power supply is used. The motion of electron in the plasma is coupled to the AC RF power, causing the electrons to stay in the plasma for a longer duration. This results in higher plasma densities and increased ionization through collisions. Therefore, materials like silica, alumina can be easily deposited. During RF sputtering, the polarity of the cathode alternates, preventing the charges to accumulate on the cathode surface. Thus, facilitating the deposition of insulators. At the anode, the alternating potential is favourable for planarization through re-sputtering of the deposited film via sputter gun [2,14].

In recent times, the HiPIMS technique has been emerged as a more advanced sputtering method as compared to existing ones. The idea behind this method is to increase the plasma density afore the sputtering source, thereby reducing the mean ionization distance for sputtered particles. Instead of increasing the gas pressure in the chamber, HiPIMS achieves increased plasma density by applying high electrical power. The electrical power must be high enough to attain 10^{19}-10^{20} m^{-3} electron density in the periphery of the sputtering source.

However, supplying such high power with conventional cooling systems is challenging. Therefore, the remedy for this problem was to supply high power in the form of pulses. With power supplied in the form of pulses, average power can be maintained at a point where adequate cooling is available. It is advantageous to use HiPIMS, where dense coating morphology and tough film characteristics are required [15].

2.1.3 Chemical vapour deposition

Chemical vapour deposition (CVD) has garnered significant attention and popularity in both scientific and industrial communities. CVD is commonly used in the semiconductor industry due to its ability to produce high quality samples with minimal maintenance cost. It enables the growth of materials over larger areas. In general, the growth process involves, maintaining the substrate at higher temperatures and exposing it to volatile precursor/s. The elevated temperature facilitates the reaction or cracking of the precursor/s, leading to the deposition of the desired material onto the substrate [2].

Figure 2.3 shows the schematics of a CVD chamber commonly used in laboratories. It is advantageous as it allows controlled and selective growth of CNs on substrate as well as in bulk, at relatively low temperature as compared to other techniques [16].

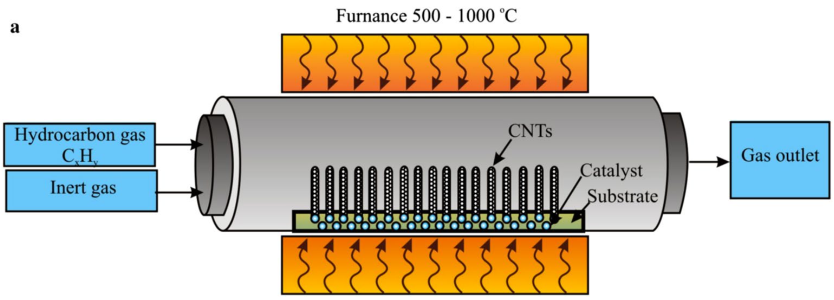

Figure 2. 3 Schematics of CVD system [16]

In the current project, catalytic CVD (CCVD) is used for the growth of carbon nanostructures (CNs). Therefore, our focus will be on the CCVD growth technique.

There are three steps involved in the synthesis of CNs, as shown in figure 2.4. These steps are explained as follow:

Step 1: *The substrate is coated with a catalytic layer*. Substrate and catalyst together play a very important role in the synthesis of CNs via CCVD. A catalyst is accelerating the reaction, so it is making it happen in acceptable conditions. There are two different types of substrates used depending on the application: conducting [17] and non-conducting substrates [18].

Deposition of catalyst directly onto the metal substrate can result in diffusion of catalytic material into the substrate forming alloys upon heating. Therefore, introduction of an appropriate buffer layer (a layer between substrate and catalyst) plays a critical role in synthesis of CNTs. Most used layers are oxides, like silica, alumina, and magnesium oxide [19,20].

Whereas, catalyst plays a very important role in defining the morphology, yield and quality of CNs. Catalyst helps lowering the cracking temperature of the hydrocarbon (HC) and provides nanosized templates for nucleation and growth of carbon nanotubes [21]. The utilization of low temperature CVD for the growth of high quality CNs harbours significant potential in various applications, since high temperature sometimes exceed the tolerance of the different materials and devices and can lead to the sintering of the catalyst.

Transition metals (Ni, Fe, Co) are frequently used as catalyst for the growth of CNs/CNT's [22]. These metals have shown high diffusion rate for C and high C solubility at elevated temperatures [23,24].

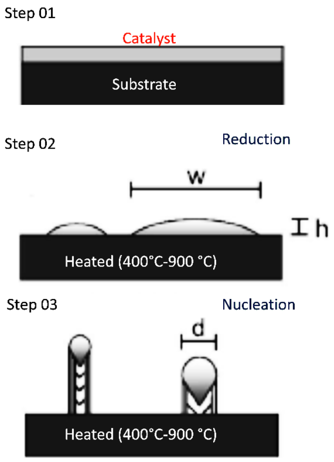

Figure 2. 4 Step 01: Deposition of catalyst, Step 02: Reduction of catalyst, Step 03: Nucleation after introduction of precursor gas [19]

Step 2: *Catalyst activation* - It is also referred to as thermal treatment of the catalytic film. Subjecting the catalytic film to a reducing gas such as hydrogen or ammonia at elevated temperatures yields several significant effects. Firstly, it leads to reduced island dimensions and a narrower distribution of these islands compared to the effect of mere film annealing. Furthermore, this process reduces the oxidized catalyst NPs. Both effects collectively enhance the efficiency of the catalyst film for CNs/CNTs growth [23,24].

Step 3: *Synthesis* - In the last step, precursors (most used are acetylene, ethylene, methane, and CO)[20] are introduced. In the presence of the active catalyst sites these HC decompose resulting in C dissolution into the catalytic metal site [2,19].

At this point one of the two mechanisms can happen as shown in figure 2.5: tip growth or base growth of CNTs. **Tip growth** is when the interaction of the catalyst with the substrate is weak. When the precursor is introduced in the chamber, it decomposes on top of the metal surface. The C diffuses inside and CNTs grow out, detaching the metal from the surface and pushing it away from the substrate. The growth will continue till the catalyst remains active. **Base growth** is a mechanism in which the interaction of the catalyst with the substrate is strong. After precursor decomposes, C diffuses into the metal site, and instead of pushing the metal particle up, CNTs are forced to move upward with catalyst well rooted with the substrate [25].

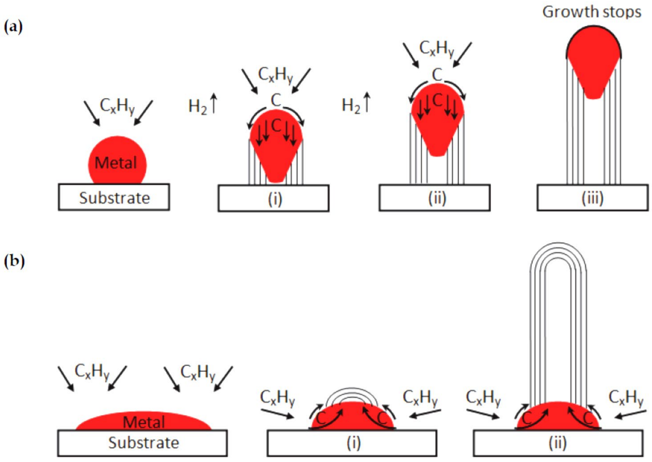

Figure 2. 5 a) Tip Growth mechanism: where the interaction of the catalyst is weak with the substrate and after C reaches super saturation it moves upward in the form of CNTs pushing the metal particle along the growth direction. b) Base Growth mechanism: the interaction of the catalyst is strong and after C reaches super saturation it moves up as CNT with strongly rooted catalyst at the base [25].

2.1.4 Supersonic Cluster Source (SCS)

Nanocluster are composed of 100 atoms and must have one dimension in the range of 1 – 10 nm and a narrow size distribution, whereas nanoparticles are composed of around 1000 atoms. Nanoclusters have been used in the field of catalysis, communication, microelectronics, sensors, biology and many more [26]. Within the scale of few nm, every atom has a significant influence on the electronic and chemical properties of the clusters. Therefore, controlled size and composition of nanoclusters will contribute to the advancement in the field of science and technology.

For the formation of nanoclusters, there are two methods:

Chemical method: Most of the chemical methods implement procedures like thermal decomposition, lithography, electro-chemical reduction, and cryo-chemical synthesis etc. It is preferred over physical method because of cost effectiveness, industrial friendly, and production with high yield. The drawback for chemical method is its hazardous effect on biological samples, and some chemicals are toxic and not environment friendly [26].

Physical method: This method is more commonly termed as cluster beam deposition. It has some advantages: the interaction between the metal cluster and the substrate can be adjusted by varying the energy of the impacting particles, they are prone to resist sintering at high temperatures and pressures, avoiding coalescence problems in catalysis, compared to chemical process they have less defects. Drawback of this method is that it is expensive, requires vacuum equipment, and lower yield [27].

There are six most used cluster beam sources. Basic difference between these sources is the method used to vaporize the material for cluster formation. Other differences are some have options to deliver power in pulses to the target and the injection of inert gas. Following is the list of cluster beam sources [28]:

1. Seeded supersonic nozzle source (SSNS)
2. Thermal gas aggregation source (TGAS)
3. Sputter gas aggregation source (SGAS)
4. Pulsed arc-cluster ion source (PACIS)
5. Laser ablation source (LAS)
6. Pulse micro-plasma cluster source (PMCS)

In this research we have used PMCS for the deposition of clusters, shown in figure 2.6. Therefore, a brief discussion on PMCS is as follow:

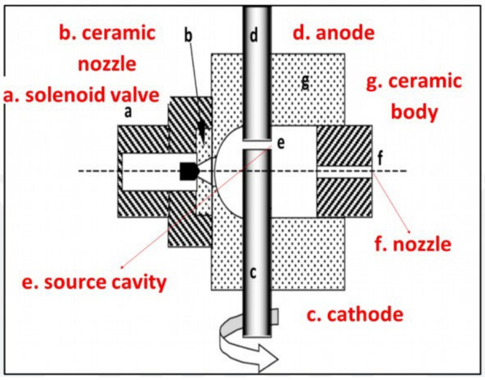

Figure 2. 6 Schematics of supersonic cluster source, a. solenoid valve, b. ceramic nozzle, c. cathode rotating to give uniform ablation, d. anode, e. source cavity, f. nozzle, g. ceramic body. illustrates that the source is encapsulated in a ceramic body, with two channels drilled into the body normal to the chamber. The material electrodes to be vaporized are inserted into these channels. He supersonic jet after entering the chamber, is ionized by supplying the pulse voltage (typical lasting 50 µs) to the electrodes, creating plasma. The plasma is directed towards the cathode, starting vaporization of the material, which later thermalizes and condenses, resulting in the formation of clusters on the substrate [29]

PMCS performs as a combination of LAS/PACIS and SGAS. Power to the target is supplied in pulses and the injection of inert gas is done in pulses that seeds and thermalizes the vapor. The target material is sputtered by plasma initiated by a discharge between an anode and the target [28].

PMCS, consists of a cylindrical cathode which is placed in ceramic frame for insulation. A channel pushing the supersonic gas jet perpendicularly towards the cathode. A pulse voltage is used to ionize the gas on its path towards the target. The target material is sputtered by the plasma produced by the discharge to form the vapor plume. Thermalization and condensations of the precursor takes place in the same chamber to form clusters. Therefore, solenoid valve is at the beginning of the channel, whereas a nozzle is placed at the end on the other side of the chamber wall. Through the nozzle the cluster beam will supersonically expand [30].

A large pressure gradient in the vicinity of the target restricts the plasma, confining sputtering to the area of 1 mm^2 of target, resulting in highly stable and intense vapour cloud. Because of the high pressure, direct sputtering of clusters take place. These clusters act as seeds for the further growth of clusters. As the sputtering/condensation cavity is only few cubic centimetres, with each pulse the change in average pressure is very extensive and a huge difference in pressure across the nozzle results in supersonic expansion of the aerosol into the neighbouring deposition chamber [31].

PMCS has many advantageous features making it fit for upscaling, as it has shown high flux, reliability, and reproducibility. It encompasses a wide range of materials like, carbon, oxides, and metals [28]. The reported flux rate for PMSC is 1-30 nm/s and typical cluster size is 10^1 - 10^4 atoms [27].

2.2 Tools for characterization

Prior to applying any material in practical applications, it is crucial to understand its electrical, thermal, chemical, and mechanical properties. In the current era of advanced science and technology, numerous sophisticated tools are available for studying samples ranging from atomic layer to microns in size. This section will delve into the instruments utilized in this research.

2.2.1 Photoemission spectroscopy

The basic principle of photoemission spectroscopy is photoelectric effect. Photoemission spectroscopies measure the kinetic energy (KE) distribution of the emitted photoelectrons when the material is irradiated with X rays. In a single particle picture, the observed electron's kinetic energy distribution mimics the energy distribution of occupied electron states in the ground state, referring to figure 2.7.

In a first approximation, the kinetic energy, E_K of the emitted photoelectron is:

$$\boldsymbol{E_K = h\nu - E_b - \emptyset_s} \qquad \textit{Equation 2. 1}$$

In this equation, h is the Planck's constant, $\boldsymbol{\nu}$ denotes the frequency of the incident photon, $\boldsymbol{E_b}$ is the binding energy (BE) of photoelectrons (PEs) relative to the Fermi level and $\boldsymbol{\emptyset_s}$is the work function of the sample.

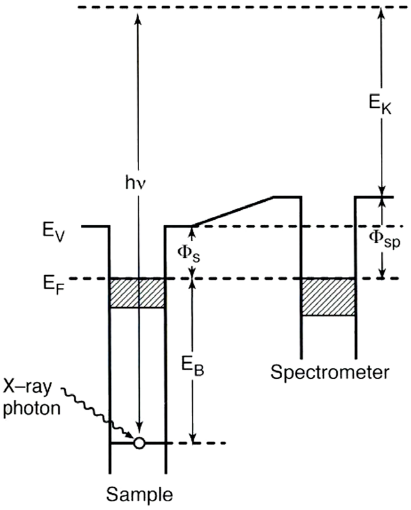

Figure 2. 7 Level diagram of photoemission process. [32]

To be detectable, to reach the electron energy analyser, a potential barrier $\emptyset = \emptyset_A - \emptyset_S$ needs to be overcome by the photoelectrons. In this case $\emptyset_A$ is the electron analyser's work function. Therefore, we can write equation 1 as:

$$\boldsymbol{E_K = h\nu - E_b - \emptyset_A} \qquad \text{Equation 2. 2}$$

Where EK depends only on $\emptyset_A$, and it is independent from the work function of the sample.

Despite photons may penetrate several micro-meters into the solid, photoemission is a surface sensitive technique because the sampling depth is governed by the mean free path of the photoelectrons which are able to leave the sample. This parameter follows the universal curve of the energy dependent inelastic mean free path of electrons in solids, varying as a function of KE of electron from 4 Å to 50 Å, as shown in Fig.2.8.

In a single particle approximation, on exposure to incoming photon flux, the current density of photoelectrons can be explained by using Fermi golden rule formula, where the matrix element, can be written in the dipole approximation as:

$$M_{fi} = < \varphi_f | \boldsymbol{A}\,\boldsymbol{p} + \boldsymbol{p}\,\boldsymbol{A} | \varphi_i > \qquad \text{Equation 2. 3}$$

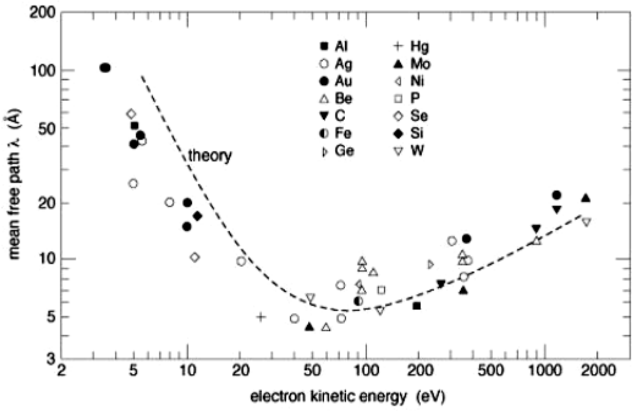

Figure 2. 8 Electrons mean-free path universal curve in solids as a function of their energy. [33]

In equation 1.3 the wave function for the final and initial electron state are φ_f and φ_i respectively. **A** represents the electromagnetic vector potential and the electron momentum is shown by **p** [32,34,35].

In first approximation, the photoemission spectrum gives the distribution of BEs of electron states within a solid. The information about the density of state is conveyed by the intensities of the photoemission structure, moreover it is affected by the cross sections of the photoemission processes involving electrons at different energy levels and by the transmission function of the electron energy analyser.

In figure 2.9, the measured photoemission spectrum displays well defined peaks, usually referred to as primary structures, superimposed on a background that is continuously increasing towards lower KE, exhibiting a big peak at low KE region. The background is recognised as the nearly continuous distribution of secondary electrons produced through scattering in solids, losing their initial energy information.

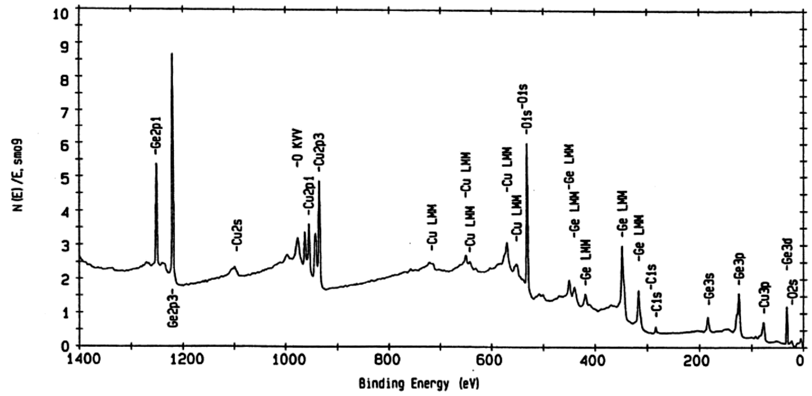

Figure 2. 9 Photoemission spectra from CuGeO3 single crystal [36]

The peaks with the highest intensities and sharp features refer to the electrons emitted from the core levels of the atoms within the solid. In general, soft x-rays are required for the excitation of the core electrons of most of the light elements, justifying the commonly used acronym for the technique, x-ray photoemission spectroscopy (XPS). Due to the discrete energies of the core levels, the position of a peak is the signature for a specific chemical element, thus, presenting photoemission spectroscopy an atom specific procedure. Handbooks are used as references as they contain all the database for the identification of core level [37]. An important fact is that the core level BE shift relies on the chemical bonds and local environment of atomic site. This enables the detection of the chemical state of an atom in an unknown solid system, utilizing the energy resolution and the definite core level shift.

The broad structure at the higher KEs of the photoemission spectrum relates to the energy distribution of the valence band states. The characteristic feature of these shallow states is their delocalized character, in comparison to the local nature of core levels. Hence, they are expected to distinctly change their distribution in energy as the chemical bonds are changed.

In the photoemission spectrum also other structures are visible, typically Auger peaks, shake up losses and correlation satellites due to relaxation processes, i.e., excitation and de-excitation of the system after the creation of the hole.

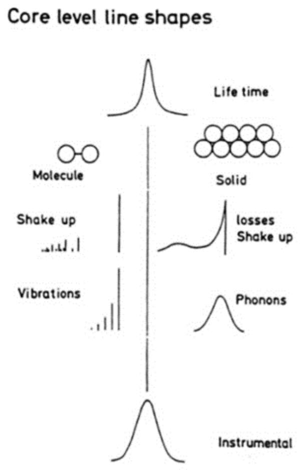

Figure 2. 10 Various contributions of the PE lines shape [35]

The photoemission core level width relies on various factors, shown in figure 2.10. Different contribution in the spectrum can be listed in the upcoming points [35]:

Mean lifetime of the photo-hole: An intrinsic width is related to all the core levels in photoemission spectrum. The mean lifetime of the holes generated during the photoemission is used to determine the width. The de-excitation of the hole takes place within the time span of 10^{-14} – 10^{-15} s. either by Auger or radiative processes, resulting in the peak width having Lorentzian line-shape.

Electronic excitation: All the electronic states of the system, modify by the creation of hole. This perturbation generates excited electronic states in the N -1 electrons system. Resulting in satellite peaks generally distinct from the core level, in molecules and insulating materials. Whereas, in metallic samples, where very small excitations can occur across the Fermi level can result in characteristic asymmetrical line shape of the photoemission peak towards lower KE [38].

Phonon coupling: The electron extraction from the solids usually results in the excitation of the vibrational modes of the system. This happens since the N electrons system's potential energy curve as a function of nuclear distance may vary when ionisation takes place. Two different cases are shown in figure 2.11: In both the cases lower curves show system before ionisation, which is the ground state. In the ground state it is assumed that the vibrational state v = 0 is populated. Whereas the higher curves in both the cases represent the excited state of the system. In excited state, Franck-Condon principle which is the direct consequence of the Born-Oppenheimer approximation [34,35,39], is utilized to know the transition probabilities of the vibrational states. In figure 2.11 a, before and after ionisation, the energy potential curves are nearly the same, due to small contribution by phonons to the photoemission peak. In figure 2.11 b, they are not the same, which is because of large contribution of phonons to the photoemission peak. In solids the broadening due to phonons has a Gaussian broadening.

Instrumental broadening: Because of the electron energy analyser's finite instrumental resolution and non-monochromatic light source, this is the most prominent broadening in photoemission spectrum. It contributes to the spectrum in the form of Gaussian broadening.

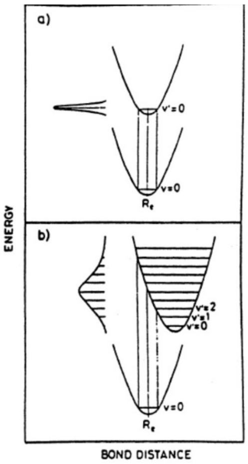

Figure 2. 11 Potential energy curves due to phonon contribution before and after ionization (a) same due to small phonon contribution (b) not the same due to large phonon contribution [39]

In Ultraviolet Photoelectron Spectroscopy (UPS) the source of photon is ultraviolet light instead of x-rays. Energy of these photons is lower (few to 100 eV) as compared to x-ray photons (100 eV – 100keV), and results in the ejection of valance band electrons rather than electrons from the core level. Figure 2.12 shows the schematics of the process.

UPS is not used for the elemental analysis or to identify the oxidation states but gives reliable information about the ionization energies of the valance shell electrons. Which facilitates in the understanding of interaction of a chemisorbate with surface or to study the band structure

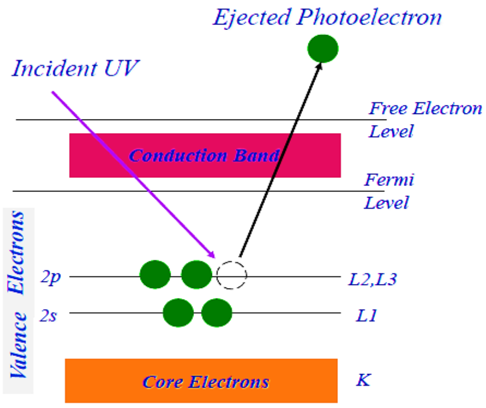

Figure 2. 12 Schematics of UPS.

of a semiconductor. Work function of the metal or semiconductors can also be calculated using UPS spectrum [40,41], using the following equation:

$$\emptyset = hv - SECO \qquad \text{Equation 2. 4}$$

Where ∅ is the work function, hv is the BE and SECO is the secondary electron cut off region.

Helium (He) discharge lamp is the most used source for UPS application. The most common emission lines in case of He discharge lamp are He I (21.22 eV) and He II (40.8 eV) [40,41].

The photoemission spectrum is number of PEs reaching the detector as a function of their KE. Modern day PE spectrometers are equipped with hemispherical sector analyser. These are fitted with inner and outer concentric hemispheres, when the volage is applied, they only allow the PEs of specific KE to pass through the analyser. PEs are slowed down by using retarding potential, which controls the KE of the electrons entering the analyser. Usually there are two ways in which pre-retardation of PEs is attained before they enter the analyser, i.e., CRR mode (constant retard ratio) or FAT (fixed analyser transmission) also known as CPE (constant pass energy) mode. CRR mode helps in reducing the original KE by a constant factor, whereas in CPE mode the scan of the KE is made changing the retarding potential. For XPS and UPS, FAT mode is preferred because of constant energy resolution and transmission efficiency, indifferent of the KE of the ejected PEs [40].

The facility in INSPECT lab in CNR-IOM, Trieste, was used for the XPS and UPS measurements, shown in figure 2.13. The instrument operates in UHV (base pressure~ 10^{-10}-10^{-11} mbar). It is equipped with two chambers: a sample preparation chamber and characterization chamber. Furthermore, the characterization chamber is equipped with

Hemispheric Analyzer of electrons (PSP 120 mm), x-ray source (hν = 1486.6 eV, hν =1253.6 eV, (ΔE ≈ 1.0 eV), UV lamp (hν = 21.2 eV, hν = 40.8 eV). The preparation chamber is fitted with plasma source, Low Energy Electron Diffraction (LEED), Residual Gas Analyzer (RGA), Evaporators, leak valve for the gas introduction and flux meter, ion gauge.

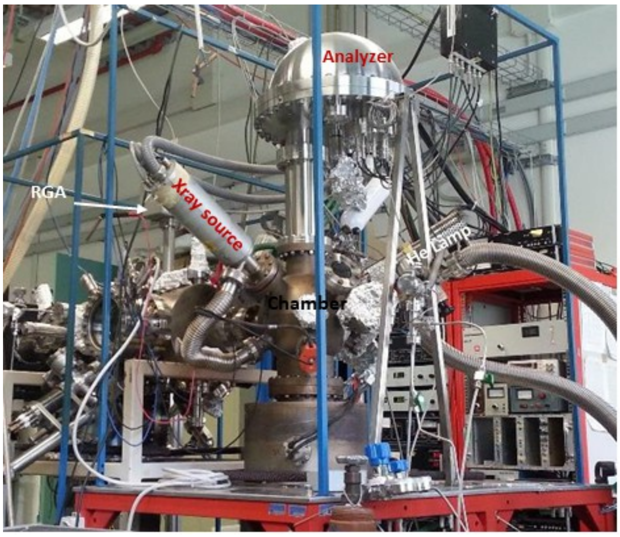

Figure 2. 13 Characterization and preparation chamber in INSPECT Lab, CNR-IOM, Trieste

2.2.2 Scanning Electron Microscopy (SEM)

SEM is a valuable tool for studying surface morphology of the sample. SEM can provide high-resolution images of a sample's surface, revealing details down to the nanometres scale.

Typically, tungsten filament is used to generate the electron beam by thermionic emission or field emission. To accelerate the electrons, the e-gun is operated with voltages from a few hundred volts to 30 KV. Electromagnetic lenses called condenser lenses are used to converge the e-beam into a probe. Objective lenses are used to facilitate the final demagnification and focusing of the beam on the sample. The beam moves along the surface of the sample by scanning coils [42]. The detectors are positioned above the sample. The detectors collect signals from each spot during the scan and convert the intensity of each pixel into an image. Figure 2.14 shows the schematics diagram of SEM.

When the electron beam interacts with the sample, it experiences the electric field of the neighbouring atoms. This interaction may lead to elastic or inelastic scattering of electrons, causing them to disperse laterally from the point of impact. Output signals generated by these electrons are the source of information in SEM [42].

SEM does not offer atomic resolution like its counterpart, transmission electron microscopy (TEM). However, SEM is not limited to compositional, morphological, or topographical studies alone. It can also be employed to detect surface fractures, crystal structures, and surface contaminations.

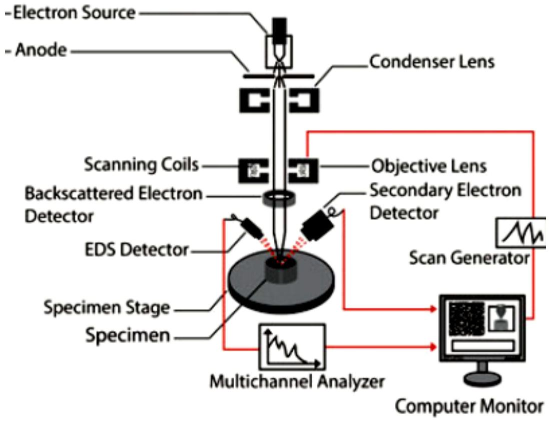

Figure 2. 14 Schematics of Scanning Electron Microscope [42]

The main advantage of SEM characterization is its ability to provide detailed 3D and topographical images. SEM is a user-friendly tool; sample preparation is much easier than TEM. With different detectors, versatile information about the sample can be extracted.

2.2.3 Atomic Force Microscopy (AFM)

AFM, a type of scanning probe microscopy, enables the investigation of both the conducting and insulating samples, providing true topographical images [43]. It offers a versatile platform for studying various sample types, including metals, soft materials, hard coatings, ceramics, biological and composites [44–47].

AFM is used to study the topography of surfaces on mesoscopic scales, by monitoring the Van der Waals interaction between the surface to be studied and a sharp tip, solidly connected to the end of a cantilever. The selection of the right cantilevers and tips is made depending on the type of sample to be characterized. Hard or soft cantilevers, differing from each other by their geometrical dimensions (typically in the μm scale), which dictates their spring constant and resonant frequency, can be employed depending on whether inorganic materials or soft matter samples are investigated. Cantilevers and tips are generally made of silicon or silicon nitride, however metallic (with diamond-like carbon) or magnetic (with Co-Cr alloys) coatings can be used to make them electrically conductive or magnetically sensitive. Finally, the tip can be shaped in a glass bead to facilitate nano-mechanical measurements [48].

The cantilever is suspended at one end (where the tip is attached) and raster or moves back and forth, up, and down trailing the profile of the sample, to build up an image. A laser is pointing at the back of the cantilever, which is reflected to a 4-quadrant photodiode, which can detect the motion of the cantilever both vertically and laterally. Figure 2.15 shows the schematics of AFM.

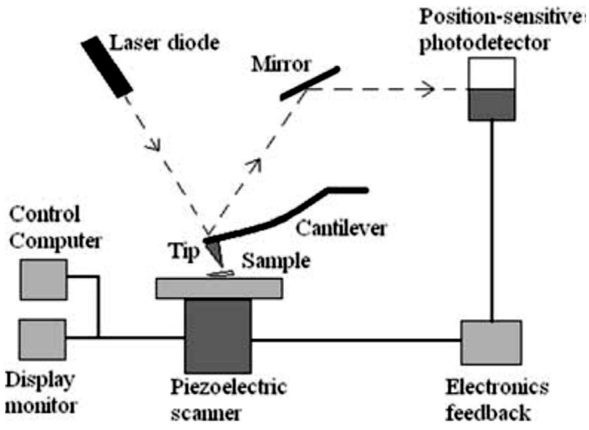

Figure 2. 15 Schematics of AFM [49]

As mentioned before, AFM measures the van der Waals force between the atoms at the end of the tip and the atoms on the surface of the sample. When the tip is brought closer to the sample, the probability of interaction between their relative atoms increases, and as they come closer their bonding potential energy will decrease from zero to a negative value, i.e., an attractive force arises. However, as they draw even closer, the force become repulsive, due to the overlapping between tip and sample electron orbitals – which is forbidden by the Pauli's principle - leading to a rapid increase in their bonding potential energy. These Van der Waals forces of attraction and repulsion as a function of tip distance are given by the derivative of the Lennard-Jones potential curve as shown in figure 2.16.

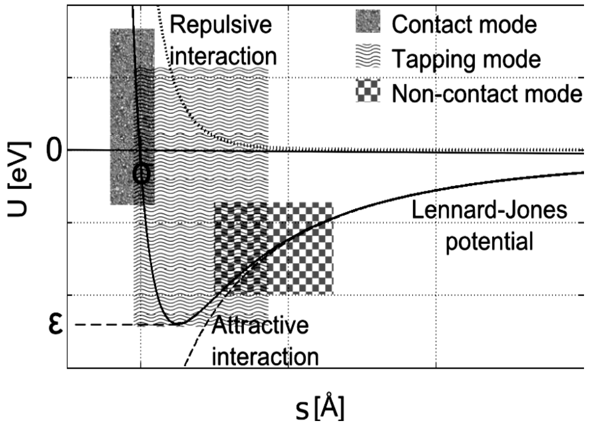

Figure 2. 16 AFM tip potential [50]

Mathematical expression is:

$$U_{(r_{ij})} = k\varepsilon[(\frac{\sigma}{r_{ij}})^n - (\frac{\sigma}{r_{ij}})^m] \qquad \text{Equation 2. 5}$$

Where n and m are the positive numbers, n>m, k is the constant, r_{ij} is the distance between the particles, σ is the interparticle distance where the potential changes its sign, and ε is the depth of the potential minimum. In case of atom-atom interaction, n=12 and m=6. However, these exponents are different when in presence of interaction between extended bodies.

AFM is used in different modes (shown in figure 2.17)

- Contact mode

The tip and the sample come in contact throughout the scan. In contact mode the chance is either of damaging the tip or spoiling the sample, especially if it is a soft or biological sample. But the best resolution is obtained using contact mode.

- Tapping mode (intermittent mode or AC mode)

It is a semi contact mode; it is designed to achieve high resolution with minimum chances of damaging the tip or the sample.

- Non-contact mode

In this mode the AFM tip is kept at few nm from the surface of the sample, i.e., in an attractive regime. With this mode the true atomic resolution is not attained, which can be achieved by working in pure repulsive regime (contact mode) [51].

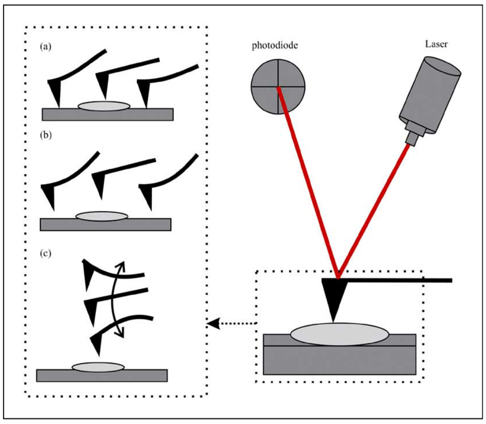

Figure 2. 17 Different modes of AFM, a. contact mode, b. non-contact mode, c. tapping mode [51]

2.2.4 Raman Spectroscopy (RS)

RS is a vibrational spectroscopic technique, which can be applied in various fields where non-destructive, microscopic, chemical analysis and imaging is required. RS measures scattered light from solid, liquid or sample in gaseous form [52].

A monochromatic electromagnetic radiation with $h\nu_o$ energy strikes the sample, either the radiation is absorbed, reflected, or scattered in different directions. There are two forms of scattered light, i.e., elastically scattered light also known as Rayleigh scattering, in which there is no net change in the energy of the incident and scattered photons. Then there is inelastic scattering, where there is a change in incoming and outgoing photons, called Raman scattering. The inelastic scattered photons either have frequency lesser ($h\nu_o$- $h\nu$) or greater ($h\nu$ + $h\nu_o$) than the incident radiations. Therefore, Raman scattering is subdivided into Stokes and Anti-Stokes shifts, shown in figure 2.18. Stokes shift occurs when the emitted photon has less energy as compared to the incident photon, whereas anti-stokes shift happens when the energy of the emitted photons is greater than the incident photons [52].

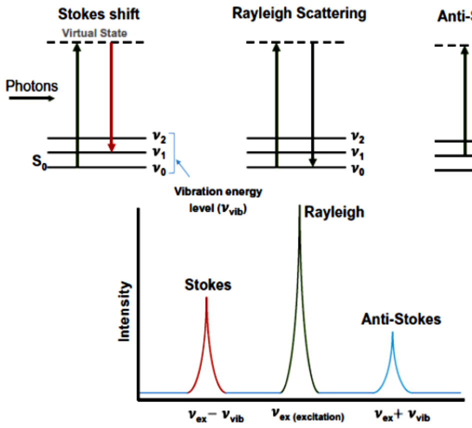

Figure 2. 18 Rayleigh, Stokes, and Anti-Stokes scattering [53]

The RS spectrum serves as a valuable tool for identifying different compounds based on their unique patterns. Therefore, for the unknown sample, the obtained spectrum of the sample can be used as a qualitative analysis. The sharper the peak more crystalline the material is, while a broader peak indicates that the material is more amorphous [52]. Other factors that can affect the broadening could be impurity, temperature, and stress.

Figure 2.19 illustrates the schematics of Raman spectrometer. RS consists of a monochromatic light source, a detector, and a sample holder. Several types of lasers are used as the source of excitation. The selected laser effects the Raman intensity, acquisition time, spatial resolution, background fluorescence, and cost of Raman system. Some of the lasers used are Helium-Neon laser (632.8nm), Nd-YAG (1064nm and 532nm) and Argon ion (488nm and 514.5nm) [52,54].

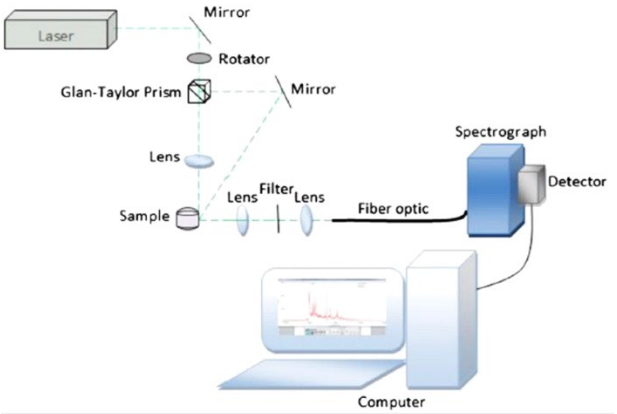

Figure 2. 19 Schematics of Raman Apparatus [54]

2.2.5 X-rays Diffraction (XRD)

XRD is a worldwide used tool to study the structures of solids. Application of XRD encompasses many fields in academic research as well as in industries [55,56].

Solids and crystals are classified into three distinct types: single crystal, poly-crystalline and amorphous, shown in figure 2.20. A single crystal is defined as the one having periodicity throughout their volume, in other words they have long range order. Poly-crystalline materials have short range periodicity, instead of whole volume they have order across individual grains. Amorphous materials have no or little ordered structure [57].

The wavelength of the x-rays is comparable to the interatomic distance of the crystal structure. Therefore, special interference, called diffraction is used to measure the distance between the atoms. Interference occurs either constructively or destructively when the emitted x-rays

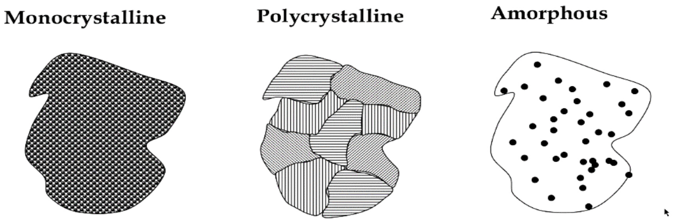

Figure 2. 20 Periodicity in monocrystalline, polycrystalline, and amorphous [58]

interact. When the x-rays strike the sample at a specific angle, where the scattered beam is interfering constructively giving rise to a peak, is called diffracted beam. This is well defined by Bragg's law (figure 2.21) given in equation 8. It is a simple equation and the basic working principle of XRD [57]:

$$n\lambda = 2dsin\theta \qquad \text{Equation 2. 6}$$

Where λ is the wavelength of the source used, d is the spacing between the plane family, and θ is the angle of incidence of the x-rays and n is an integer.

Constructive interference takes place when Bragg's law is satisfied at values of 'θ' and 'd.' XRD patterns represent the fingerprint image for a particular material. Therefore, the obtained scan is compared with the known pattern in the database. The structure and composition of the material can be determined using XRD. If a sample consists of multiple compounds, XRD can easily provide information about them [57].

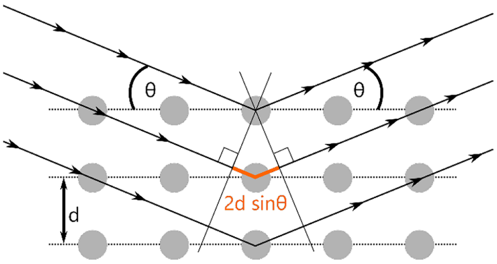

Figure 2. 21 geometrical representation of Bragg's law [59]

For characterizing the sample, it is placed in the instrument and illuminated with the beam of x-rays. Both the x-rays tube and the detector move in synchronized motion. The peaks attained corresponds to the atomic structure of the sample. Figure 2.22 shows the schematics of x-rays apparatus.

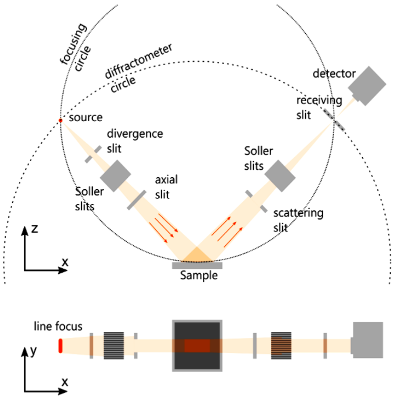

Figure 2. 22 Schematics of x-ray instrument [59]

The main advantages of XRD are that it is an excellent way to get information about structure and lattice parameters and is one of the fastest and most economical way to do so. It is a non-destructive technique. Sample preparation is easy. Several types of samples can be analysed, like powder, bulk, and thin films. From XRD, both qualitative and quantitative information can be extracted. Most measurements are done in ambient conditions.

2.3 Sample preparation

This section describes the synthesis of W based carbon nano-structed hybrid materials for the current project. First the focus will be on the synthesis of all the Carbon Nanostructures (CNs) (pebble-like carbon nanostructures and carbon nanotubes). All the technical details and experimental set up related to the growth, processing procedures and parameters will be discussed. Secondly deposition of tungsten (W) on the synthesized CNs and CNTs will be highlighted.

The synthesis of CNs was done by CCVD, as described earlier. For the deposition of tungsten DCMS and SCS were used, also explained in previous section.

For the synthesis of HM several experiments were conducted by varying: the material for catalyst, parameters of growth in CCVD, growth conditions for depositing tungsten through DCMS and W nanoclusters by PMCS. In this section we will exclusively deal with the experiments performed for the synthesis of HMs for this research work, characterization of the samples at every step will be discussed in the subsequent chapters. Following is the order in which we will proceeded in this section.

1. Deposition of a catalyst via e-beam evaporator.
2. Growth of CNs/CNTs through CCVD
3. Deposition of W/WO_x on bare Si(100) as well as on CNs/CNTs using DCMS
4. Deposition of W on bare Si(100) as well as on CNTs by PMCS

2.3.1 Deposition of catalyst via e-beam

A commercial wafer of SiO_2(250 nm)/Si(111) was used as substrate for depositing Nickel (Ni) as a catalyst for CNs growth. Whereas SiO_2(250 nm)/Si(100) and Al_2O_3 (7.5 nm)/Si(100) were used as substrates for depositing Iron (Fe) as a catalyst for CNTs growth.

Also, as has been highlighted earlier in this chapter, for CCVD, role of catalyst is very crucial during the growth of CNTs/CNs. It provides a nanoscale template for the nucleation and growth of CNTs/CNs and helps in lowering the cracking temperature of the precursor gas. In this work Ni and Fe have been used as catalysts for the growth of CNs/CNTs.[60–62] Both the selected catalysts are 3d metals and are reported to show better catalytic behaviour for carbon compound decomposition, formation of carbides and for the rapid diffusion of carbon through the metal. They show finite solubility for carbon at specific temperatures. After the cracking of gas molecules, carbon diffuses into the catalyst particles, resulting in the supersaturation of carbon in the metal.

Fe and Ni were deposited on different substrates via e-beam.

Before deposition, basic cleaning procedure of the substrate was done. The whole wafer was placed in (96% pure) ethanol ultrasonic bath for 5 min, rinsed in deionized water and dried using nitrogen. After cleaning, the wafer was mounted on the sample holder and placed in the e-beam vacuum chamber. The system was evacuated to a base pressure of about 2x10^{-6} mbar. Catalyst deposition was done keeping the substrate at room temperature (RT), a microbalance was used to measure the thickness of the film. Catalyst material (source) was placed in a ceramic crucible, placed in one of the grooves of water-cooled stage. The distance between the source and the stage was 30 cm. E-beam was used to evaporate the catalyst. 1.5 nm of catalyst (Fe or Ni) was deposited by maintaining the growth rate of 0.1 Å/s.

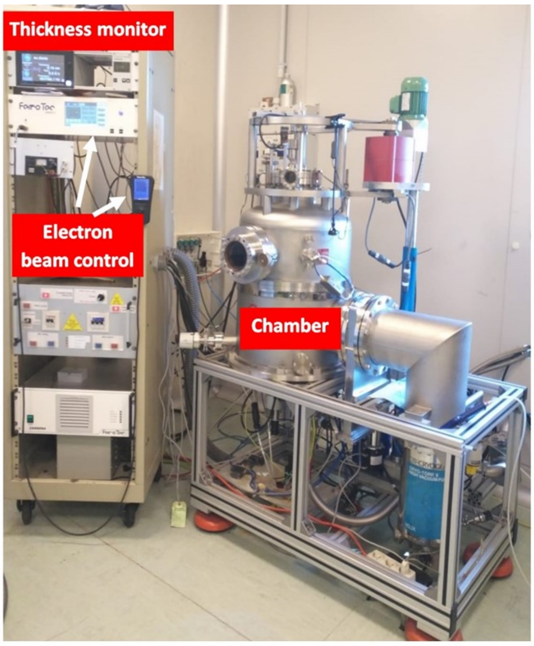

Figure 2. 23 E-beam instrument at the nano fabrication facility at IOM-CNR, Basovizza, Trieste, Italy

2.3.2 Catalytic Chemical Vapour Deposition (CCVD): Catalyst pre-treatment and CVD synthesis:

A homemade CVD chamber as shown in figure 2.24 is used to grow CNTs/CNs. It is equipped with a flow meter to have better control of gas flow. The resistive heater is used to heat the substrates, and a thermocouple is used to measure the temperature of the heater. With this set up 900 °C can be easily reached. Hydrogen (H_2) was used as a reducing agent. As a precursor gas acetylene (C_2H_2) was used. Four different temperatures of growth were finalized for the growth of CNTs/CNs. These temperatures were varied in a step of 100 °C from 400 °C to 700 °C. All other parameters like time for thermal treatment (TT) of the sample (5 mins), flow rate of H_2 during TT (100 sccm), time of growth (5 mins), the flow rate of gases during growth (H_2: 100 sccm, C_2H_2: 100 sccm), and pressure (~2.84 X 10^{-1} mbar) were kept constant.

It should be noted that the temperature for TT and growth is the same.

Once the required temperature is attained, as a first step hydrogen is fluxed for 5 min at the flow rate of 100 sccm maintaining 1.86 X 10^{-2} mbar pressure. Then after 5 min, along with hydrogen (100 sccm), acetylene at 100 sccm flow rate was introduced in the chamber for 5 min. The pressure of the chamber increased to 2.2 X 10^{-1} mbar. After 5 min, heating and gases flux were stopped. The system was allowed to cool down to 80 °C or below before the samples were removed.

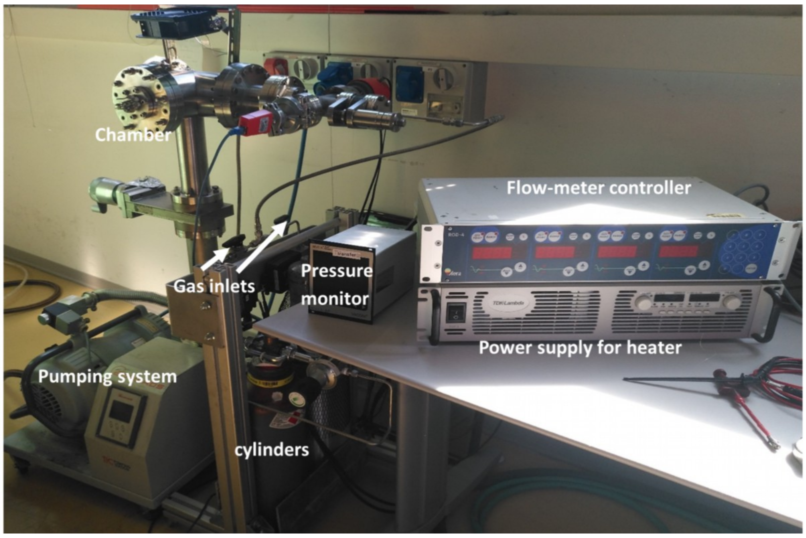

Figure 2. 24 Homemade CVD equipment facility at surface science laboratory elettra, Basovizza, Trieste, Italy

To grow CNT forest with **varying length**, we studied the effect of the CVD time of growth, keeping all the parameters same as given above with 600 °C as constant temperature. We varied the time of growth from 15 s to 1500 s.

To further explore the possibility to achieve increased length of CNTs, flow rate of acetylene was reduced from 100 sccm to 80 sccm at different growth times, keeping the pre-treatment parameters and other growth parameters the same as above.

Lastly, parameter that was changed was chamber pressure for growth by closing the backing valve. Parameters used for the TT are the same as above, whereas during growth cycle the pressure of the chamber was varied from 0.44 X 10^{-1} to 12.3 X 10^{-1} mbar, initially increasing by 0.22 X 10^{-1} mbar till 0.88 X 10^{-1} mbar and then we synthesized at higher pressure of 5.5 X 10^{-1} mbar and 12.3 X 10^{-1} mbar. All other parameters during growth were constant, growth time for all the samples was 150 mins.

2.3.3 Deposition of W via DC Magnetron Sputtering

The chamber was equipped with three 6 inches disc-shaped targets, 40 cm apart. These targets were placed parallel to the base of the chamber. Substrates were placed on a rotating plate furnished with 6 stages to have multiple growths. The distance between the stage and the target was 8 cm. This distance can be reduced, but not increased. Underneath the plate, steel support was fixed to facilitate six bulb heaters (250W), used for heating the substrates. There was also a provision to supply negative biasing to the substrate. Negative biasing was supplied by using an external DC generator.

W and WO_x films were deposited on bare Si(100) substate, to optimize the time of growth, flow rate of gas/gases (Ar/O_2) and power for depositing 100 nm of W and WO_x films. Si substrates were placed in the middle of the sample holder, The procedure is explained as:

W film was deposited using DCMS from 99.95% pure, 6 inches diameter W target onto Si(100) substrate. The substrate was cleaned using the procedure already discussed earlier. 100 nm of W film was deposited using pure Ar plasma. The base pressure was 2.6 X 10^{-5} mbar. Before deposition, the target was pre-sputtered for 1 min at 300 W, in a pure Ar environment at working pressure of 8.4 X 10^{-4} mbar. Flow rate of Ar was set to 23 sccm for the pre-sputtering as well as for sputtering processes. During deposition the substrate was kept at RT and was grounded. The rate of deposition during the sputtering process was 0.4 nm/s.

For depositing 100 nm WO_x, the process was same as discussed above, but here along with Ar, O_2 was also introduced in the chamber at RT. Flow rate of Ar was 20 sccm and of O_2 was 3 sccm during deposition. The rate of deposition during the sputtering process was 0.4 nm/s

For depositing 100 nm W and WO_x on CNs/CNTs all the parameters mentioned above were kept constant. However, during growth process some of the samples were grown by applying biasing to the substrate:

- Deposited without biasing.
- -50V was applied to the substrate during the growth

Biasing affects the grain size of the particles constitutes the film.[63,64] For further deposition of W on CNTs -50 V was the selected biasing for the substrate. Details of which will be discussed in chapter 5.

Different thicknesses (100 nm, 200 nm, 500 nm) of the W film were deposited on the forest by sequentially adjusting the substrate temperature and power.

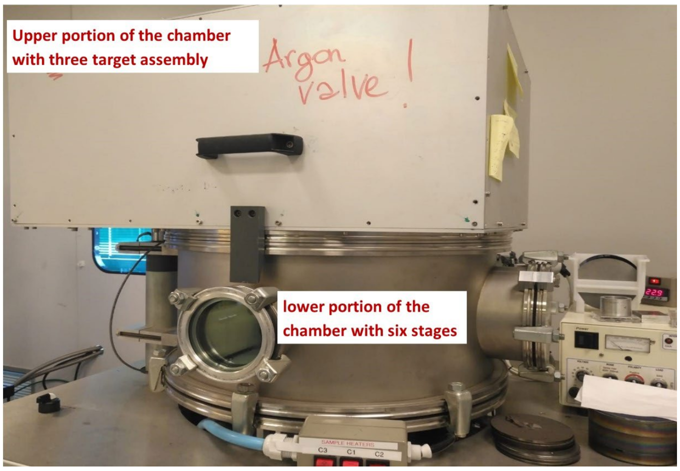

Figure 2. 25 Sputtering unit at the nano fabrication facility at IOM-CNR, Basovizza, Trieste, Italy

2.3.4 Supersonic cluster source:

The supersonic cluster source apparatus consisted of multiple compartments, each serving a specific purpose. The instrument operated under low vacuum conditions (10^{-7} mbar). The first chamber contained the beam source, connected to the gas supply via a solenoid valve and a ceramic nozzle. The solenoid valve was backed with high gas pressure (8-25 bar). The characteristic of the generated beam was determined by the pressure difference, as well as the shape and size of the nozzle. Typically, the compartment maintains the pressure of 10^{-7} mbar.

The solenoid valve delivered helium (He) pulses to the source, with an opening time of a few hundred µs. As the pulsed valve closed, the pressure in the source cavity matched the vacuum in the first compartment, i.e., 10^{-7} mbar. When the valve opened, He entered the chamber as supersonic jet due to the significant pressure difference. As the He supersonic jet entered the chamber, it was focused on one of the electrodes (cathode). The electrodes were supplied with pulsed voltage (typical lasting 50 µs), ionized the gas, and created plasma. The plasma was directed towards the cathode, which initiated vaporization of the material, which subsequently thermalized and condensed, forming clusters on the substrate [31,65].

Schematics of the PMSC is already shown in figure 2.6.

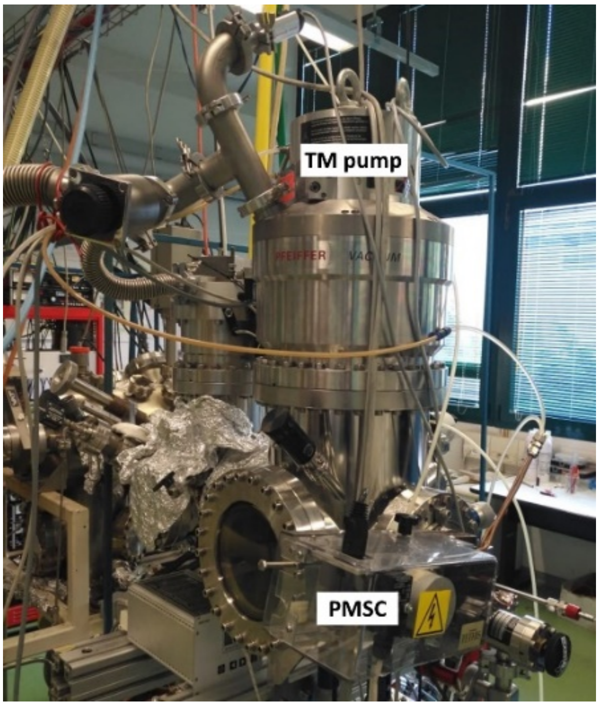

Figure 2. 26 Supersonic cluster source equipped with in-situ XPS and UPS measurement in INSPECT lab, TASC laboratory, CNR-IOM, Basovizza, Trieste, Italy.

2.4 Experimental setup for gas sensing

The sample's electrical resistance has been measured at RT in UHV conditions (base pressure: about $2x10^{-9}$ mbar) using a conventional multi-meter connected to the samples through the sample holder (see figure 2.27). The electric contact has been done through two tantalum foils in direct contact with two sample's borders (contact area: about 1x5 mm^2). For all samples, before EtOH dosing, the stability of the resistance was measured, the stability of the resistance was measured.

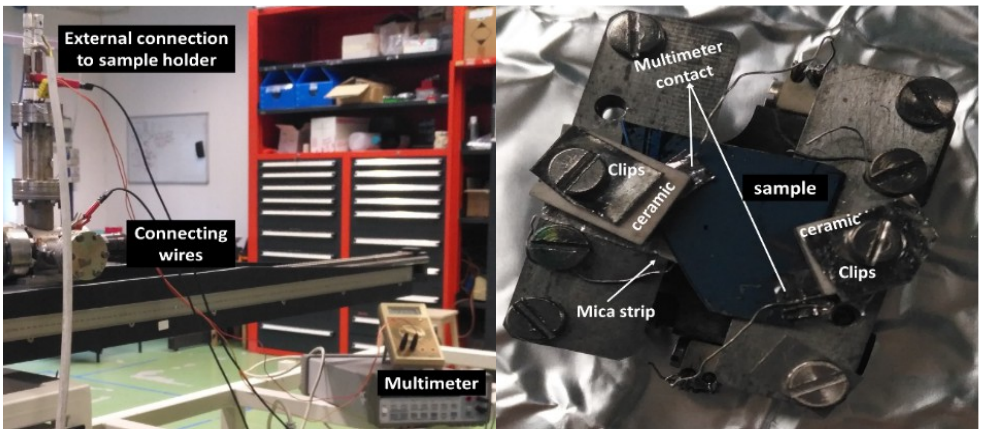

Figure 2.27 (left) The external connection of the sample holder with the multi-meter, (right) sample holder and the components used to fix the sample on it

2.5 Reference

[1] Z. Wang, Z. Zhang, Electron Beam Evaporation Deposition, in: Lin Yuan, Chen Xin (Eds.), Advanced Nano Deposition Methods, 01 ed., Chemical Industry Press., 2016: pp. 33–58. https://doi.org/10.1002/9783527696406.ch2.

[2] H. Frey, H.R. Khan, Handbook of Thin-Film Technology, Springer Berlin Heidelberg, 2015. https://doi.org/10.1007/978-3-642-05430-3.

[3] Awan Tahir, Basir Almas, Tehseen Aqsa, Chemistry of Nanomaterials, Elsevier, 2020. https://doi.org/10.1016/C2018-0-04648-4.

[4] K. Von Niessen, M. Gindrat, Plasma spray-PVD: A new thermal spray process to deposit out of the vapor phase, Journal of Thermal Spray Technology 20 (2011) 736–743. https://doi.org/10.1007/s11666-011-9654-9.

[5] Z. Zheng, J. Wang, P. Bi, J. Ren, Y. Wang, Y. Yang, X. Liu, S. Zhang, J. Hou, Tandem Organic Solar Cell with 20.2% Efficiency, Joule 6 (2022) 171–184. https://doi.org/10.1016/j.joule.2021.12.017.

[6] P. Melpignano, C. Cioarec, R. Clergereaux, N. Gherardi, C. Villeneuve, L. Datas, E-beam deposited ultra-smooth silver thin film on glass with different nucleation layers: An optimization study for OLED micro-cavity application, Org Electron 11 (2010) 1111–1119. https://doi.org/10.1016/j.orgel.2010.03.022.

[7] K. Askar, B.M. Phillips, Y. Fang, B. Choi, N. Gozubenli, P. Jiang, B. Jiang, Self-assembled self-cleaning broadband anti-reflection coatings, Colloids Surf A Physicochem Eng Asp 439 (2013) 84–100. https://doi.org/10.1016/j.colsurfa.2013.03.004.

[8] A.H. Simon, Sputter Processing, in: Handbook of Thin Film Deposition: Fourth Edition, Elsevier, 2018: pp. 195–230. https://doi.org/10.1016/B978-0-12-812311-9.00007-4.

[9] M. Qadir, Y. Li, C. Wen, Ion-substituted calcium phosphate coatings by physical vapor deposition magnetron sputtering for biomedical applications: A review, Acta Biomater 89 (2019) 14–32. https://doi.org/10.1016/j.actbio.2019.03.006.

[10] A. Baptista, F.J.G. Silva, J. Porteiro, J.L. Míguez, G. Pinto, L. Fernandes, On the Physical Vapour Deposition (PVD): Evolution of Magnetron Sputtering Processes for Industrial Applications, in: Procedia Manuf, Elsevier B.V., 2018: pp. 746–757. https://doi.org/10.1016/j.promfg.2018.10.125.

[11] M.M. Hassan, Antimicrobial coatings for textiles, in: Handbook of Antimicrobial Coatings, Elsevier, 2017: pp. 321–355. https://doi.org/10.1016/B978-0-12-811982-2.00016-0.

[12] Milton Ohring, Material Science of Thin Films, Academic Pres, 1992.

[13] P.J. Kelly, R.D. Arnell, Magnetron sputtering: a review of recent developments and applications, Vacuum 56 (2000) 159–172. https://doi.org/10.1016/S0042-207X(99)00189-X.

[14] Encyclopedia of Tribology, Springer US, 2013. https://doi.org/10.1007/978-0-387-92897-5.

[15] Mattias. Samuelsson, Fundamental Aspects of HiPIMS under Industrial Conditions, Linkoping University, 2012.

[16] O. Zaytseva, G. Neumann, Carbon nanomaterials: Production, impact on plant development, agricultural and environmental applications, Chemical and Biological Technologies in Agriculture 3 (2016). https://doi.org/10.1186/s40538-016-0070-8.

[17] E. Roumeli, M. Diamantopoulou, M. Serra-Garcia, P. Johanns, G. Parcianello, C. Daraio, Characterization of vertically aligned carbon nanotube forests grown on stainless steel surfaces, Nanomaterials 9 (2019). https://doi.org/10.3390/nano9030444.

[18] G.Y. Xiong, D.Z. Wang, Z.F. Ren, Aligned millimeter-long carbon nanotube arrays grown on single crystal magnesia, Carbon N Y 44 (2006) 969–973. https://doi.org/10.1016/j.carbon.2005.10.015.

[19] C. Mattevi, C.T. Wirth, S. Hofmann, R. Blume, M. Cantoro, C. Ducati, C. Cepek, A. Knop-Gericke, S. Milne, C. Castellarin-Cudia, S. Dolafi, A. Goldoni, R. Schloegl, J. Robertson, In-situ X-ray photoelectron spectroscopy study of catalyst-support interactions and growth of carbon nanotube forests, Journal of Physical Chemistry C 112 (2008) 12207–12213. https://doi.org/10.1021/jp802474g.

[20] K.A. Shah, B.A. Tali, Synthesis of carbon nanotubes by catalytic chemical vapour deposition: A review on carbon sources, catalysts and substrates, Mater Sci Semicond Process 41 (2016) 67–82. https://doi.org/10.1016/j.mssp.2015.08.013.

[21] M. Ahmad, S.R.P. Silva, Low temperature growth of carbon nanotubes – A review, Carbon N Y 158 (2020) 24–44. https://doi.org/10.1016/j.carbon.2019.11.061.

[22] H. Ur Rashid, K. Yu, M. Naveed Umar, M. Naveed Anjum, K. Khan, N. Ahmad, M. Tariq Jan, CATALYST ROLE IN CHEMICAL VAPOR DEPOSITION (CVD) PROCESS: A REVIEW, Rev. Adv. Mater. Sci 40 (2015) 235–248.

[23] G.N. Ayre, T. Uchino, B. Mazumder, A.L. Hector, J.L. Hutchison, D.C. Smith, P. Ashburn, C.H. De Groot, On the mechanism of carbon nanotube formation: The role of the catalyst, Journal of Physics Condensed Matter 23 (2011). https://doi.org/10.1088/0953-8984/23/39/394201.

[24] A. Malesevic, H. Chen, T. Hauffman, A. Vanhulsel, H. Terryn, C. Van Haesendonck, Study of the catalyst evolution during annealing preceding the growth of carbon

nanotubes by microwave plasma-enhanced chemical vapour deposition, Nanotechnology 18 (2007). https://doi.org/10.1088/0957-4484/18/45/455602.

[25] A. Venkataraman, E.V. Amadi, Y. Chen, C. Papadopoulos, Carbon Nanotube Assembly and Integration for Applications, Nanoscale Res Lett 14 (2019). https://doi.org/10.1186/s11671-019-3046-3.

[26] G. Peng, Z. e. Huma, M. Umair, I. Hussain, I. Javed, Nanosilver at the interface of biomedical applications, toxicology, and synthetic strategies, in: Metal Nanoparticles for Drug Delivery and Diagnostic Applications, Elsevier Inc., 2019: pp. 119–139. https://doi.org/10.1016/B978-0-12-816960-5.00008-2.

[27] G. Sanzone, J. Yin, H. Sun, Scaling up of cluster beam deposition technology for catalysis application, Front Chem Sci Eng 15 (2021) 1360–1379. https://doi.org/10.1007/s11705-021-2101-7.

[28] J.A. De Toro, P.S. Normile, C. Binns, Gas-Phase Synthesis of Nanoparticles, First, Wiley-VCH Verlag GmbH & Co., 2017.

[29] H. Vahedi Tafreshi, P. Piseri, G. Benedek, P. Milani, The role of gas dynamics in operation conditions of a puised microplasma cluster source for nanostructured thin films deposition, J Nanosci Nanotechnol 6 (2006) 1140–1149. https://doi.org/10.1166/jnn.2006.139.

[30] H.V. Tafreshi, P. Piseri, E. Barborini, G. Benedek, P. Milani, Simulation on the effect of Brownian motion on nanoparticle trajectories in a pulsed microplasma cluster source, Journal of Nanoparticle Research 4 (2002) 511–524.

[31] P. Milani, P. Piseri, E. Barborini, A. Podesta, C. Lenardi, Cluster beam synthesis of nanostructured thin films, Journal of Vacuum Science & Technology A: Vacuum, Surfaces, and Films 19 (2001) 2025–2033. https://doi.org/10.1116/1.1331289.

[32] D. Briggs (Editor), M. P. Seah (Editor), Practical Surface Analysis, Auger and X-ray Photoelectron Spectroscopy (Volume 1), Wiley, 1990.

[33] M.P. Seah, W.A. Dench, Quantitative Electron Spectroscopy of Surfaces: A Standard Data Base for Electron Inelastic Mean Free Paths in Solids, Wiley, 1979. https://doi.org/10.1002/sia.740010103.

[34] N.W.Ashcroft and N.D.Mermin, Solid State Physics, Harcourt, Inc, 1976.

[35] N. Martensson, A. Nilsson, Core-Level Line Shapes of Adsorbates: Effects of Electronic and Vibrational Excitations, J Electron Spectros Relat Phenomena 52 (1990) 1–46. https://doi.org/10.1016/0368-2048(90)85001-P.

[36] V. Corradini, A. Goldoni, F. Parmigiani, C. Kim, A. Revcolevschi, L. Sangaletti, U. Del Pennino, Surface gap and surface electronic states in CuGeO 3 single crystal, 1999.

[37] J.F. Moulder, W.F. Stickle, P.E.' Sobol, K.D. Bomben, J. Chastain, Handbook of X-ray Photoelectron Spectroscopy AReference Book of Standard Spectra for Identification and Interpretation of XPS Data, Perkin Elmer corporation Physical Electronics Division, 1992.

[38] S. Doniacht, M. Sunjic$, Many-electron singularity in x-ray photoemission and x-ray line spectra from metals, Journal of Physics C: Solid State Physics 3 (1970) 285. https://doi.org/10.1088/0022-3719/3/2/010.

[39] A. Zangwill, Physics at Surfaces, Cambridge University Press, 1988. https://doi.org/10.1017/CBO9780511622564.

[40] J.E. Whitten, Ultraviolet photoelectron spectroscopy: Practical aspects and best practices, Applied Surface Science Advances 13 (2023). https://doi.org/10.1016/j.apsadv.2023.100384.

[41] D.A. Zatsepin, A.F. Zatsepin, Ultraviolet Photoelectron Spectroscopy-Materials Science Technique, 2021.

[42] A. Ul-Hamid, A Beginners' Guide to Scanning Electron Microscopy, Springer Nature, 2018. https://doi.org/10.1007/978-3-319-98482-7.

[43] G. Binnig, C.H. Gerber, E. Stoll, T.R. Albrecht, C.F. Quate, Atomic Resolution with Atomic Force Microscope, 1987.

[44] Y.F. Dufrêne, T. Ando, R. Garcia, D. Alsteens, D. Martinez-Martin, A. Engel, C. Gerber, D.J. Müller, Imaging modes of atomic force microscopy for application in molecular and cell biology, Nat Nanotechnol 12 (2017) 295–307. https://doi.org/10.1038/nnano.2017.45.

[45] N. Alharbi, S. Teerakanok, J.D. Satterthwaite, R. Giordano, N. Silikas, Quantitative nano-mechanical mapping AFM-based method for elastic modulus and surface roughness measurements of model polymer infiltrated ceramics, Dental Materials 38 (2022) 935–945. https://doi.org/10.1016/j.dental.2022.03.002.

[46] M.L. Oyen, R.F. Cook, A practical guide for analysis of nanoindentation data, J Mech Behav Biomed Mater 2 (2009) 396–407. https://doi.org/10.1016/j.jmbbm.2008.10.002.

[47] K.W. Shinato, F. Huang, Y. Jin, Principle and application of atomic force microscopy (AFM) for nanoscale investigation of metal corrosion, Corrosion Reviews 38 (2020) 423–432. https://doi.org/10.1515/corrrev-2019-0113.

[48] K.H. Chung, Wear characteristics of atomic force microscopy tips: A reivew, International Journal of Precision Engineering and Manufacturing 15 (2014) 2219–2230. https://doi.org/10.1007/s12541-014-0584-6.

[49] H. Yang, Y. Wang, S. Lai, H. An, Y. Li, F. Chen, Application of atomic force microscopy as a nanotechnology tool in food science, J Food Sci 72 (2007). https://doi.org/10.1111/j.1750-3841.2007.00346.x.

[50] S. Babicz, J. Smulko, A. Zieliński, Enhancing capabilities of Atomic Force Microscopy by tip motion harmonics analysis, Bulletin of the Polish Academy of Sciences: Technical Sciences 61 (2013) 535–539. https://doi.org/10.2478/bpasts-2013-0053.

[51] M. Veerapandian, K. Yun, Study of Atomic Force Microscopy in Pharmaceutical and Biopharmaceutical Interactions - A Mini Review, Curr Pharm Anal 5 (2009) 256–268. https://doi.org/10.2174/157341209788922020.

[52] N. John, S. George, Raman Spectroscopy, in: Spectroscopic Methods for Nanomaterials Characterization, Elsevier, 2017: pp. 95–127. https://doi.org/10.1016/B978-0-323-46140-5.00005-4.

[53] Y.C. Cho, S. Il Ahn, Fabricating a Raman spectrometer using an optical pickup unit and pulsed power, Sci Rep 10 (2020). https://doi.org/10.1038/s41598-020-68650-7.

[54] F. Matroodi, S.H. Tavassoli, Simultaneous Raman and laser-induced breakdown spectroscopy by a single setup, Appl Phys B 117 (2014) 1081–1089. https://doi.org/10.1007/s00340-014-5929-4.

[55] M. Serhan, M. Sprowls, D. Jackemeyer, M. Long, I.D. Perez, W. Maret, N. Tao, E. Forzani, Total iron measurement in human serum with a smartphone, in: AIChE Annual Meeting, Conference Proceedings, American Institute of Chemical Engineers, 2019. https://doi.org/10.1039/x0xx00000x.

[56] A. Chauhan, Powder XRD Technique and its Applications in Science and Technology, J Anal Bioanal Tech 5 (2014). https://doi.org/10.4172/2155-9872.1000212.

[57] B. D. . Cullity, S.R. Stock, Elements of X-RAY Diffraction, third, PEARSON, 2014.

[58] ECE 209 Notes, https://csclub.uwaterloo.ca/~matedesc/exam-notes.html, (2010).

[59] G.F. Harrington, J. Santiso, Back-to-Basics tutorial: X-ray diffraction of thin films, J Electroceram 47 (2021) 141–163. https://doi.org/10.1007/s10832-021-00263-6.

[60] K.T. Ng, D.M. Hercules, Studies of Nickel-Tungsten-Alumina Catalysts by X-Ray Photoelectron Spectroscopy, J Phys Chem 80 (1976). https://pubs.acs.org/sharingguidelines.

[61] S.Y. Lee, M. Yamada, M. Miyake, Synthesis of carbon nanotubes over gold nanoparticle supported catalysts, Carbon N Y 43 (2005) 2654–2663. https://doi.org/10.1016/j.carbon.2005.05.045.

[62] S. Hofmann, R. Blume, C.T. Wirth, M. Cantoro, R. Sharma, C. Ducati, M. Hävecker, S. Zafeiratos, P. Schnoerch, A. Oestereich, D. Teschner, M. Albrecht, A. Knop-Gericke, R. Schlögl, J. Robertson, State of transition metal catalysts during carbon nanotube growth, Journal of Physical Chemistry C 113 (2009) 1648–1656. https://doi.org/10.1021/jp808560p.

[63] J. Shi, D. Kojima, M. Hashimoto, The interaction between platinum films and silicon substrates: Effects of substrate bias during sputtering deposition, J Appl Phys 88 (2000) 1679–1683. https://doi.org/10.1063/1.373871.

[64] H. Wang, S. Zhang, Y. Li, D. Sun, Bias effect on microstructure and mechanical properties of magnetron sputtered nanocrystalline titanium carbide thin films, Thin Solid Films 516 (2008) 5419–5423. https://doi.org/10.1016/j.tsf.2007.07.022.

[65] E. Barborini, P. Piseri, P. Milani, A pulsed microplasma source of high intensity supersonic carbon cluster beams, J. Phys. D: Appl. Phys 32 (1999) 105–109.

CHAPTER No. 3

Carbon Nanostructures/ Carbon Nanotubes growth and characterization

In this chapter we characterize the obtained CNs (synthesis described in chapter 2) to serve as a template for the synthesis of W/C hybrid materials. These CNs were obtained via CCVD by exploiting the already available literature, as discussed in the previous chapters.

This Chapter is divided into two main parts:

- The first part encompasses the characterization of CNs grown on (250 nm) SiO_2/Si commercially available substrate and Nickel (Ni) as the catalyst.
- The second part incorporates the characterization of CNTs synthesized on (250 nm) SiO_2/Si commercially available substrate and (7.5 nm) Al_2O_3/Si substrate with iron (Fe) as the catalyst.

All the characterizations that are discussed in this chapter are ex-situ characterizations. The growths were done several times using the same parameters to verify the reproducibility of our findings, that was confirmed. Figure 3.1 gives the schematics of the path that has been chosen to develop the W/C HM.

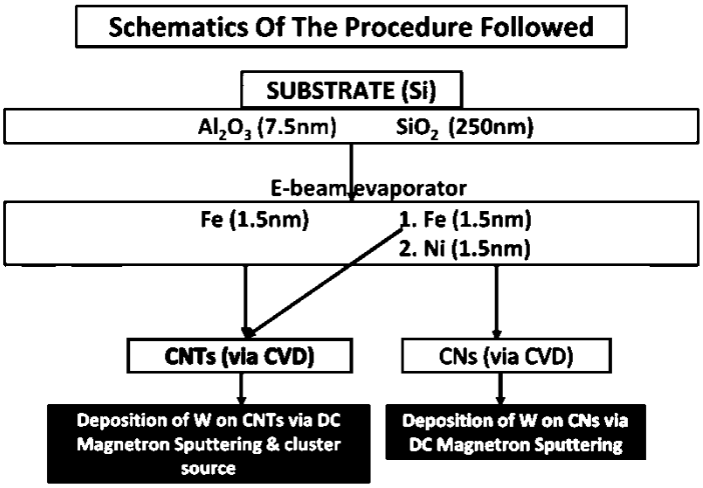

Figure3. 1 Experimental route for the synthesis of CNs, three wafers were used: two with SiO_2 (250nm)/Si and one with Al_2O_3 (7.5 nm)/Si. Ni (1.5 nm) was deposited on SiO_2 (250 nm)/Si (111) substrate whereas Fe (1.5 nm) was deposited on both SiO_2 (250nm)/Si and Al_2O_3 (7.5 nm)/Si via e-beam. These prepared substrates were then used for the growth of CNs via CVD. After the synthesis of CNs/CNTs, W was deposited on top of them by two different techniques, i.e., DCMS and SCS.

3.1 CVD on SiO_2(250 nm)/Si (111) using Ni as catalyst

Figure 3.2 shows the SEM image of the 1.5 nm Ni film deposited at room temperature via e-beam on the SiO_2 250 nm thick film (see chap. 2 for preparation details). Introduction of SiO_2 between Ni and Si was done to avoid the formation of silicide at higher temperature [1]. Furthermore, it has been brought into consideration that Ni films grown on SiO_2 have an intrinsic stress, which increases with film thickness. Ni films on SiO_2 are kinetically confined after growth at low temperatures and when annealed above 200 ºC they agglomerate. It is reported that when films having thickness less than 5 nm, wetting layer of Ni between agglomerated Ni and SiO_2 formed that act as a diffusion barrier. Hence at a higher temperature the Ni particle will form bigger particles instead of diffusing into the oxide layer [1,2].

There are three primary modes of thin film growth. These are Volmer-Weber (when the film grows in the form of islands), Frank- van der Merwe (layer by layer growth of film) and Stranski- Krastanov (mixture of both islands + layer by layer). The image shows that the growth followed the Volmer-Weber nucleation mode, with the formation of islands, which agrees with the literature. It has been reported that metals on insulators are more favoured to grow following the Volmer-Weber mechanism [3–6]. The reasons behind this fact are thermodynamics and kinetic in nature. The most important factors are the adhesion of metal film on insulator along with high vapour phase saturation and adsorption layer covering the surface facilitating Volmer-Weber growth [3].

The average islands size, calculated using ImageJ software, is (3.04 ± 0.5) nm.

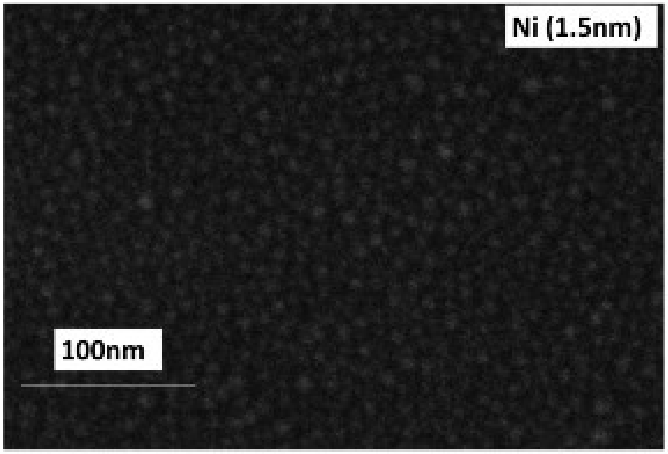

Figure3. 2 SEM image of Ni (1.5 nm) deposited thin film forming small island (Volmer-Weber)

We recall that the active chemical state of the catalyst is the metallic one. The structure of the grown CNs depends on the morphology that the catalyst film assumes after the pre-treatment and during CVD (refer to chapter 2). It is well known that annealing metal oxides (MO) in vacuum reduces their oxidation state [7], so one efficient CVD pre-treatment to activate the catalyst for CCVD is annealing in UHV environment.

Figure 3.3 (left, right) shows, respectively, the Ni 2p and O 1s XPS spectra of the as deposited Ni film after air exposure (bottom) and after in-situ annealing at 400 °C for 5 minutes (top). To analyse the chemical state of the film before and after annealing, we fitted the XPS spectra using several Voigt (GL convolution) profiles superimposed to a Shirley background. Nickel (Ni) has high reactivity towards oxygen. Ni films when exposed to air react with oxygen from the atmosphere, the presence of Ni^{3+} oxidation state in the as grown sample is clear in the Ni 2p XPS spectrum (figure 3.3 (left), bottom). From the spectrum shown in figure 3.3 peaks at 852.9 eV, 854.6 eV and 856.2 eV corresponding to Ni^0, Ni^{3+} and $Ni(OH)_2$ respectively [8–10]. Fitting parameters used are given in table A1.1 in appendix. Once annealed in vacuum at 400 ºC, it is completely reduced to Ni $2p_{3/2}$ which showed a peak at 852.9 eV and a satellite at 859.1 eV, in agreement with the values in literature [8,9].

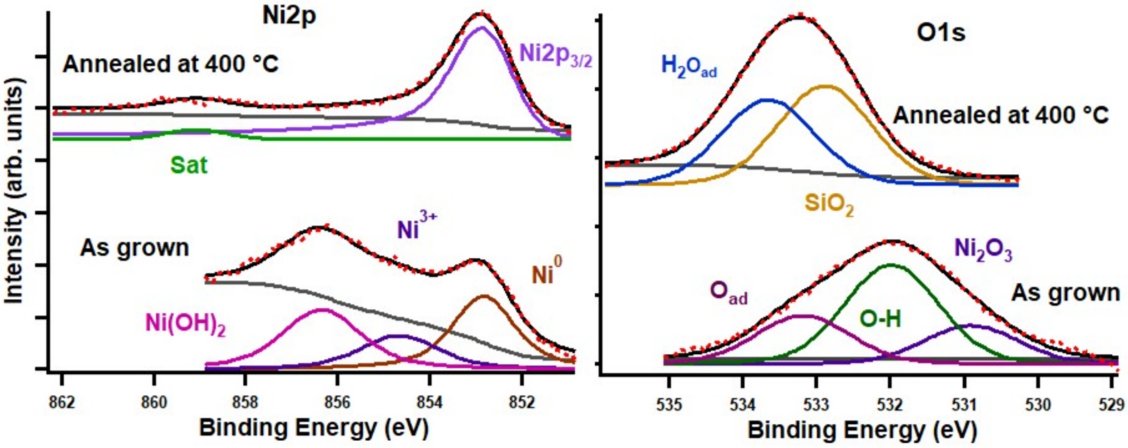

Figure3. 3 XPS spectra of as grown (purple) and annealed (red) at 400 °C a. Ni 2p3/2 and b. O 1s

Moreover, from the oxygen spectrum after exposure to air, Ni_2O_3 was present (figure 3.3 (right), bottom, table A 1.2). Absence of SiO_2 in the as grown spectrum showed the uniform coverage of Ni film on the substrate, but once annealed, due to agglomeration, SiO_2 layer was exposed and can be observed with another component (figure 3.3 (right), top).

In figure 3.3 (right) the spectrum of O (1s) electrons with dominant feature for the as grown sample was at 531.9 eV, corresponding to O-H. The other two spectral components of O (1s) spectra centred at 530.9 eV and 533.2 eV, referred to Ni_2O_3 and adsorbed H_2O respectively.

After annealing SiO_2 along with adsorbed H_2O, peaks at 532.9 eV and 533.6 eV were observed, respectively [5,10,11], to further confirm the reduction of the Ni film.

From the XPS data we concluded that the annealing treatment at 400 °C in UHV for 5 minutes was sufficient to completely reduce the Ni film, making it active and ready for CCVD. It was noted that 400 °C temperature was enough to crack the precursor gas, C_2H_2, when Ni is used as catalyst (see chapter. 1.2).

After the Ni film deposition, the substrate was cut in many parts. Each of them went through different **CCVD** processes, using the parameters described in chapter 2.3 (only the temperature was varied). Fig. 3.4. shows the SEM images of the nanostructures obtained at the different growth temperatures.

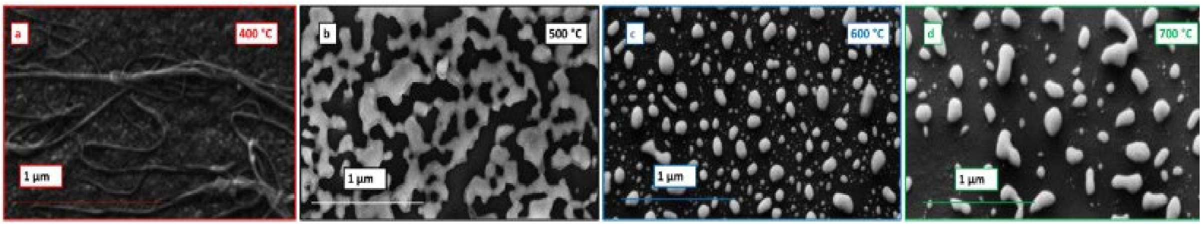

Figure3. 4 SEM images of the samples grown at four different growth temperature with a 45 tilt

The images were taken with a 45° tilt. From the SEM image 3.4 (a) we can clearly see that at 400 °C there were a few CNTs bundles distributed along the substrate. The low number of tubes observed may be because the time of growth was not long enough for the activation of all the Ni catalyst nanoparticles, or because the catalyst film thickness was too thick. We also noted that the presence of isolated SWCNTs flat on the substrate cannot be excluded because they are not visible by SEM. By increasing the CCVD temperature the catalyst started to agglomerate, and nanostructures of different shapes were attained. At 500 °C a "dendritic-like film" was formed, while at 600 °C and 700 °C multiple big nanoparticles, like peapods, were seen, whose size increased with increasing temperature. P.H. Lee et al. reported (shown in figure 3.5) almost the same structures, even if they were obtained using different thickness of the Ni films on 9.5 nm SiO_2/Si substrate (different from the one used in this work, i.e., 1.5 nm), varying from 1 nm to 20 nm [12]. They used the resistive heating method to deposit Ni of varying thickness on SiO_2. Afterwards, samples were thermally treated in the tube furnace in high vacuum conditions (~ 10^{-6} mbar). Samples were annealed for 30 mins at temperature ranging from 550 – 850 ºC. In the figure 3.5 the structures shown were annealed at 700 °C with varying thickness of Ni film.

In the present work, the thickness of the Ni film was the same for all samples (1.5 nm), and the formation of the different CNs depended only on the different CCVD temperature of growth.

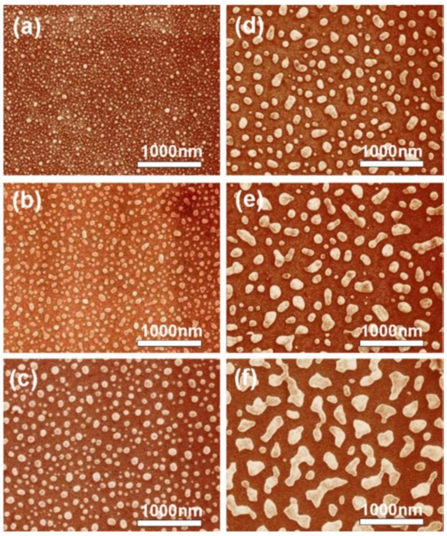

Figure3. 5 SEM images of thermally treated samples at 700 ºC of Ni on 9.5 nm SiO2. The thickness of Ni is respectively, (a) 1-, (b) 3-, (c) 7-, (d) 10-, (e) 15-, and (f) 20-nm [12].

The diameter's dimension analysis, based on SEM images using ImageJ software, showed that the mean value of the diameter's Gaussian distributions increased with increasing growth temperature. The mean diameter of CNs at 600 ºC was (66 ± 1.99) nm, and (100 ± 1.09) nm at 700 °C, as shown in figure 3.6.

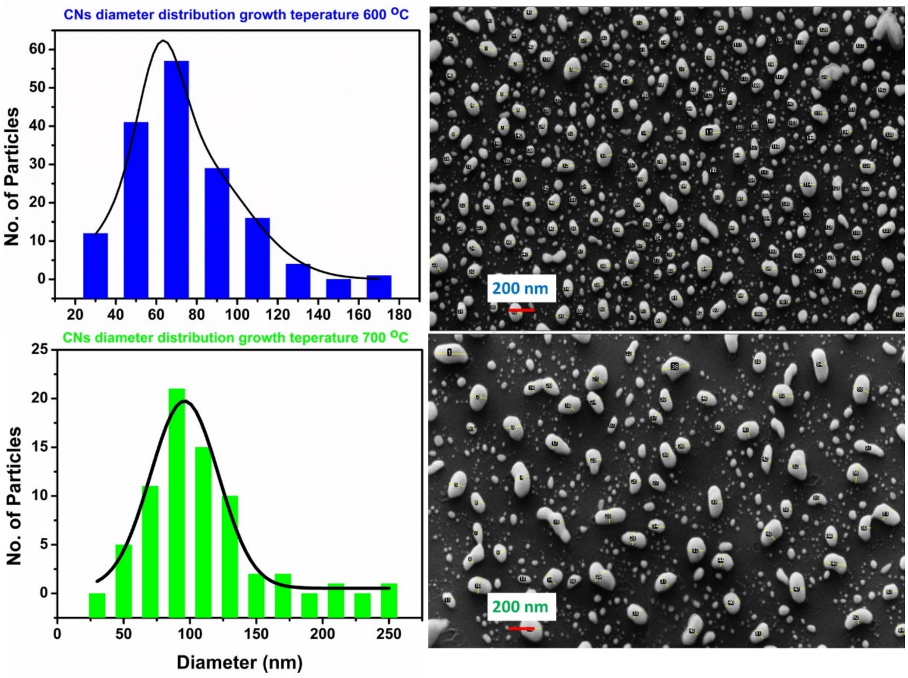

Figure3. 6 (Top) diameter distribution of CNs grown at 600 °C, (bottom) diameter distribution of CNs grown at 700 °C

From SEM image shown in figure 3.6 we calculated the number of C pebbles covering the Ni catalyst per µm^2 for the samples grown at 600 °C and 700 °C. Pebbles counted on 600 °C sample were (43 ± 0.8)/µm^2 and (13.2 ± 1.3)/µm^2 at 700 °C.

To further characterize the morphology of the nanostructures, we performed AFM as shown in figure 3.7. AFM analysis was performed by using Gwyddion software.

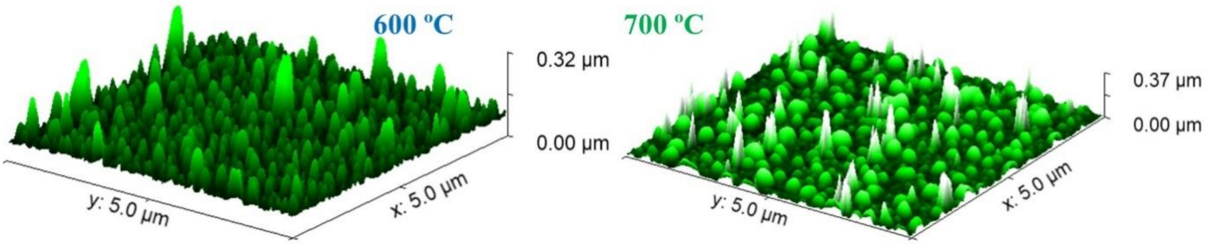

Figure3. 7 AFM images of CNs obtained at different growth temperatures

AFM imaging was used to study the surface topography of the CNs. The measurements were performed in contact mode, at RT, in air. Figure 3.8 shows the AFM two-dimensional (2D) images and for each of them a significant line profile of the CNs grown at 500 ºC, 600 ºC and 700 ºC is shown. The obtained values of the average roughness (Ra) are shown in figure 3.9. The surface roughness of CNs shown in Figure 3.9 revealed that for all the samples it is approximately the same (small change within the error limit). Thus, from the measurements we showed that the surface roughness of the CNs decreased slightly with the increasing growth temperature

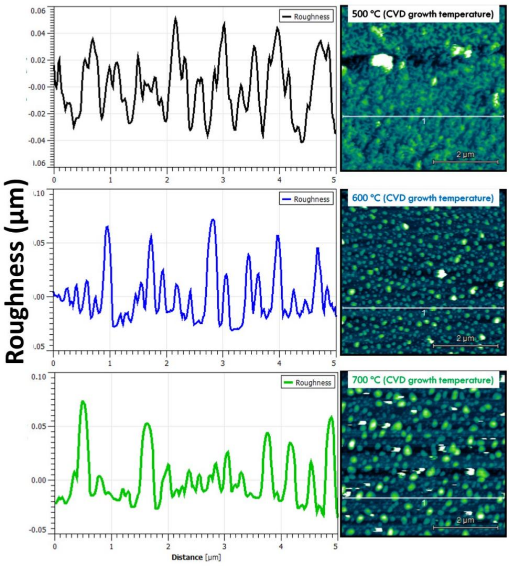

Figure3. 8 (left) Roughness profile of the samples grown at 500 °C, 600 °C and 700 °C from top to bottom, (right) AFM morphological 2D images in the same order

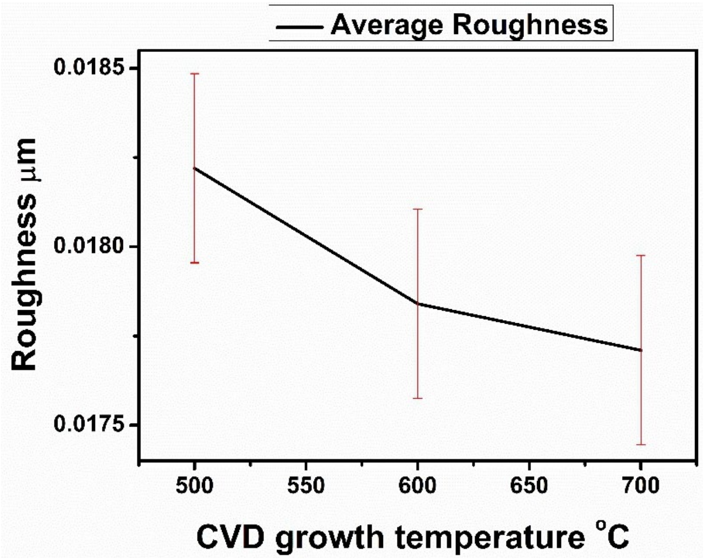

Figure3. 9 Average roughness Vs Temperature of growth

To reveal the chemistry and bonding state of the synthesized carbon nanostructures, we performed *ex-situ* XPS, as shown in figure 3.10 and table A1.3, after exposing the sample to air for many days. XPS have been performed at RT in normal emission geometry, fixing the binding energy (BE) scale to the Fermi level (no shift due to charging effects were observed). We first noted that in all samples the Ni 2*p* line shape has the typical line shape of Ni^0. This indicated that the CVD process implied the formation of a continuous coating on the catalyst, which prevented its oxidation even after air exposure. The Ni $2p_{3/2}$ of the samples grown at 400 °C and 500 °C is at ca. 852.7 eV, while at a higher temperature it was at about 853 eV. This may be an indication that as soon as the peapods started to agglomerate the chemical environment changed, implying a different chemical bonding between the substrate, catalyst, and CVD's reaction products. This was also reflected in the BE change of C 1s (figure 3.10 (left) and table A1.4), passing from about 284.0 eV at 400 °C, 500 °C and 700 °C to 284.6 eV at 600 °C. We noted that these binding energies are the typical BE compatible with the formation of sp^2 C, pointing towards the formation of a continuous C coating covering the catalyst. In addition to the main peak, after deconvolution, other components were present at (284.9 ± 0.3) eV referring to adventitious-C, (285.7 ± 0.3) eV corresponding to C-OH, and at 287.1 eV, corresponding to C-O-C, all may be due to the presence of contaminants after air exposure and/or to defects in the graphitic network synthesized by CCVD [13].

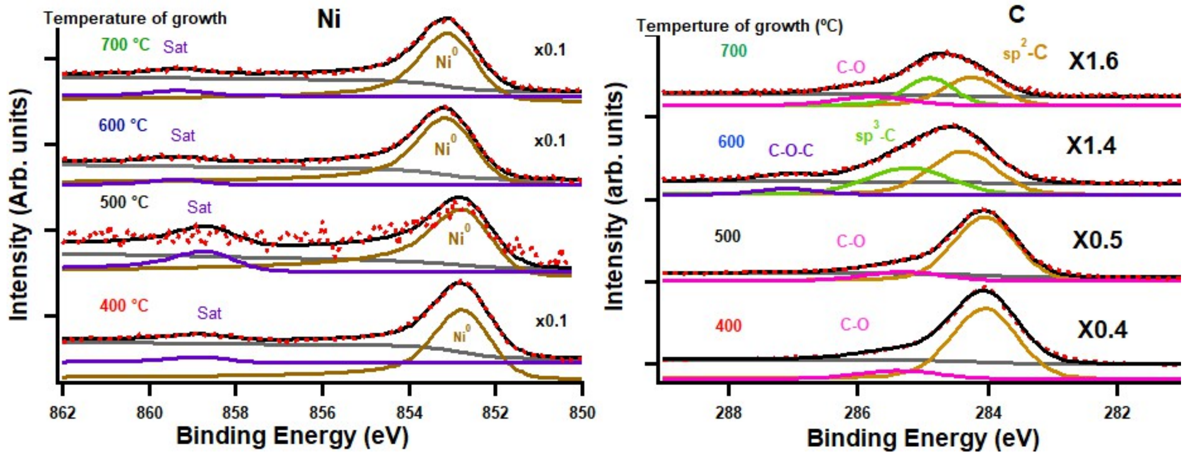

Figure3. 10 XPS core level spectra for (left) Ni 2p and (right) C 1s for CNs grown at different time of growth

To confirm these findings and to better identify the products of the synthesis, we performed Raman spectroscopy, which provided precise information about the quality and structure of the CNs [14]. RT Raman spectra were taken on all the grown samples using a laser excitation λ of 532 nm (see chapter 2.2). The two main peaks observed at high frequency zone are called D and G bands/ lines. G band corresponds to the E_{2g} mode, i.e., the stretching of C-C bond in the graphitic plane and are related to the presence of crystalline graphitic carbon. D band corresponds to the defects present in the CNs grown. G` band is used to determine the order or disorder in structure stacking. The ratio $I_{G'}/I_G$ is related to the defects in the stacking of the graphene structures [15]. The ratio of I_D/I_G is related the crystallinity of the CNs: the smaller the value of the ratio, the less defective are the CNs. Table 3.1 gives the information extracted from the spectra obtained for the CNs.

Figure 3.11 shows the Raman spectra obtained for the grown samples. All the spectra showed the position of the G band near 1575 cm^{-1}, corresponding to the G band related to the vibration of sp^2 bonded carbon atoms in a bi-dimensional hexagonal lattice, while the D band was near 1350 cm^{-1}, indicating defective graphitic structures. We noted that the G line shape at 400 °C is the typical line shape relative to SWCNT [16], indicating that the CNTs observed in SEM are SWCNTs organized in bundles with most possible some isolated SWCNTs not visible in SEM and AFM. From the I_D/I_G ratio the CNs synthesized at 400 °C were the most crystalline ones, further confirming the presence of few CNTs/SWCNTs on the surface [17,18]. The $I_{G`}/I_G$ ratio showed that the defects increased with the increase in the growth temperature.

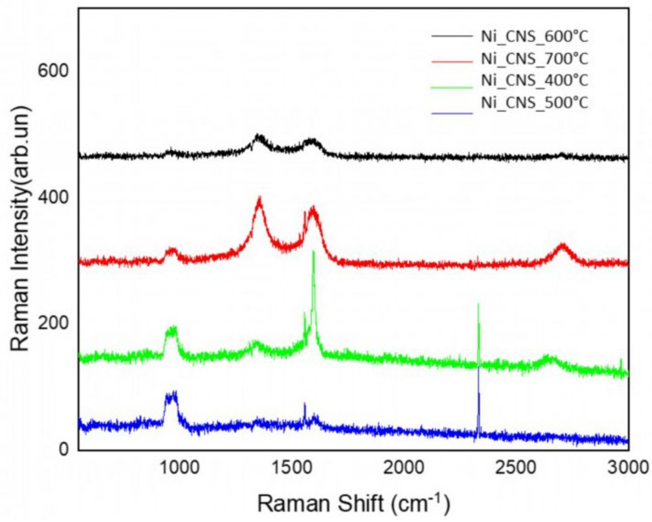

Figure3. 11 Raman Spectra of the CNs grown at different temperatures

Temperature of growth (°C)	Position of D band (cm)$^{-1}$	Position of G band (cm)$^{-1}$	Position of G′ band	Intensity of D band	Intensity of G band	Intensity of G` band	I_D/I_G	$I_{G`}/I_G$
400	1341	1595.6	2642	15.28	140.44	17.057	0.108	0.121
500	-	1570	-	-	11.12	-	-	-
600	1356	1581	2705	27	24	5	1.125	0.208
700	1355	1590	2703	93	86	30	1.08	0.348

Table 3.1: Observed values in Raman spectra and calculated I_D/I_G ratio

Moreover, at temperature higher than 400 °C the G mode line shape did not fit anymore for the presence of SWCNTs, but with that of CNFs and/or graphitic carbon. Also, the broadening of the G and the D bands indicated disordered graphitic planes covering the catalyst nanoparticles [19].

Considering the SEM, AFM, XPS and Raman data, we asserted that at 400 °C, a few numbers of horizontal CNTs/SWCNTs grew. On further increasing the temperature to 500 °C, because of the low interaction between the catalyst and SiO_2 and the high Ni mobility on this surface [6], the catalyst film started de-wetting, allowing the forming of dendritic-like nanostructures that were covered by a continuous sp^2 C coating through CCVD. By increasing the CVD growth temperature, the catalyst further agglomerated, forming big nanoparticles which were the seeds for CNs synthesis [6]. In all the sample, the catalyst was covered by a continuous carbon sp^2 coating, which prevented catalyst oxidation even after long (days) air exposure.

3.2 Synthesis of CNs on SiO_2 and Al_2O_3 thin films using Fe as catalyst

3.2.1 Characterization of Fe 1.5 nm film on SiO_2/Si

Ex situ measurements were done to study the chemical composition of the surface of the substrate coated with 1.5 nm of Fe catalyst (sample preparation explained in chapter 2) and its evolution after thermal annealing up to 600 °C in UHV environment. We took the XPS spectra for the as grown (air exposed) sample as well as for after annealing in UHV up to 600 °C for 5 minutes. Spectra shown are for both the as grown and annealed at 600 °C for both Fe2p and O1s.

From the as grown XPS spectrum (figure 3.12 bottom), it was observed that different oxidation states of iron were present, Fe^{2+} and Fe^{3+}. Unlike Ni, Fe requires a very high temperature in vacuum to reduce completely, approximately 1250 °C [20]. Therefore, even after annealing at 600 °C in vacuum, iron oxide was observed along with metallic Fe (figure 3.12 top, table A1.5).

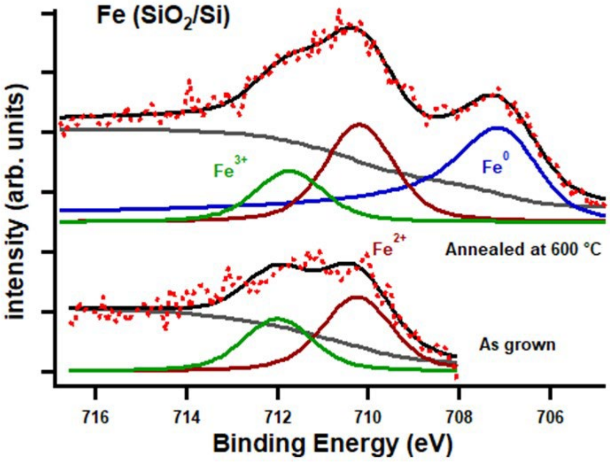

Figure3. 12 XPS spectra of a. Fe2p for as grown (air exposed) film (bottom) annealed in ultra-high vacuum at 600 °C (top)

XPS spectra was fit by using a Shirley background and by reproducing the photoemission peaks by using Doniach-Sunjic line shape, centred at the BE matching Fe^0, Fe^{2+}, and Fe^{3+} states of iron. For the oxidation states and satellite peaks the asymmetry parameter was kept zero, whereas for Fe^0 the asymmetry was set in the range of 0.42-0.46. The Lorentzian linewidth was fixed to 0.67 eV for all the Fe peaks [21].

Figure 3.12 shows that the air exposed film showed two components that correspond to two different oxidation states of Fe. The $Fe2p_{3/2}$ peaks at 710.5 eV, 711.9eV, referred to Fe^{2+} and Fe^{3+} respectively [22].

The sample was then annealed from 400 °C to 600 °C in step of 100 °C. At 600 °C we got a pronounced peak of Fe^0 at 707.2 eV [23]. It should be noted that 600 °C is the cracking temperature of acetylene (chapter 1). Other components that were present in the spectrum were at 709.93 eV and 711.3 eV, referring to Fe^{2+} and Fe^{3+} respectively [24,25].

Therefore, from the XPS we observed that when Fe thin film was annealed up to 600 °C, Fe^0 state was well pronounced as compared to lower temperatures. As already mentioned, it is well known that the metallic is the active catalyst state for the growth of CNTs. Therefore, for the consistency of the experiments we synthesized the CNTs selecting the same range as we have done for Ni catalyst. With Fe catalyst and C_2H_2 as precursor, growth of CNTs below 580 °C was less liable, as the cracking temperature of the precursor is 580 °C – 600 °C.

Hence, for the growth of CNTs, the temperature range of 600 °C – 700 °C was used, as already discussed in chapter 2.

3.2.2 Characterization of Fe (1.5 nm) catalyst film on Al_2O_3/Si

The wafer after depositing Fe on Al_2O_3/Si as explained in chapter 2, was characterized using XPS measurements. The substrate was exposed to air before XPS measurements. The same conditions for measuring spectra were used as described earlier for previous samples.

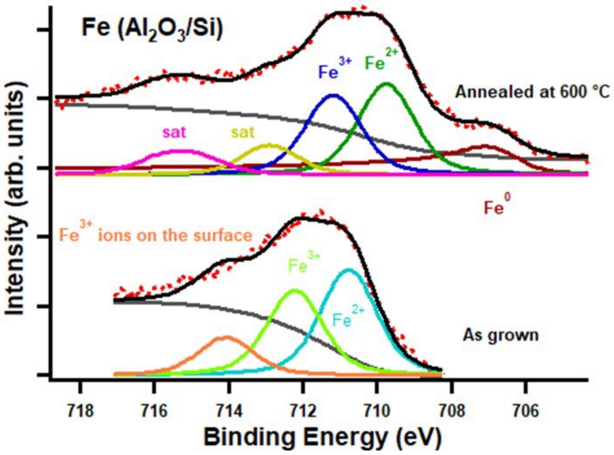

Figure3. 13 XPS spectra of Fe2p shown. These spectra are taken after the sample is being exposed to air and then in-situ annealing was done at 600 °C

In figure 3.13 and table A1.6, Fe2p core level spectra are shown for as grown and then UHV annealed at 600 ºC sample. After air exposure, the Fe $2p_{3/2}$ of the as grown sample showed three components at ca, 710.4 eV, 711.5 eV and 713.2 eV corresponding to Fe^{2+}, Fe^{3+} and Fe^{3+} surface ions respectively. After annealing in UHV conditions, we observed the presence of Fe^0 state at 706.8 eV and its satellite at 712.88 eV. Apart from metallic Fe, peaks at 709.7 eV, 711.2 eV and 714.7 eV referred to Fe^{2+}, Fe^{3+} and their satellite peak are seen [24,26].

In conclusion, on (7.5 nm)Al_2O_3/Si substrate, 1.5 nm of Fe was deposited via e-beam. Fe^{3+} and Fe^{2+} states were observed in XPS spectra for the air exposed as well as in vacuum annealed. At 600 °C, an additional peak appeared witnessing the presence of Fe^0, which can catalyse the growth of CNTs [27].

3.2.3 CVD of CNTs on SiO_2 (250 nm)/Si(100) using Fe (1.5 nm) as catalyst

The detailed description of all the used CVD parameters is described in detail in Chap. 2.1 As expected, no growth has been observed up to 600 ºC. At higher temperature of growth, i.e., 600 °C and 700 °C CNTs forest were observed, whose SEM images shown in figure 3.14 (tilt: 45º).

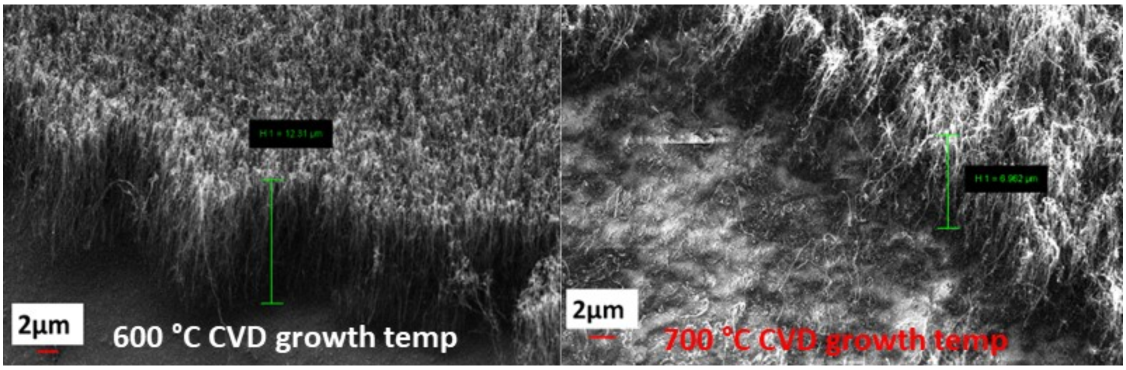

Figure3. 14 SEM images of the CNTs forest grown at (left) 600 °C and (right) 700 °C

From figure 3.14, the length of the CNTs were measured using ImageJ software. It was found that the average length of CNTs grown at 600 °C was (11.4 ± 0.5) µm and (5.3 ± 0.25) µm long at 700 °C. From image 3.15 we found the diameter of the CNTs. Average diameter of the CNTs grown at 600 °C and at 700 °C are (13.3 ± 4.5) nm and (20.5 ± 7.75) nm respectively. Moreover, using the same image, area density of the forest was calculated. We counted the roots of the CNTs on substrate. It was approximated that for the sample grown at 600 °C, (436 ± 4) CNTs/µm^2 were present, whereas for CNTs grown at 700 °C this number decreased to (28 ± 3) CNTs/ µm^2.

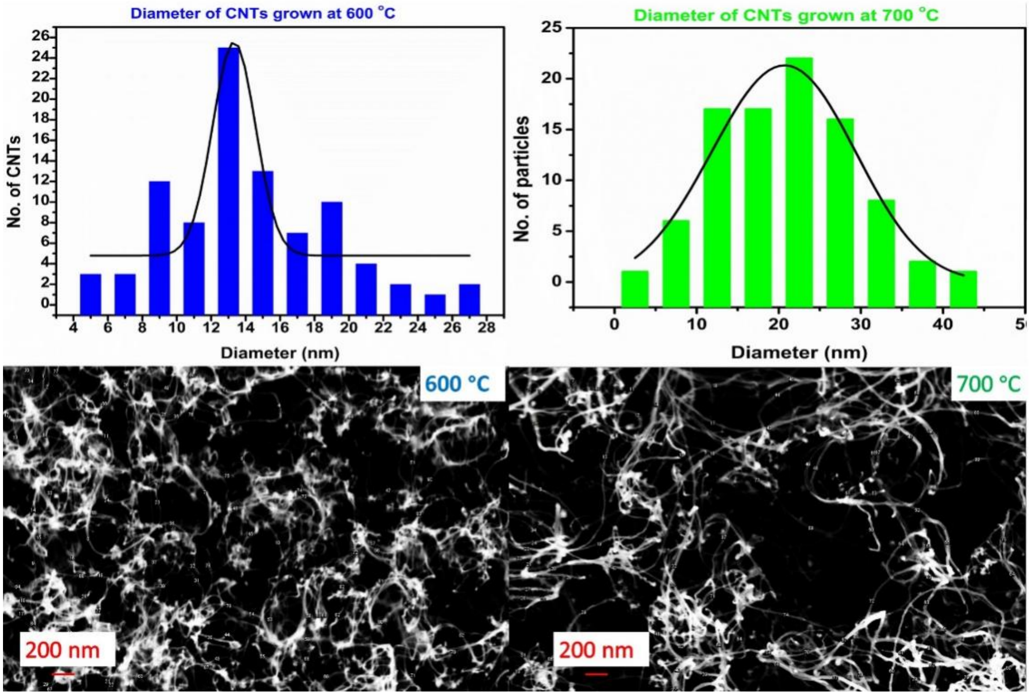

Figure3. 15 Diameter distribution on sample grown at (left) 600 °C and (right) 700 °C

CVD growth temperature °C	600	700
Mean Length of CNTs (µm)	11.4 ± 0.5	5.30 ± 0.25
Mean Diameter of CNTs (nm)	13.3 ± 4.5	20.5 ± 7.75
Approximate density of the forest	436 ± 4 CNTs/µm^2	28 ± 3 CNTs/µm^2

Table 3.2: Length and diameter of the CNTs grown at different growth temperatures

Ex-situ XPS measurements were done for the samples shown in SEM images. From XPS, shown in figure 3.16 and table A1.7, Fe^0 was observed at 706.6 eV in both the samples, whereas Fe^{2+} and Fe^{+3} states were approximately at peak position 710 eV and 711.9 eV with a slight shift towards lower BE at higher temperature [24].

From C1s (figure 3.16 (right) and table A1.8), BE at ca. 284.2 eV referred to the C=C bond [28]. C1s spectra were showing other peaks at 285.2 eV and 286 eV, referring to sp^3 C and C=O, respectively [29].

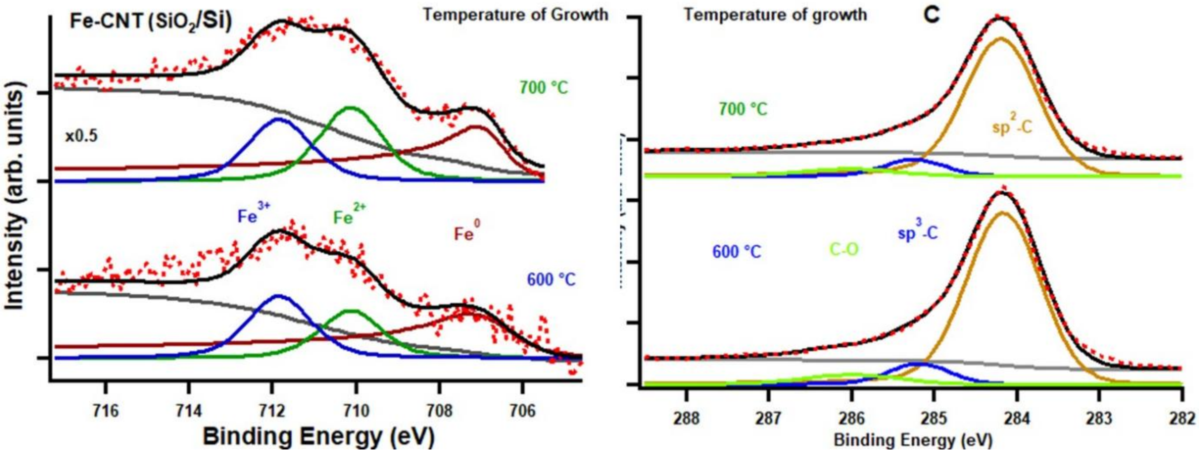

Figure3. 16 XPS spectra of Fe and C1s after different CVD growth temperature; 400 °C (red), 500 °C (black), 600 °C (blue) and 700 °C (green)

RT Raman spectra were taken at a laser excitation λ of 532 nm (see chapter 2). Spectra for 600 °C and 700 °C showed the presence of D, G and G` bands as shown in figure 3.17, while at lower temperature Raman demonstrated that no graphitic carbon is present on the surface, as expected (not shown).

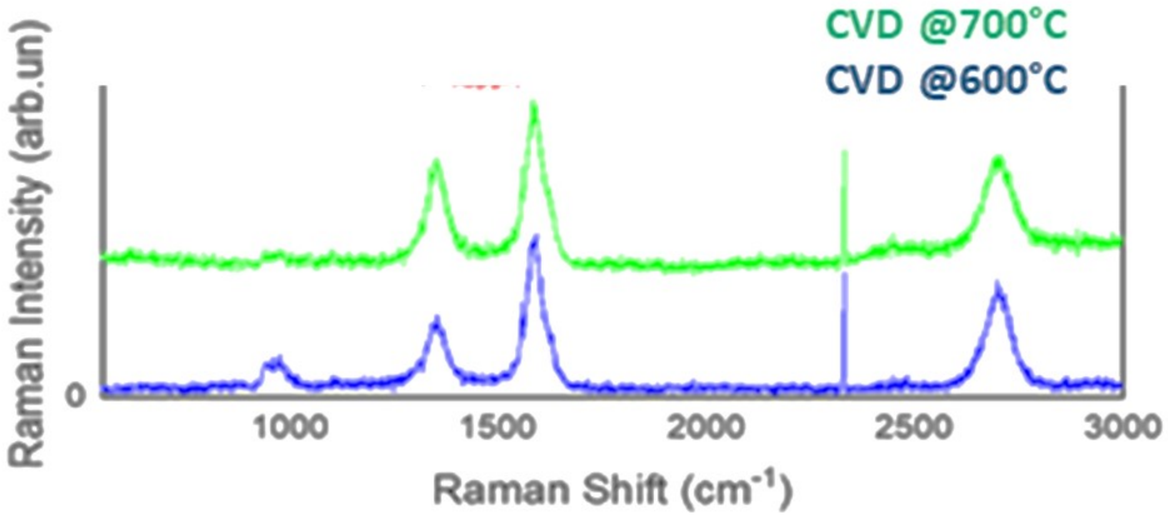

Figure3. 17 Raman spectra for CNTs grown at different CVD temperature

Temperature of growth (°C)	Position of D band $(cm)^{-1}$	Position of G band $(cm)^{-1}$	Position of G′ band	Intensity of D band	Intensity of G band	I_D/I_G
600	**1352**	**1588**	**2700**	**94**	**137**	**0.686**
700	**1351**	**1587**	**2700**	**70**	**143**	**0.487**

Table 3.3: Information extracted from Raman spectra for the CNTs grown at 600 °C and 700 °C

From the table 3.3, the position of D and G band gave the characteristic value for the MWCNTs. The ratio of peak intensities between D to G band indicated that the CNTs grown at 700 °C is more crystalline or less defective as compared to the ones grown at 600 °C. These defects are observed when the crystal symmetry is broken. Hence, we can find the degree of disorder in CNTs. It is also reported that increased temperature of growth will minimize the defects during CNTs synthesis [30].

3.2.4 CVD using Fe as catalyst on Al_2O_3/Si

The SEM image of the CNT forest grown at 600 °C CVD temperature on alumina with Fe as the catalyst is shown in figure 3.18 (tilt: 45°). From the SEM image using ImageJ software we calculated the diameter of the CNTs shown in the figure, as well as density of the forest. The diameter was (20.3 ± 1.3) nm and density was (932 ± 25) CNTs/μm^2.

Detailed description of all the used CVD parameters is given in section 2.3. We have already explained and observed that no growth has been observed below 600 °C on the samples where Fe has been deposited on SiO_2/Si substrate. Therefore, for Fe on alumina we synthesized CNTs by keeping the temperature constant at 600 °C and varying other parameters, which will be discussed later in this chapter.

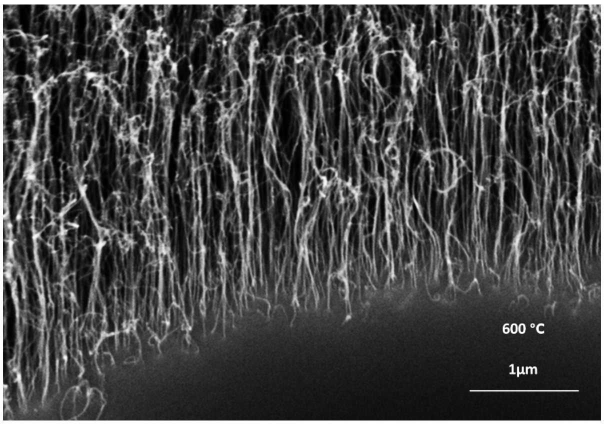

Figure3. 18 SEM image of CNT forest grown at 600 °C on Fe coated Al_2O_3/Si substrate where time of growth is 90 sec.

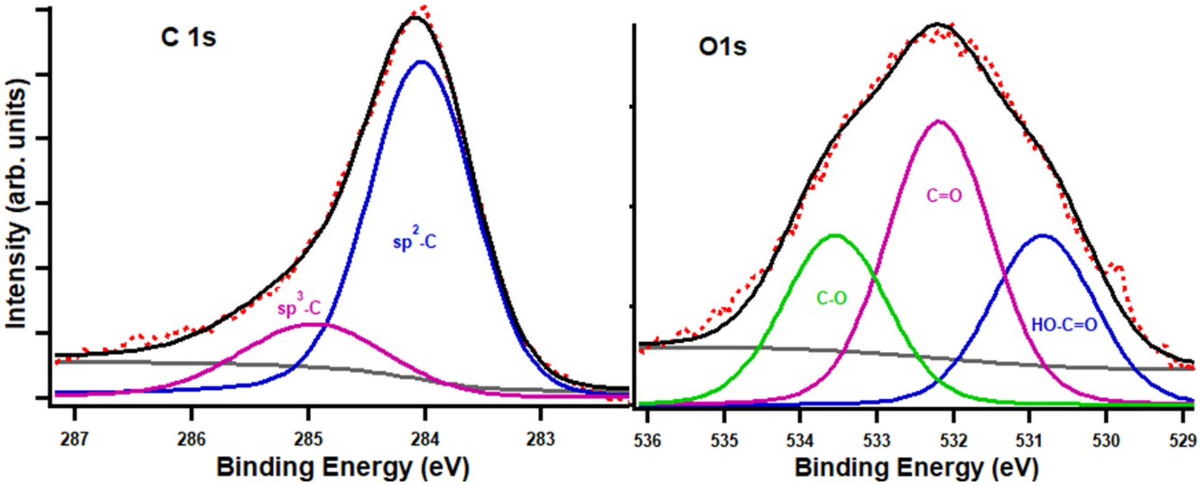

Figure3. 19 XPS core level spectra for (left) C1s and (right) for O1s of the CNT forest grown at 600 °C on Al_2O_3/Si substrate

After the growth of CNTs forest on the substrate under discussion, Fe was completely covered by the CNTs caused the Fe 2p signal to disappear. It was observed that the density of the CNTs on SiO_2/Si (436/μm^2) substrate was approximately half the value that we have obtained on Al_2O_3/Si (932/μm^2) substrate. This may explain flat Fe 2p spectrum.

But from C1s core level spectrum (figure 3.19, left, table A1.9) we saw that the peak at 284.1 eV is referred to sp^2 C, with sp^3 C at 285.15 eV, indicating the presence of some defects. From the O1s spectrum (figure 3.19, right, table A1.10), peaks at 530.8 eV, 532.2 eV, and 533.2 eV have been observed. These peaks corresponded to the presence of HO-C=O, C=O, and C-O, respectively [31,32].

3.3 Variation in CVD parameter for the growth of CNT forest

For the growth of VACNTs the typical standard procedure requires a metal catalyst on which a carbon feedstock is decomposed at a higher temperature. The catalyst layer is supported by an oxide under layer (most used are silica, magnesia, and alumina), that is to prevent alloying of metals at higher temperature (discussed in chapter 2). Up till now Fe in combination with alumina under layer has shown the best results for the growth of VACNTs. One of the positive aspects of alumina is that NPs of Fe oxide are confined and stabilized on alumina, hence restricting NP sintering [33].

Techniques used for the synthesis of long CNTs forest are well established. Hata et. al initially reported 2.5 mm long CNTs, synthesized using their famous super growth method. They used water as a stimulator of growth during the CCVD process [34]. Yaghoobi et.al, reported the synthesis of VACNTs for photoemission application. They reported mm long CNTs, grown by using 1 nm of Fe catalyst on 10 nm alumina on Si. Atmospheric pressure CVD deposition was adopted for the synthesis of CNTs. Pre-treatment was done at 750 ºC, in the presence of Ar (200 sccm) and H_2 (400 sccm). After 3 min of annealing, C_2H_4 (140 sccm) for the growth of VACNTs was introduced for an hour [35]. Another group presented a 14 cm long CNTs using cold gas CVD. They used 2 nm Fe/0.8 nm Gd/Al_2O_x substrate with C_2H_2 in combination with CO_2/Ar/H_2 for growth at 750 ºC, with a total gas flow rate to be equal to 500 sccm [36].

In another experiment, methane was used as a precursor on Fe/alumina substrate. They showed that diameter and length of the CNTs changes with the Fe content and reaction time. Thick catalytic layer may result in the formation of nanoribbons than CNTs [37]. Recently, VACNTs, were synthesized using almost similar parameters as we are reporting [38], to achieve 2.6 mm long CNTs but with a different setup.

To study the effect of time of growth, flow rate of precursor, and chamber pressure during growth we synthesized CNTs forest by varying them one by one and keeping the rest constant. Each one of them is discussed as follows:

3.3.1 Effect of time of growth on CNTs forest

To achieve an effective growth rate, it has been observed that fast growth and an active catalyst plays a major role. With time the growth rate can exponentially decrease. In some cases, termination of growth process is sudden. It is because of the sintering effect of the catalyst and its diffusion into the oxide layer [39]. Longer time of growth after certain point stops affecting the CNTs length, which may be due to de activation of the catalyst. It was reported earlier by a group that initially the CNTs grew linearly and rapidly with time. Then in the intermediate stage, the growth rate slowed down but after continuous exposure to gases the growth rate almost becomes negligible, indicating the point where the termination of growth will take place [40]. Li et. al, studied the growth kinematics to understand the behaviour of catalyst. They used 750 ºC as the growth temperature and showed the same trend as ref 40 [41].

As already discussed in the previous chapter, we studied **the effect of CCVD growth time by keeping all other process parameters constant**. We started varying the time from 15 s to 300 s and analysed the samples via SEM (figure 3.20) for the synthesis of CNTs forest. While we used SiO_2/Si substrate for a short growth duration, i.e., from 15 s to 120 s, the CNTs did not grow, whereas at 150 s growth time SEM images revealed the formation of CNTs. These CNTs were not vertically aligned, but for 300 s (5 min) time of growth, VACNTs were observed, as already shown in section 3.2.

Therefore, for SiO_2/Si substrate with 1.5 nm Fe catalyst, the CVD growth temperature to synthesize VACNTs with acetylene is 600 °C and above (upper limit was not tested). Below this we did not get VACNTs. Furthermore, for SiO_2/Si, a longer duration of precursor exposure was required, as shown in SEM image.

From the SEM images shown in figure 3.20 (bottom row), unlike SiO_2/Si substrate coated with Fe (top row), Al_2O_3/Si covered with Fe showed the growth of CNTs even for 15 s growth time. With the increase in the duration of time of growth, the length of the forest increased. Table 3.4 and figure 3.21 are showing the calculated values of length of CNTs synthesized on alumina substrate, using ImageJ software.

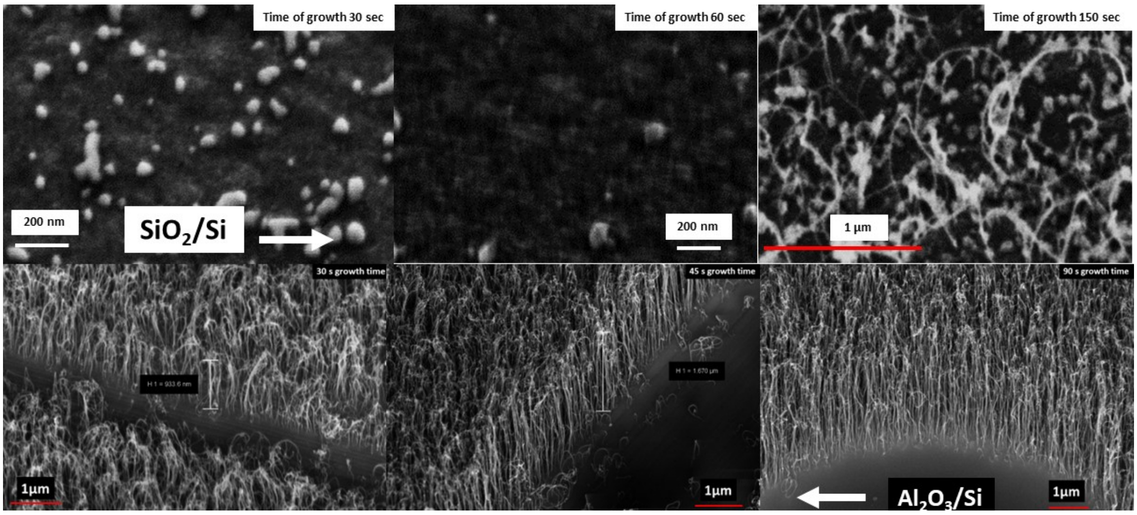

Figure3. 20 SEM images of the samples grown at 600 °C but with different growth time on (top) SiO_2/Si and (bottom) Al_2O_3/Si substrate with 1.5 nm Fe as catalyst.

Time of growth (sec)	Diameter of CNTs (nm)	Length of CNTs (nm)
15	13.5 ± 0.675	398 ± 19.9
30	13.09 ± 0.6545	834 ± 41.7
45	13.972 ± 0.6986	908 ± 45
60	11.501 ± 0.575	1096 ± 54.8
90	12.42 ± 0.621	1842 ± 92.1
1500	11.0289 ± 0.551	15427 ± 771.53

Table 3.4: Time of growth vs diameter and length of CNTs

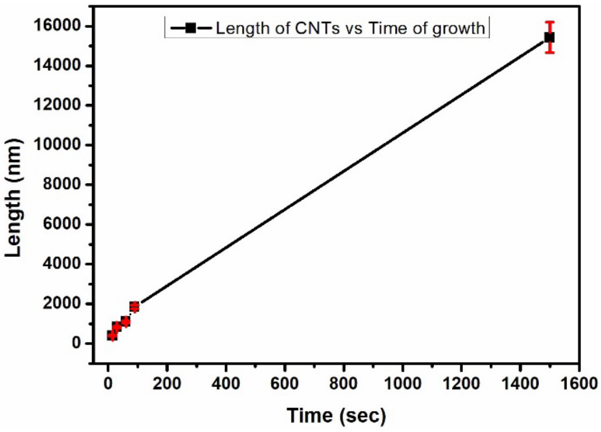

Figure3. 21 Graphical representation of change in length of CNTs with time of growth on Fe deposited Al_2O_3/Si substrate

Figure 3.22 is showing the SEM images for diameter evaluation of the same CNTs shown in figure 3.20. With the increase in time of growth the diameter of the CNTs is gradually decreasing. Figure 3.23 and table 3.4 show the variation in diameter as a function of time of growth.

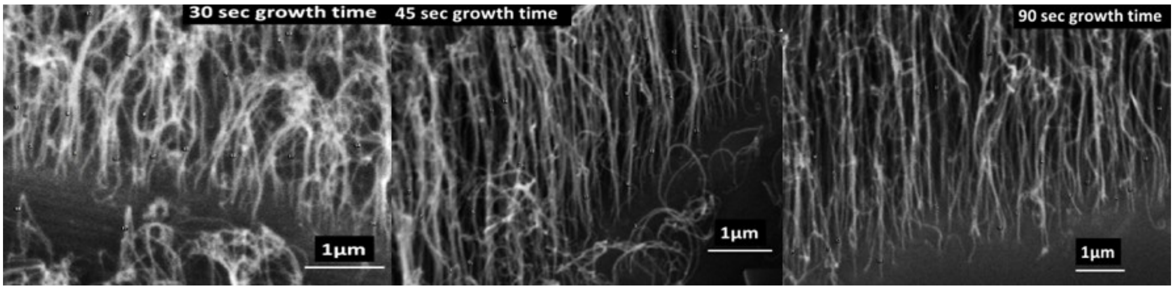

Figure3. 22 SEM Images of CNTs forest used to calculate the diameter of the CNTs using ImageJ software.

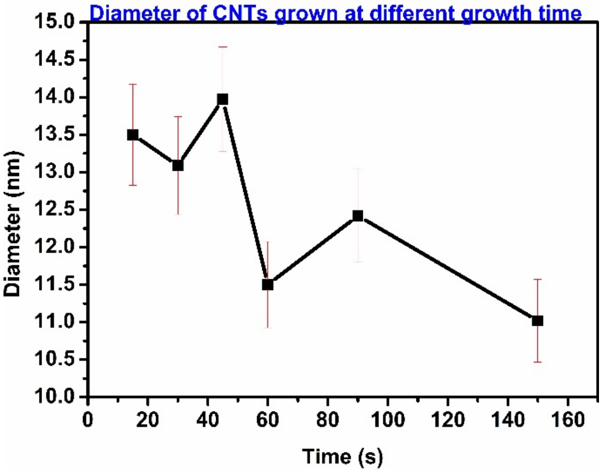

Figure3. 23 Changing diameter of CNTs with time of growth

In our work, with the increase in time of growth up to 25 min at 600 °C for 100 sccm of H_2 and C_2H_2, the growth rate increased. But after 25 min the change in growth rate was not exponential but slow, and finally after 180 min of growth time we did not find any change in the length.

3.3.2 Effect of C_2H_2 flow rate

Figure 3.24 shows the SEM images of CNTs grown on Al_2O_3/Si substrate with reduced flow of acetylene (80 sccm). Figure 3.25 shows the variation in diameter of CNTs as well as the length of CNTs as a function of time of growth respectively. Table 3.5 gives the values of the diameter and length of CNTs.

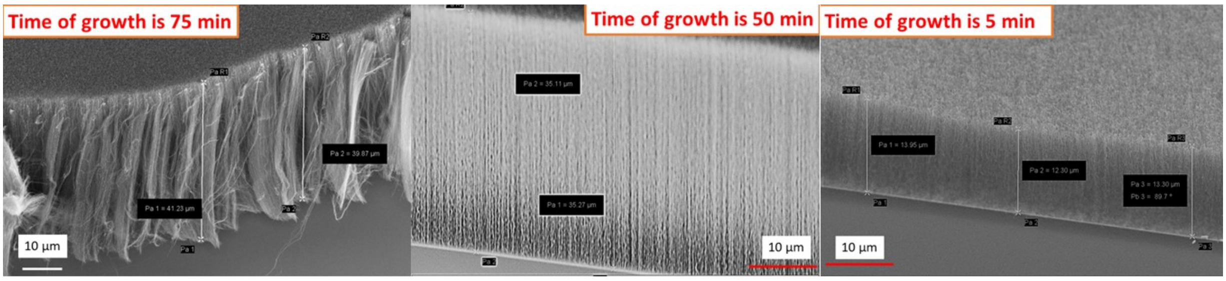

Figure3. 24 SEM images of the CNTs forest grown at reduced acetylene flow rate for different time of growth

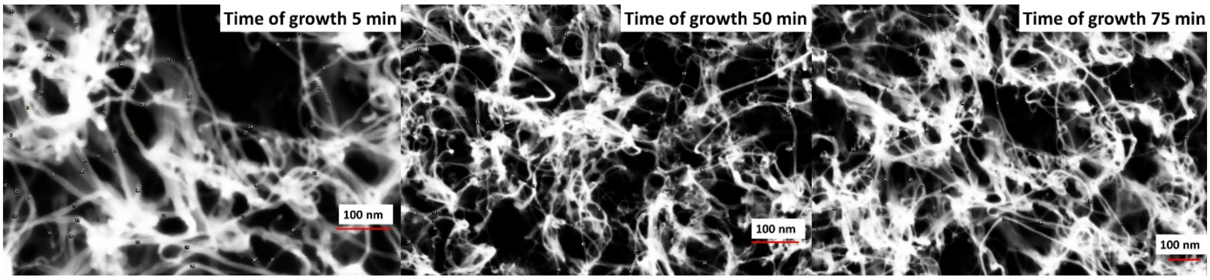

Figure3. 25 SEM images used for diameter calculation for 5 min 50 min and 75 min growth time for 80 sccm flow rate of C_2H_2

Time of growth (min)	Diameter (nm)	Length (µm)
5	7.35 ± 0.741	13.087 ± 0.654
50	7.042 ± 0.352	34.682 ± 1.734
75	6.524 ± 0.363	41.030 ± 2.051

Table 3.5: diameter and length of CNTs as a function of time of growth with 80 sccm acetylene flow rate

Haidari and co-worker showed that the diameter of the CNTs is affected by the low flow rate of precursor. If the flow rate of the carbon source is increased, it will increase the diameter of the CNTs. This is due to the deposition of the excessive amorphous carbon on the outer walls of the CNTs [42]. Moreover, other similar results were reported along with the fact that the increased flow rate introduced defects in CNTs, resulting in decreasing graphitic phase [43].

If we compare the results that we have from section 3.3.1 and 3.3.2, we can see that they agree with the literature and the diameter has reduced with the decrease in the flow rate of precursor gas.

3.3.3 Effect of CCVD growth pressures (pumping speed)

The following SEM images (figure 3.26) show different growth pressures. In the table 3.6, the length of the CNTs is given w.r.t their growth pressure:

Pressure of growth mbar	Length of CNTs (µm)
0.44	163
0.66	274
0.88	194.52
1.34	80
5.5	119.8
12.3	172

Table 3.6: Pressure during growth Vs length of CNTs

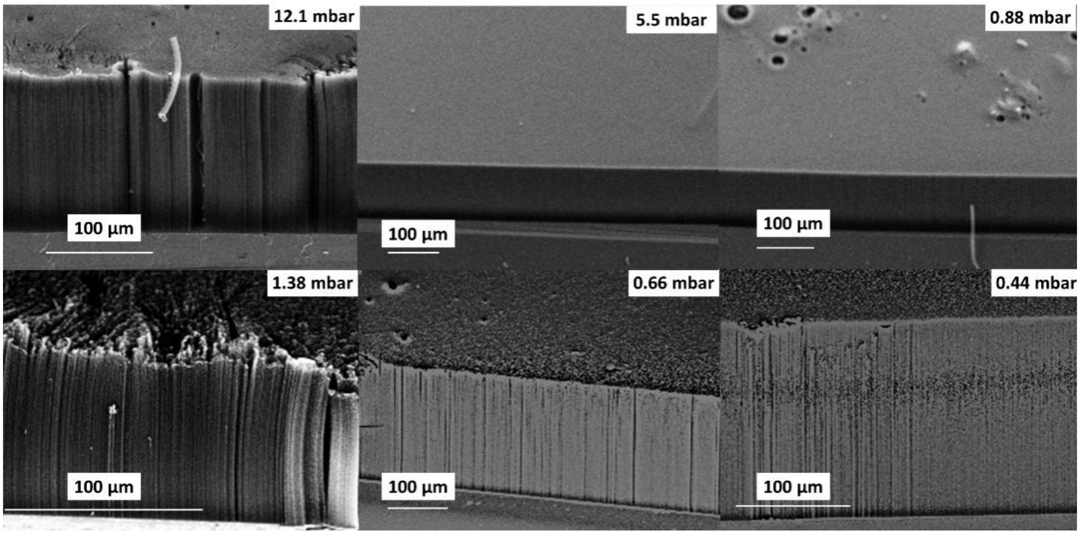

Figure3. 26 SEM images of CNT forest grown at different pressure during growth

Li et. al, showed that with the increase in pressure, the yield increased and at 200 torr there was a sudden 486 % increase in CNTs yield. Which then at certain higher pressure started to decrease [44].

In this section we showed that increasing the chamber pressure increased the length of CNTs up to 0.66 mbar and then afterwards a decreasing trend was observed.

With Al_2O_3/Si, it was observed that with Fe as the catalyst produced excellent results even for very short duration of exposure to the pre-cursor gas (acetylene in our case and at 600 °C growth temperature).

3.4 Summary

When we have synthesised CNs (dendritical and peapods), with 1.5 nm, Ni/SiO_2/Si deposited via e-beam, the aim was to get a CNT forest at low temperature. But as earlier reports suggested that thickness of the catalyst plays an important role, 1.5 nm Ni was too thick to assist in the growth of CNTs forest. We then varied the temperature of CCVD growth and found that with the increase of growth temperature the CNs starts sintering and form pebble like structures. Furthermore, we noted that at 400 °C, SEM image showed horizontally grown CNTs. Their growth may be attributed to the fact that during deposition of catalyst the outer edge of the wafer gets less material deposit, and as the cracking temperature for C_2H_2 with Ni is ~ 350 °C, therefore few of the CNTs grew. Moreover, Raman showed the typical peak structure for SWCNTs.

Other catalyst that we used was 1.5 nm of Fe on silica and alumina separately via e-beam. We initially grew CNTs on SiO_2/Si substrate coated with Fe and then to vary the length of the forest by varying CCVD parameter, we switched to Fe deposited Al_2O_3/Si.

Briefly, long, thin, and dense CNT forest can be synthesised in many ways as discussed earlier. What we are reporting is a simple method, in which CNTs are synthesised using a CCVD homemade chamber, with H_2 (100 sccm) as pre-treatment gas and C_2H_2 (80-100 sccm) as carbon source. We were able to show CNT forest on Fe/SiO_2 substrate for growth time ≥300 s, but for Fe/Al_2O_3, we showed variation of CNT forest length ranging from 500 nm - ~ 300 μm. Max. growth rate of CNTs that we have achieved was 2.8 μm/min on Fe/Al_2O_3. Therefore, without using Ar or other gases that help in increasing the lifetime of catalyst (CO_2, NH_3 etc), we successfully grew CNT forest of variable length.

3.5 Reference

[1] A.M. Thron, P.K. Greene, K. Liu, K. Van Benthem, Structural changes during the reaction of Ni thin films with (1 0 0) silicon substrates, Acta Mater 60 (2012) 2668–2678. https://doi.org/10.1016/j.actamat.2012.01.033.

[2] C. Boragno, F. Buatier De Mongeot, R. Felici, I.K. Robinson, Critical thickness for the agglomeration of thin metal films, Phys Rev B Condens Matter Mater Phys 79 (2009). https://doi.org/10.1103/PhysRevB.79.155443.

[3] M. Becht, F. Atamny, A. Baiker, K.-H. Dahmen, Morphology analysis of nickel thin films grown by MOCVD, Surf Sci 371 (1997) 399–408. https://doi.org/10.1016/S0039-6028(96)01015-1.

[4] H.Z. Yu, C. V. Thompson, Stress engineering using low oxygen background pressures during Volmer–Weber growth of polycrystalline nickel films, Journal of Vacuum Science & Technology A: Vacuum, Surfaces, and Films 33 (2015). https://doi.org/10.1116/1.4902957.

[5] J. Franc, Z. Bastl, Nickel evaporation in high vacuum and formation of nickel oxide nanoparticles on highly oriented pyrolytic graphite. X-ray photoelectron spectroscopy and atomic force microscopy study, Thin Solid Films 516 (2008) 6095–6103. https://doi.org/10.1016/j.tsf.2007.11.008.

[6] J.A. Sengupta Chacko Jacob, The effect of Fe and Ni catalysts on the growth of multiwalled carbon nanotubes using chemical vapor deposition, Journal of Nanoparticle Research 12 (2010) 457–465. https://doi.org/10.48550/arXiv.1908.00391.

[7] S.Y. Lee, N. Mettlach, N. Nguyen, Y.M. Sun, J.M. White, Copper oxide reduction through vacuum annealing, Appl Surf Sci 206 (2003) 102–109. https://doi.org/10.1016/S0169-4332(02)01239-4.

[8] R. Sanchis, T. García, A.M. Dejoz, I. Vázquez, F.J. Llopis, B. Solsona, Easy method for the transformation of levulinic acid into gamma-valerolactone using a nickel catalyst derived from nanocasted nickel oxide, Materials 12 (2019). https://doi.org/10.3390/ma12182918.

[9] C. Drouet, C. Laberty, J. Fierro, P. Alphonse, A. Rousset, A. Rousset X-, A. X-, P. Alphonse, A. Rousset, X-ray photoelectron spectroscopic study of non-stoichiometric nickel and nickel-copper spinel manganites Open Archive TOULOUSE Archive Ouverte (OATAO) X-ray photoelectron spectroscopic study of non-stoichiometric nickel and nickel-copper spinel manganites, International Journal of Inorganic Materials 2 (2000) 419–426. https://doi.org/10.1016/S1466-6049(00)00047-7ï.

[10] D.P. Xing, H. Zhong Zeng, W. Xu Zhang, W. Li Zhang, XPS studies of charging effect induced by X-ray irradiation on amorphous SiO2 thin films, in: IOP Conf Ser Mater Sci Eng, Institute of Physics Publishing, 2019. https://doi.org/10.1088/1757-899X/490/2/022079.

[11] A.P. Grosvenor, M.C. Biesinger, R.S.C. Smart, N.S. McIntyre, New interpretations of XPS spectra of nickel metal and oxides, Surf Sci 600 (2006) 1771–1779. https://doi.org/10.1016/j.susc.2006.01.041.

[12] P.H. Lee, C.C. Chang, Spectroscopic characterization of Ni films on sub-10-nm silica layers: Thermal metamorphosis and chemical bonding, Surf Sci 601 (2007) 362–375. https://doi.org/10.1016/j.susc.2006.10.030.

[13] M. Fingerle, S. Tengeler, W. Calvet, W. Jaegermann, T. Mayer, Sputtered Nickel Oxide Thin Films on n-Si(100)/SiO 2 Surfaces for Photo-Electrochemical Oxygen Evolution Reaction (OER): Impact of Deposition Temperature on OER Performance and on Composition before and after OER , J Electrochem Soc 167 (2020) 136514. https://doi.org/10.1149/1945-7111/abbcdf.

[14] D. Yoon, H. Moon, H. Cheong, J. Sik Choi, J. Ae Choi, B. Ho Park, Interference effect on Raman spectrum of graphene on SiO2/Si, Journal of the Korean Physical Society 55 (2009). https://doi.org/10.1103/PhysRevB.80.125422.

[15] I. Calizo, D. Teweldebrhan, W. Bao, F. Miao, C.N. Lau, A.A. Balandin, Spectroscopic Raman nanometrology of graphene and graphene multilayers on arbitrary substrates, J Phys Conf Ser 109 (2008). https://doi.org/10.1088/1742-6596/109/1/012008.

[16] G. Bertoni, C. Cepek, F. Romanato, C.S. Casari, A. Li Bassi, C.E. Bottani, M. Sancrotti, Growth of multi-wall and single-wall carbon nanotubes with in situ high vacuum catalyst deposition [6], Carbon N Y 42 (2004) 440–443. https://doi.org/10.1016/j.carbon.2003.11.005.

[17] Y. Yao, L.K.L. Falk, R.E. Morjan, O.A. Nerushev, E.E.B. Campbell, Synthesis of carbon nanotube ®lms by thermal CVD in the presence of supported catalyst particles. Part I: The silicon substrate/nanotube film interface, Journal of Material Science: Materials in Electronics 15 (2004) 533–543.

[18] M. Endo, Y.A. Kim, Y. Fukai, T. Hayashi, M. Terrones, H. Terrones, M.S. Dresselhaus, Comparison study of semi-crystalline and highly crystalline multiwalled carbon nanotubes, Appl Phys Lett 79 (2001) 1531–1533. https://doi.org/10.1063/1.1400774.

[19] D.Q. McNerny, B. Viswanath, D. Copic, F.R. Laye, C. Prohoda, A.C. Brieland-Shoultz, E.S. Polsen, N.T. Dee, V.S. Veerasamy, A.J. Hart, Direct fabrication of graphene on SiO 2 enabled by thin film stress engineering, Sci Rep 4 (2014). https://doi.org/10.1038/srep05049.

[20] F. Hofmann, J. Treffkorn, K.A. Farley, U-loss associated with laser-heating of hematite and goethite in vacuum during (U–Th)/He dating and prevention using high O2 partial pressure, Chem Geol 532 (2020). https://doi.org/10.1016/j.chemgeo.2019.119350.

[21] D.G. Van Campen, R.J. Pouliot, L.E. Klebanoff, Spin-resolved x-ray-photoelectron-spectroscopy study of ferromagnetic iron, Phys Rev B 48 (1993) 17533–17537. https://doi.org/10.1103/PhysRevB.48.17533.

[22] S.L. Tait, Y. Wang, G. Costantini, N. Lin, A. Baraldi, F. Esch, L. Petaccia, S. Lizzit, K. Kern, Metal-organic coordination interactions in Fe-terephthalic acid networks on Cu(100), J Am Chem Soc 130 (2008) 2108–2113. https://doi.org/10.1021/ja0778186.

[23] K. Rokosz, T. Hryniewicz, S. Raaen, Cr/Fe RATIO BY XPS SPECTRA OF MAGNETOELECTRO POLISHED AISI 316L SS FITTED BY GAUSSIAN-LORENTZIAN SHAPE LINES, Tehnicki Vjesnik 21 (2014) 533–538. http://hdl.handle.net/11250/2626909 (accessed January 21, 2024).

[24] T. Yamashita, P. Hayes, Analysis of XPS spectra of Fe 2+ and Fe 3+ ions in oxide materials, Appl Surf Sci 254 (2008) 2441–2449. https://doi.org/10.1016/j.apsusc.2007.09.063.

[25] M.S. Mohamed Saheed, N.M. Mohamed, Z.A. Burhanudin, Effect of different catalyst deposition technique on aligned multiwalled carbon nanotubes grown by thermal chemical vapor deposition, J Nanomater 2014 (2014). https://doi.org/10.1155/2014/707301.

[26] D. Guo, Y. An, W. Cui, Y. Zhi, X. Zhao, M. Lei, L. Li, P. Li, Z. Wu, W. Tang, Epitaxial growth and magnetic properties of ultraviolet transparent Ga2O3/(Ga1−xFex)2O3 multilayer thin films, Sci Rep 6 (2016). https://doi.org/10.1038/srep25166.

[27] N. Nagaraju, A. Fonseca, Z. Konya, J.B. Nagy, Alumina and silica supported metal catalysts for the production of carbon nanotubes, J Mol Catal A Chem 181 (2002) 57–62.

[28] Y.M. Shulga, S.A. Baskakov, E.I. Knerelman, G.I. Davidova, E.R. Badamshina, N.Y. Shulga, E.A. Skryleva, A.L. Agapov, D.N. Voylov, A.P. Sokolov, V.M. Martynenko, Carbon nanomaterial produced by microwave exfoliation of graphite oxide: New insights, RSC Adv 4 (2014) 587–592. https://doi.org/10.1039/c3ra43612h.

[29] X. Chen, X. Wang, D. Fang, A review on C1s XPS-spectra for some kinds of carbon materials, Fullerenes Nanotubes and Carbon Nanostructures (2020) 1048–1058. https://doi.org/10.1080/1536383X.2020.1794851.

[30] Y. Xiao, Z. Ahmed, Z. Ma, C. Zhou, L. Zhang, M. Chan, Low temperature synthesis of high-density carbon nanotubes on insulating substrate, Nanomaterials 9 (2019). https://doi.org/10.3390/nano9030473.

[31] K. Qu, Y. Zheng, Y. Jiao, X. Zhang, S. Dai, S.Z. Qiao, Polydopamine-Inspired, Dual Heteroatom-Doped Carbon Nanotubes for Highly Efficient Overall Water Splitting, Adv Energy Mater 7 (2017). https://doi.org/10.1002/aenm.201602068.

[32] E. Paparazzo, XPS analysis of iron aluminum oxide systems, Appl Surf Sci 25 (1986) 1–12. https://doi.org/10.1016/0169-4332(86)90021-8.

[33] A. Roussey, N. Venier, H. Fneich, L. Giardella, T. Pinaud, S. Tahir, M. Pelaez-Fernandez, R. Arenal, A. Mehdi, V. Jourdain, One-pot preparation of iron/alumina catalyst for the efficient growth of vertically-aligned carbon nanotube forests, Materials Science and Engineering: B 245 (2019) 37–46. https://doi.org/10.1016/j.mseb.2019.05.005.

[34] K. Hata, * Don, N. Futaba, K. Mizuno, T. Namai, M. Yumura, S. Iijima, Water-Assisted Highly Efficient Synthesis of Impurity-Free Single-Walled Carbon Nanotubes, Science (1979) 306 (2004) 1362–1364. https://doi.org/10.1126/science.1104962.

[35] P. Yaghoobi, M. Michan, A. Nojeh, Middle-ultraviolet laser photoelectron emission from vertically aligned millimeter-long multiwalled carbon nanotubes, Appl Phys Lett 97 (2010). https://doi.org/10.1063/1.3496486.

[36] H. Sugime, T. Sato, R. Nakagawa, T. Hayashi, Y. Inoue, S. Noda, Ultra-long carbon nanotube forest via in situ supplements of iron and aluminum vapor sources, Carbon N Y 172 (2021) 772–780. https://doi.org/10.1016/j.carbon.2020.10.066.

[37] P. Zarabadi-Poor, A. Badiei, A.A. Yousefi, B.D. Fahlman, A. Abbasi, Catalytic chemical vapour deposition of carbon nanotubes using Fe-doped alumina catalysts, Catal Today 150 (2010) 100–106. https://doi.org/10.1016/j.cattod.2009.06.019.

[38] O.T. Gul, A simple method to grow millimeters long vertically aligned carbon nanotube forests, Diam Relat Mater 120 (2021) 108637. https://doi.org/10.1016/j.diamond.2021.108637.

[39] W. Cho, M. Schulz, V. Shanov, Growth and characterization of vertically aligned centimeter long CNT arrays, Carbon N Y 72 (2014) 264–273. https://doi.org/10.1016/j.carbon.2014.01.074.

[40] Y. Li, G. Xu, H. Zhang, T. Li, Y. Yao, Q. Li, Z. Dai, Alcohol-assisted rapid growth of vertically aligned carbon nanotube arrays, Carbon N Y 91 (2015) 45–55. https://doi.org/10.1016/j.carbon.2015.04.035.

[41] Q. Li, X. Zhang, R.F. DePaula, L. Zheng, Y. Zhao, L. Stan, T.G. Holesinger, P.N. Arendt, D.E. Peterson, Y.T. Zhu, Sustained growth of ultralong carbon nanotube arrays for fiber spinning, Advanced Materials 18 (2006) 3160–3163. https://doi.org/10.1002/adma.200601344.

[42] J. Haidari, M.B. Khabbaz, H. Radman, M. Maghrebi, M. Baniadam, Effect of carbon precursor flowrate on the quality and quantity of carbon nanotubes, Diam Relat Mater 125 (2022) 108984. https://doi.org/10.1016/j.diamond.2022.108984.

[43] Z. Cao, Z. Sun, P. Guo, Y. Chen, Effect of acetylene flow rate on morphology and structure of carbon nanotube thick films grown by thermal chemical vapor deposition, Front Mater Sci China 1 (2007) 92–96. https://doi.org/10.1007/s11706-007-0017-x.

[44] W.Z. Li, J.G. Wen, Y. Tu, Z.F. Ren, Effect of gas pressure on the growth and structure of carbon nanotubes by chemical vapor deposition, Appl. Phys A Mater Sci Process 73 (2001) 259–264. https://doi.org/10.1007/s003390100916.

Chapter 4

Synthesis and Characterization of Tungsten deposited via different techniques

The experimental set up and deposition techniques used for depositing tungsten has already been discussed in chapter 2. In this chapter, the morphological and chemical characterization of the W/WO$_x$ film grown on Si(100) substrate will be presented.

4.1 Tungsten film deposited via sputtering

To optimize the growth conditions, we deposited 100 nm of tungsten on Si(100) substrate. The thickness of the film was checked by profilometer.

SEM, AFM and XPS analysis of the grown film was done to study the surface morphology and chemical state of the film.

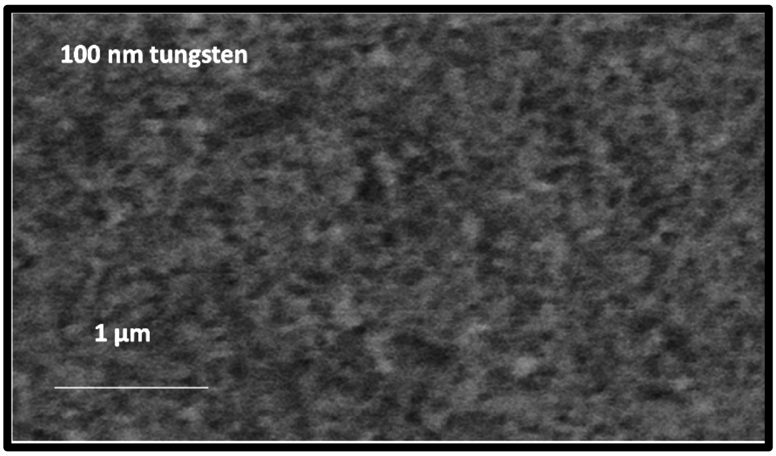

Figure 4. 1 SEM image of a 100 nm thick film of tungsten deposited via DC Magnetron sputtering at room temperature

From the SEM top view image, the film deposited shows a featureless structure.

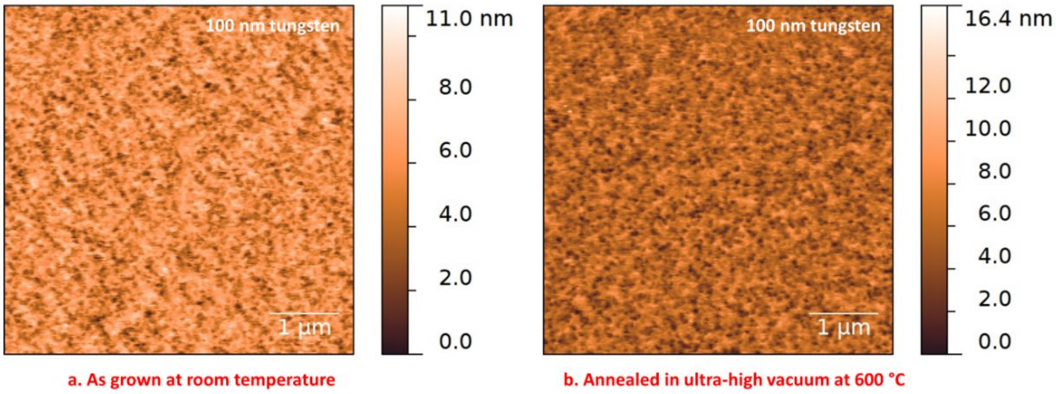

a. As grown at room temperature

b. Annealed in ultra-high vacuum at 600 °C

Figure 4. 2 AFM images of a. as grown b. annealed in ultra-high vacuum at 600 °C of 100 nm of tungsten thin film

Ex-situ AFM measurements were used to study the topography of the as grown film deposited at RT, after annealing in ultra-high vacuum at 600 °C. The average roughness of the samples was (1.23 ± 0.04) nm and 1(.49 ± 0.19) nm for the as grown and annealed sample, respectively, as measured using the Gwyddion software. The surface of tungsten film, when annealed at 600 °C become coarsened in comparison to the as grown sample.

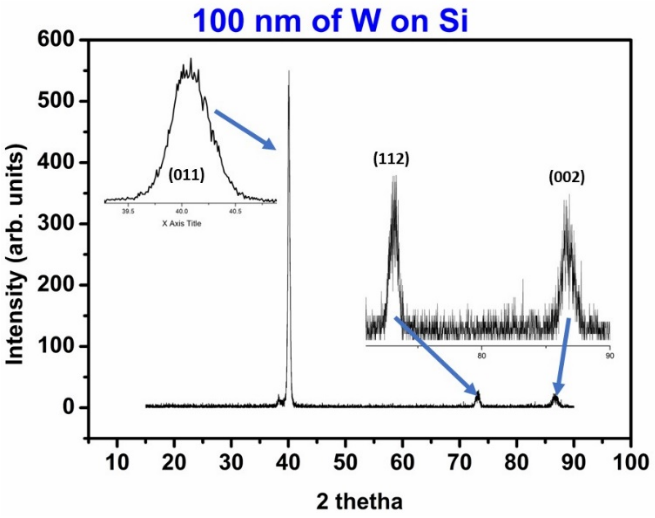

Figure 4. 3 XRD spectrum of W 100 nm film showing the presence of α-W

The spectrum shown in figure 4.3 shows the presence of α-W. All the peaks (011), (112), and (002) at 40.1°, 74.5° and 87.1° corresponds to α-W. For films with thickness >7 nm on SiO_2/Si substrate mostly α-W presence dominates the sample [1].

From the XRD data, estimation on the size of grain can be done, using Scherrer formula

Equation 5.1

$$D = \frac{0.94\lambda}{\beta cos\theta}$$

where λ is the Xray wavelength, β is the FWHM of the diffraction peak intensity, and θ is the Bragg angle.

Equation 5.1 relates the grain size to the broadening of a diffraction peak; the average grain size is given by the equation and was found out to be 21.55 nm.

To study the composition and the electronic and chemical state of the samples, after deposition (air exposed) and annealing the sample in UHV condition at 600 ºC, photoemission spectroscopy was performed.

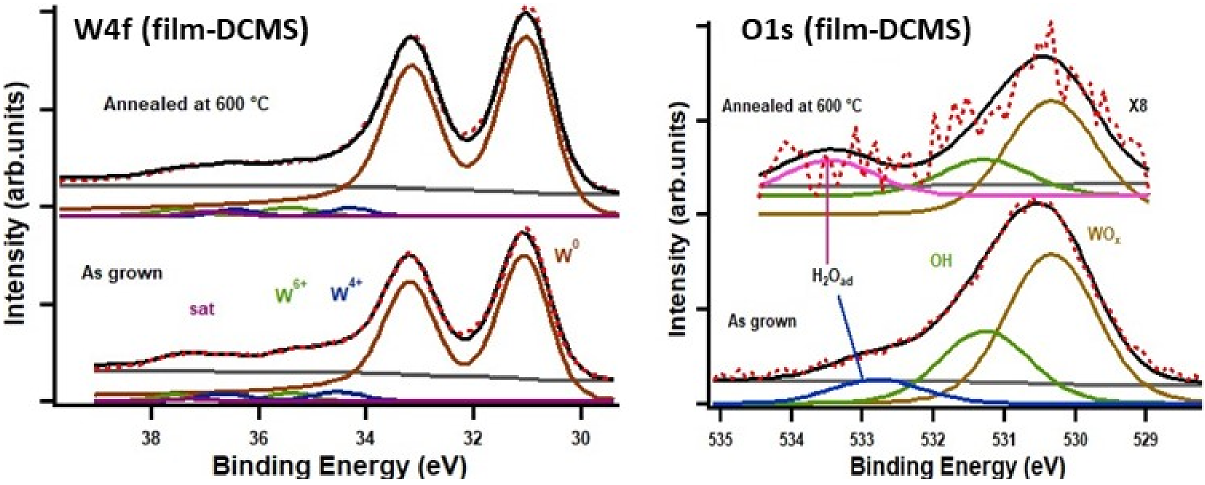

Figure 4. 4 XPS spectra of W4f and O1s of W film exposed to air and measured at RT and annealed in ultra-high vacuum at 600 °C for 5 min

Figure 4.4 (left) and table A1.11 show a mixture of metallic tungsten and tungsten oxides, as tungsten is well known to oxidize instantly in an ambient atmosphere. The W4f spectrum was reproduced using doublets of Donjach-Sunjic line shape, where the energy splitting (2.14 eV) and full width at half maximum (FWHM) were initially constrained, then allowed to vary during the fitting procedure. The presence of the W^0 doublet was observed at 30.95 eV ($W4f_{7/2}$) and 33.09 eV ($W4f_{5/2}$). The W^{4+} and W^{6+} doublets were observed at 34.3 eV ($W4f_{7/2}$) and 36.4 eV ($W4f_{5/2}$) and 35.5 eV ($W4f_{7/2}$) and 37.4 eV ($W4f_{5/2}$) for the as grown and annealed samples, respectively. In both the samples satellite peaks were observed. In the as grown sample, the satellite peak appeared at 37.4 eV, whereas after annealing it was at 36.8 eV [2].

We measured the W*4f* photoemission spectra on the as deposited films. After exposure to the air, tungsten forms an oxide layer on top. The thickness of the oxide layer was calculated using equation 4.1 [3]:

$$d = \lambda_{ox} ln(\frac{I_{ox} * N_m * \lambda_m}{I_m N_{ox} \lambda_{ox}} + 1) \qquad \textit{Equation 4. 1}$$

Where subscript ox and m corresponds to oxide and metal, λ is the electron inelastic attenuation length at the kinetic energy of the emitted photoelectrons and is I is the intensity of photoemission peaks measured. In this case oxide has formed a layer on tungsten film, therefore attenuation of the metallic W *4f* photoemission peak was calculated. Value for the λ_m used is by the average value reported from Tanuma, Powell, and Pen (from optical data and formula predictive) which was 16.2 Å and for λ_o it was 20.8 Å. Equation 1 is correctly used to establish the thickness of a continuous film deposited in layer-by-layer mode (Frank-van der Merve mode), hence in our case only rough estimation of the surface oxide can be made. From the above discussion the calculated thickness of the oxide layer was 1.83 Å [4]. Figure 4.4(right) and table A1.12 show O 1s XPS spectra of the sample before and after annealing. In the XPS spectra for both as grown and annealed sample, three peaks of different intensities at BEs of (530.1 ± 0.2) eV, (531.4 ± 0.2) eV and 533.1 ± 0.3 eV can be distinguished. Peak at (530.1 ± 0.2) eV referred to the presence of WO_x. O 1s peaks at BEs ca. (531.4 ± 0.2) eV corresponded to OH^- and ~(533.1 ± 0.3) eV is related to H_2O_{ad} [5,6].

UPS spectra of HeII (hν = 40.7 eV) was acquired for both samples. From the figure 4.5, the presence of metallic states for the air exposed sample was also evident by theW5d states at the Fermi level (inset). After annealing at 600 °C in the UHV, the sample showed growth of states at the Fermi level. Pointing towards the increase of the metallic states, whose density is higher compared to the air exposed sample. Moreover, after annealing a well-defined peak appeared at 3.3 eV below Fermi level. This referred to the W5d in-gap states, that is filled due to the presence of the oxygen vacancies. These sorts of states are not observed in the pure WO_3. There were two peaks in the air exposed sample at ca. 4.5 eV and 6.7 eV, related to O2p and W5d-O2p hybridized state, respectively [7–9].

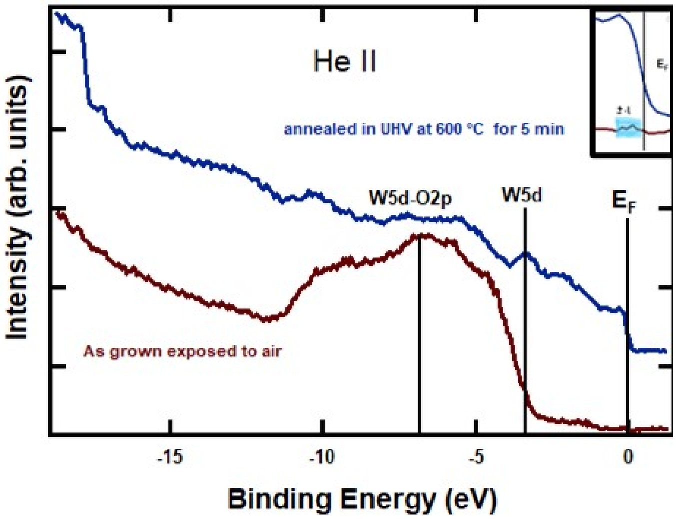

Figure 4. 5 Expanded view of the VB spectra for as grown (purple) and annealed in UHV (blue)

The film deposited via DCMS, as shown from the AFM characterization, is smooth and when exposed to air chemisorbs oxygen. After annealing the sample in UHV condition at 600 °C the contamination on the surface of the film is removed. However, 600 °C is too low to completely reduce the WO_x film or generate any major changes in the deposited film. From

VB spectra it was noted that after annealing some new states appeared, referring to trending towards metallicity.

As already known in literature, the UHV annealing process at 600 °C does not allow a complete reduction of the W film. In the context of gas sensing applications, the oxygen deficient sites significantly contribute more to the sensor sensitivity enhancement. With the reduction of these sites, sensitivity will be affected. Consequently, to maintain a high level of sensitivity under vacuum conditions, it is preferential to operate at lower operating temperatures.

4.2 Tungsten oxide film deposition via DC magnetron sputtering

100 nm of WO_x film was deposited on Si(100) substrate via DCMS. 20 sccm Ar along with 3 sccm oxygen was used during the sputtering process as explained in chapter 2. To find the chemical composition of the sample ex-situ XPS analysis was done.

In figure 4.6 (table A1.13 and A1.14), the photoemission spectra of W 4f (left) and O1s (right) spectra are shown. The deconvolution of W 4f photoemission peak for the film deposited in the oxygen atmosphere was accomplished. The position of the peaks with the BEs of W 4f were observed at ca. 31.4 eV, 34. 74 eV, 35. 43 eV, and 41.08 eV were observed. The spin–orbit splitting of the doublet were 2.13 -2.17 eV (with a peak ratio of 4: 3). The peak position and line shape of these peaks represent W atoms with 2+, 5+ and 6+ oxidation states and a satellite peak.

The signal of the oxide corresponds to the high B.E in the spectrum, because compared to the W, oxygen is more electronegative. The oxide broadening can be referred to phonon. Furthermore, oxide is considered less ordered than the metals, which can also contribute to peak broadening.

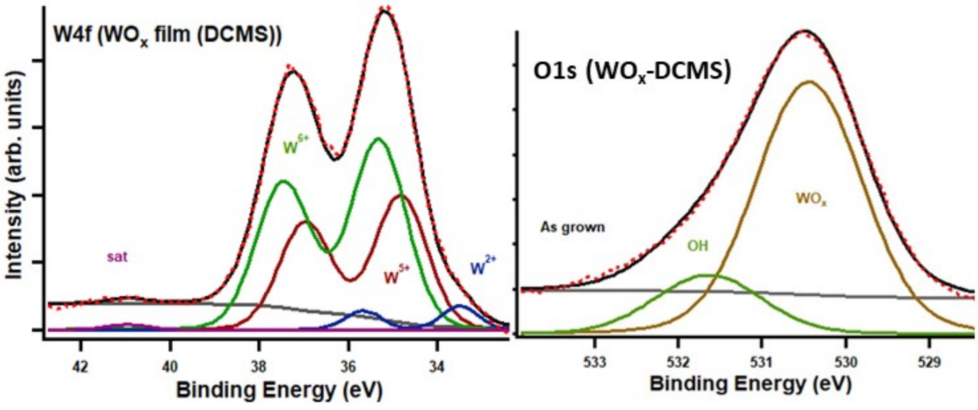

Figure 4. 6 XPS core level spectra of W4f and O1s of WO_x film exposed to air and measured at RT

The O 1s photoemission peaks are also shown in Fig. 4.6. The O 1s BEs of the WO_x film were found at peak position 530.6 eV, which corresponded to the typical W–O bond. Furthermore, the O 1s XPS peak was quite broad for the WO_x film, while the deconvolution of this peak exposed an extra peak 531.7 eV BE, which could be assigned to hydroxyl groups (–OH) [6]. The difference between figure 4.4 and 4.6 can be clearly observed. Figure 4.4 showed XPS of the film of metallic tungsten, which got oxidized when exposed to air. Whereas for WO_x deposited film, different oxidation states were present without any metallic phase of tungsten. These oxide films are utilized in gas sensing applications because they can easily sense oxidizing as well as reducing gases.

4.3 Tungsten deposition via Cluster source

For the synthesis of WO_x films with controlled stoichiometry and amorphous structure, supersonic cluster beam deposition (SCBD) was carried out with a pulsed micro plasma cluster source (PMCS), as discussed in chapter 2.

For structural and morphological analysis ex-situ SEM and TEM measurements were done. They showed that the nanostructures formed are nano porous and composed of amorphous phases along with some crystalline nanoparticles.

Argon as carrier gas along with oxygen was used during the deposition process. Different concentration of mixtures of $Ar + O_2$ were used to control the stoichiometry of the WO_x. After deposition, the NS film sample was transferred to the analysis chamber (pressure $< 5 \times 10^{-10}$ mbar) without breaking the vacuum. In-situ XPS characterization was done to study the stoichiometry and electronic structure of the as- grown samples, after air exposure. VB and WF measurements were done using a He lamp (He I, 21.22 eV and He II, 40.8 eV). High resolution SEM and TEM images were attained to study the morphology of the sample.

From ex-situ SEM, the NS have dendritical shape, where the surface showed granular nature with the presence of nanopores, as shown in figure 4.7 [10,11].

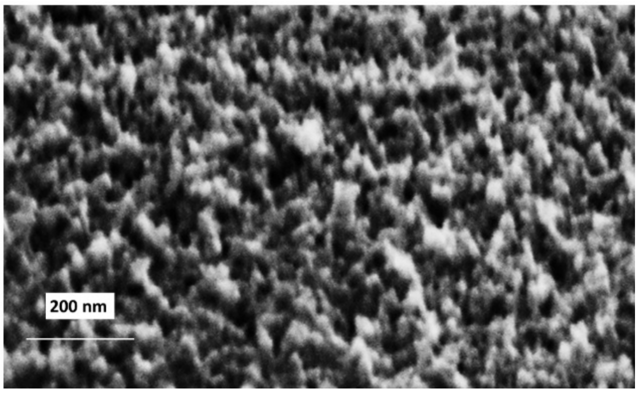

Figure 4. 7 SEM images of WO_x Clusters. From the image granularity of the film is clear.

From the ex-situ TEM images, aggregated small NPs are clearly observable as shown in figure 4.8. In addition to that, TEM analysis showed the coexistence of amorphous and crystalline nanoparticles in the NS film. The presence of amorphous material was confirmed by a selective area electron diffraction (SAED) pattern, indicating that the NPs are amorphous. But in a different region of the sample, crystalline NPs are evident (figure 4.9). Calculated lattice spacing were 0.38 nm and 0.37 nm, in close agreement with lattice spacing (001) and (110) and of WO_3.

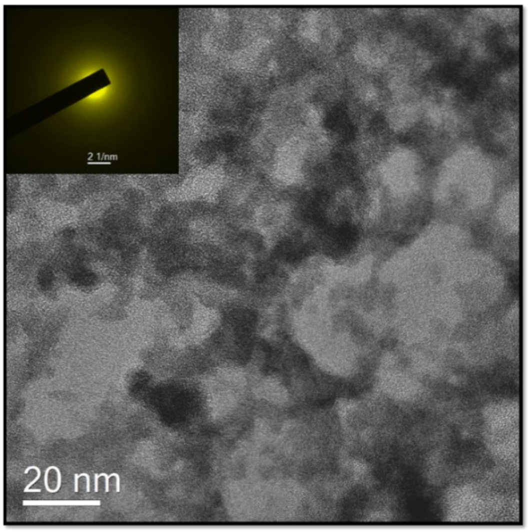

Figure 4. 8 TEM image of WO_x clusters. The dendritically shaped aggregated structures are seen. SAED pattern (inset), shows a diffuse background, signature of amorphous materials

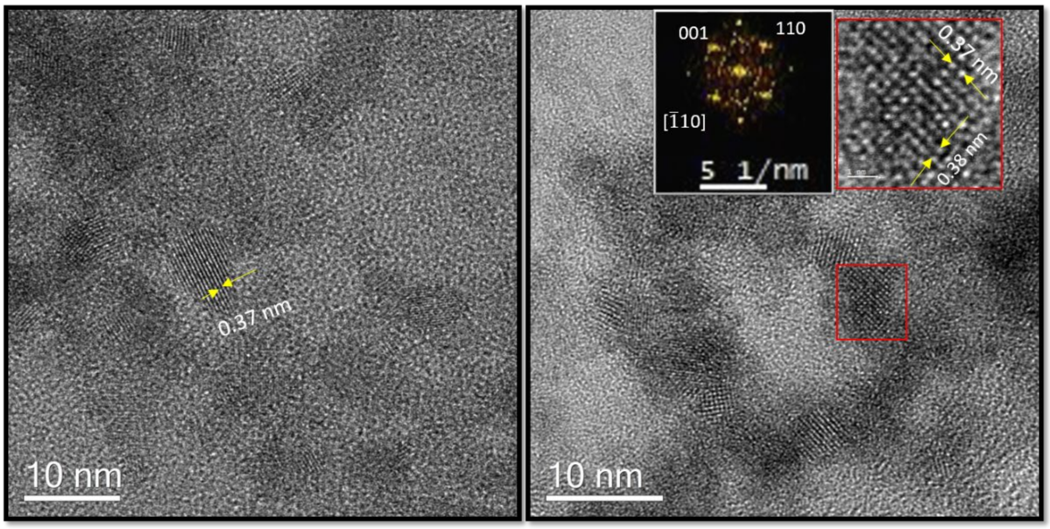

Figure 4. 9 TEM image of WO_x sample. Presence of crystalline NPs is visible. Lattice spacing of 0.37 and 0.38 nm are clearly noticeable.

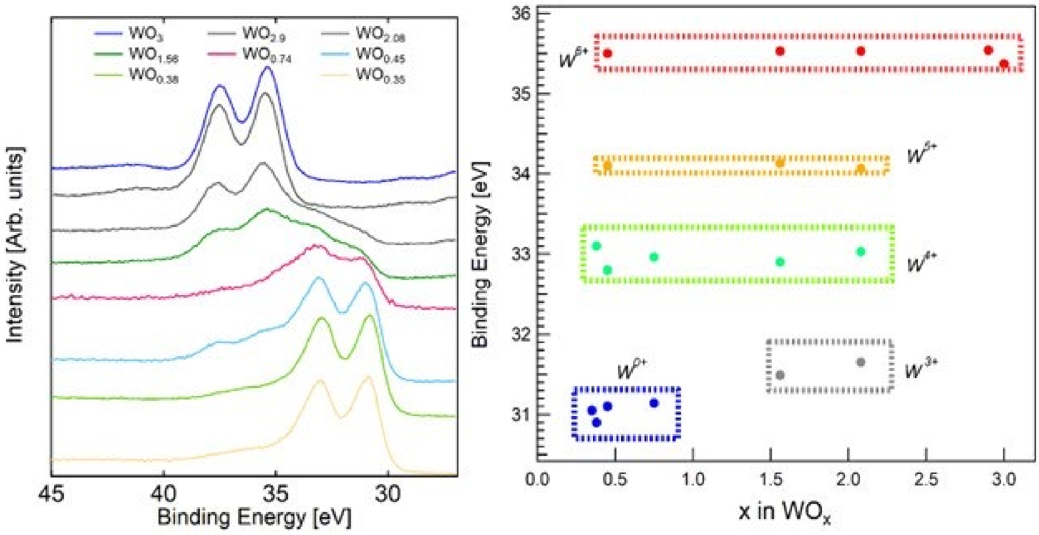

Figure 4. 10 Left: W4f spectra for WO_x NS films with different oxygen concentration. Right: Binding energy position of the different oxidation states components extracted by the fitting procedure as a function of the WO_x stoichiometry. The coloured frames are centred on the average BE value for each oxidation state and are wide along the BE axis.

In figure 4.10, W4f core level spectra for various WO_x films are shown which were acquired in-situ, without any air exposure. The stoichiometry of the nanoparticles was changed by mixing Ar (high purity Ar: 99.9995%) as carrier gas, with a controlled amount of oxygen. The change in the W4f as a function of oxygen concentration has a very similar trend to what is reported in the previous in-situ etching study [12]. It is interesting to observe that samples with sub stoichiometric compositions have more oxidation states peaks than the stoichiometric composition, for example comparing $WO_{0.74}$ with WO_3 sample. This is a clear sign of the coexistence of multiple phases within the films.

We note that the analysis of the stoichiometry of the NS film, obtained from the fitting of the XPS core levels, can only give us the average oxidation state of the film. Therefore, it is difficult to differentiate all the different phases present. The fact that not all the oxides of tungsten are stable further complicates the phase identification. With appropriate thermodynamic conditions and selection of proper precursor, W_2O_3 can be isolated only in a very narrow window [13]. This can be the partial explanation of the presence of components of oxidation states 5+ and 6+ when the stoichiometry is $1.5<x<2.5$. When $x<1$, the presence of 4+ oxidation state can be justified by considering that in presence of a small amount of oxygen in the carrier gas, the conditions for the homogeneous oxidation of all the NP are not favourable. In figure 4.10 it is reported the oxidation states fraction present in the films as a function of stoichiometry and oxygen percent in the gas during deposition.

The trends displayed in figure 4.11 identified the presence of phase coexistence not close to the lower and upper limits of the stoichiometry range. For x=2.08 and 1.56, coexistence of 6+ to 3+ oxidation states were observed. This highlights that when all the NP were not homogeneously oxidized by the oxygen in the gas mixture, a distribution of oxidation states was present. For $x<1.5$ only W^{0+} and W^{4+} can be observed pointing to the fact that the 3+ oxidation state was not favoured in a poor oxygen environment. Although an exceptional behaviour for $x = 0.45$ (which is $x < 1.5$) was observed. At this x concentration four following W states were observed: 0, 4+, 5+ and 6+. Which may have occurred due to some experimental error, like imperfect control of oxygen in the mixture.

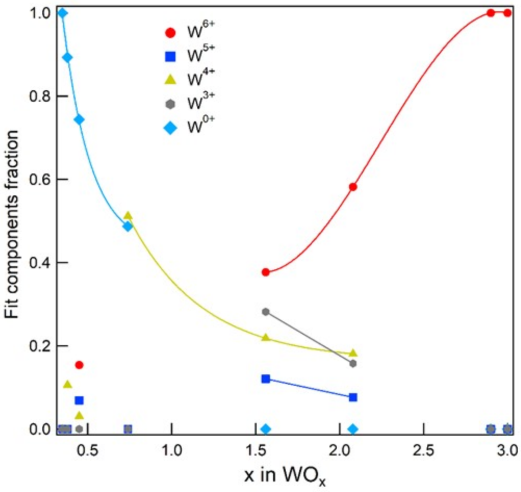

Figure 4. 11 Fraction of the fit components as a function of the film stoichiometry. The continuous lines are a guide for the eyes

Afterwards we exposed these samples to the atmosphere for few months and took XPS. One of the sample data is shown in figure 4.12 (table A1.15). From this figure the sample was oxidized, peak at 35.2 eV is W^{5+} phase, whereas W^{6+} phase can be observed at BE 35.6 eV. Whereas the in-situ spectrum is showing different oxidation states in the sample.

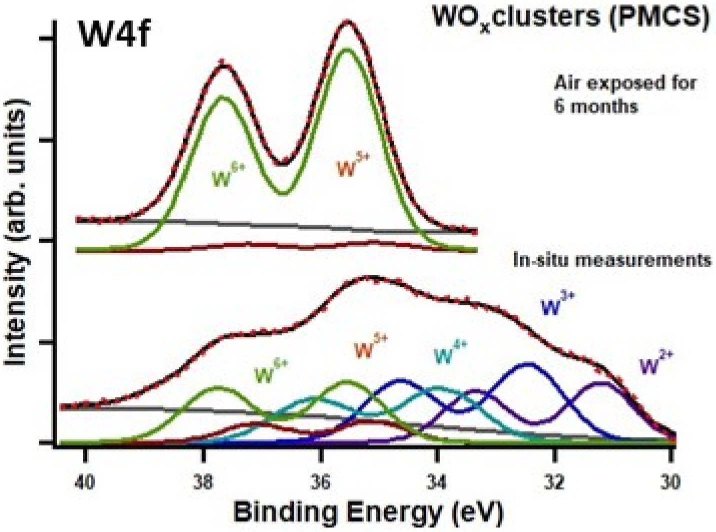

Figure 4. 12 In-situ and air exposed XPS measurement of WO_x clusters deposited via PMSC

Using a PMCS it is viable to synthesize amorphous WO_x NS film characterized with controllable stoichiometry. The nanometric size of these clusters allow to obtain phases that are not stable otherwise. Also, the narrow band gap as reported in literature (approximately 2.5 – 2.8 eV) of sub stoichiometric WO_{3-x} has shown exceptional electron transport and photosensitive characteristics. Because of oxygen deficient sites in WO_{3-x} it has been extensively tested for the applications like gas sensing, electrochromic catalysis etc [14].

4.4 Reference

[1] J.-S. Lee, J. Cho, C.-Y. You, Growth and characterization of α and β -phase tungsten films on various substrates, Journal of Vacuum Science & Technology A: Vacuum, Surfaces, and Films 34 (2016). https://doi.org/10.1116/1.4936261.

[2] W. Lisowski, A.H.J. van den Berg, G.A.M. Kip, L.J. Hanekamp, Characterization of tungsten tips for STM by SEM/AES/XPS, Fresenius J Anal Chem 341 (1991) 196–199. https://doi.org/10.1007/BF00321548.

[3] M.R. Alexander, G.E. Thompson, X. Zhou, G. Beamson, N. Fairley, Quantification of oxide film thickness at the surface of aluminium using XPS, in: Surface and Interface Analysis, 2002: pp. 485–489. https://doi.org/10.1002/sia.1344.

[4] S. Tanuma, C.J. Powell, D.R. Penn, Calculations of electron inelastic mean free paths. IX. Data for 41 elemental solids over the 50 eV to 30 keV range, Surface and Interface Analysis 43 (2011) 689–713. https://doi.org/10.1002/sia.3522.

[5] T. Schiros, K.J. Andersson, L.G.M. Pettersson, A. Nilsson, H. Ogasawara, Chemical bonding of water to metal surfaces studied with core-level spectroscopies, J Electron Spectros Relat Phenomena 177 (2010) 85–98. https://doi.org/10.1016/j.elspec.2009.09.009.

[6] S. Rahimnejad, J.H. He, F. Pan, X. Lee, W. Chen, K. Wu, G.Q. Xu, Enhancement of the photocatalytic efficiency of WO_3 nanoparticles via hydrogen plasma treatment, Mater Res Express 1 (2015). https://doi.org/10.1088/2053-1591/1/4/045044.

[7] M. Vasilopoulou, A. Soultati, D.G. Georgiadou, T. Stergiopoulos, L.C. Palilis, S. Kennou, N.A. Stathopoulos, D. Davazoglou, P. Argitis, Hydrogenated under-stoichiometric tungsten oxide anode interlayers for efficient and stable organic photovoltaics, J Mater Chem A Mater 2 (2014) 1738–1749. https://doi.org/10.1039/c3ta13975a.

[8] F. Bussolotti, L. Lozzi, M. Passacantando, S. La Rosa, S. Santucci, L. Ottaviano, Surface electronic properties of polycrystalline WO_3 thin films: A study by core level and valence band photoemission, Surf Sci 538 (2003) 113–123. https://doi.org/10.1016/S0039-6028(03)00696-4.

[9] L. Ottaviano, F. Bussolotti, L. Lozzi, M. Passacantando, S. La Rosa, S. Santucci, Core level and valence band investigation of WO_3 thin films with synchrotron radiation, Thin Solid Films 436 (2003) 9–16. https://doi.org/10.1016/S0040-6090(03)00518-2.

[10] N.M. Hwang, Springer Series in Surface Sciences 60 Non-Classical Crystallization of Thin Films and Nanostructures in CVD and PVD Processes, 01 ed., Springer Dordrecht, 2016. https://doi.org/10.1007/978-94-017-7616-5.

[11] I.N. Kholmanov, E. Barborini, S. Vinati, P. Piseri, A. Podestà, C. Ducati, C. Lenardi, P. Milani, The influence of the precursor clusters on the structural and morphological evolution of nanostructured TiO_2 under thermal annealing, Nanotechnology 14 (2003) 1168–1173. http://iopscience.iop.org/0957-4484/14/11/002.

[12] F.Y. Xie, L. Gong, X. Liu, Y.T. Tao, W.H. Zhang, S.H. Chen, H. Meng, J. Chen, XPS studies on surface reduction of tungsten oxide nanowire film by Ar + bombardment, J Electron Spectros Relat Phenomena 185 (2012) 112–118. https://doi.org/10.1016/j.elspec.2012.01.004.

[13] C.L. Dezelah IV, O.M. El-Kadri, I.M. Szilágyi, J.M. Campbell, K. Arstila, L. Niinistö, C.H. Winter, Atomic layer deposition of tungsten(III) oxide thin films from $W_2(NMe_2)_6$ and water: Precursor-based control of oxidation state in the thin film material, J Am Chem Soc 128 (2006) 9638–9639. https://doi.org/10.1021/ja063272w.

[14] M. Zhang, C. Yang, Z. Zhang, W. Tian, B. Hui, J. Zhang, K. Zhang, Tungsten oxide polymorphs and their multifunctional applications, Adv Colloid Interface Sci 300 (2022) 102596. https://doi.org/10.1016/j.cis.2021.102596.

CHAPTER 5

Hybrid Materials

In this chapter we will discuss the characterization of HM prepared as a combination of CNs (CNs and CNTs) as template with tungsten coating. The synthesis of CNTs and deposition conditions for tungsten film/ clusters has already been discussed in chapter 3 and 4 respectively.

5.1 DCMS of Tungsten (bias: 0V) on the CNs obtained on SiO_2 using Ni as catalyst

The CNs shown in chapter 3 are used as substrates to deposit W of different thickness via DCMS, exploiting the optimised conditions stated in chapter 4 section 1. In this section the following abbreviations will be used to define the samples under discussion:

100nmWO_x/CNs@500C, 500nmWO_x/CNs@500C for 100 nm and 500 nm tungsten deposited on CNs grown at 500 °C.

100nmWO_x/CNs@600C, 500nmWO_x/CNs@600C for 100 nm and 500 nm tungsten deposited on CNs grown at 600 °C.

100nmWO_x/CNs@700C, 500nmWO_x/CNs@700C for 100 nm and 500 nm tungsten deposited on CNs grown at 700 °C, respectively.

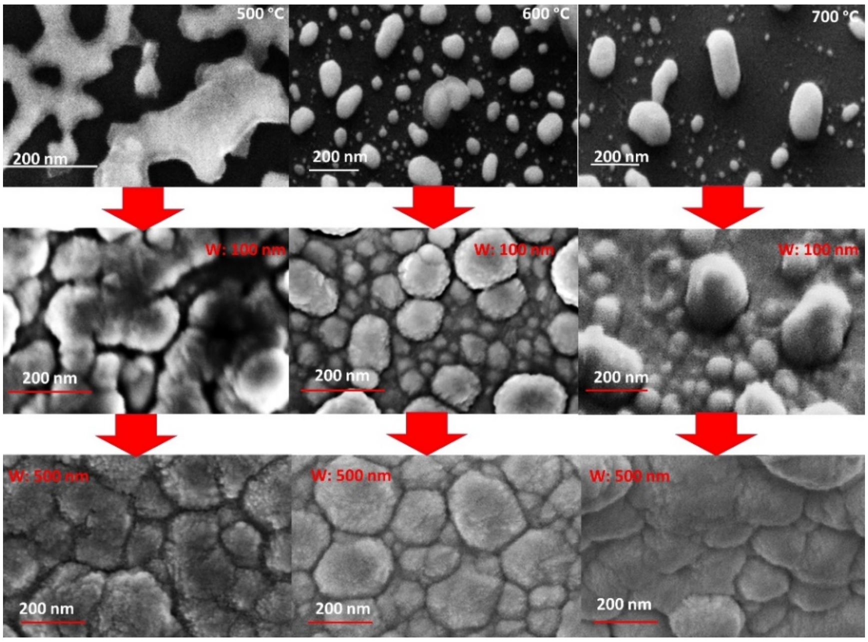

Figure 5. 1 SEM images (tilted at 45°) of CNs (Column left) grown at 500 °C; (top) CNs, (middle) 100 nm W deposited, (bottom) 500 nm of W deposited, (middle column) CNs grown at 600 °C; (top) CNs, (middle) 100 nm W deposited, (bottom) 500 nm of W deposited, (right column) CNs grown at 700 °C; (top) CNs, (middle) 100 nm W deposited, (bottom) 500 nm of W deposited

Only the sample grown at T higher than 500 °C are shown, because at 400 °C only few SWCNT along the substrate were seen. Fig. 5.1 show the bare CNs (top) grown at 500 ºC, 600 ºC and 700 ºC and after the deposition at RT of 100 nm (centre) and 500 nm (bottom) of tungsten via DCMS. No substrate biasing was applied during all depositions. It is clear that W deposition causes a progressive increasing of the CNs dimension, together with a change in the surface roughness.

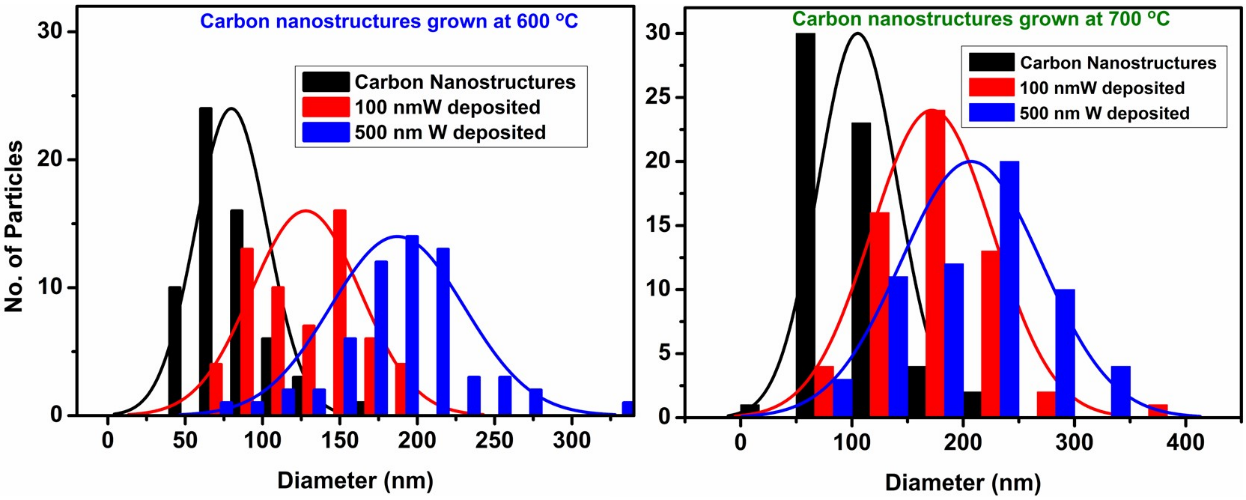

Figure 5. 2: Size distribution histogram and Gaussian fitting for the CNs grown at 600 °C (left) and 700 °C (right) without W (black), with 100 nm W deposited top (red), and 500 nm of W deposited on CNs (blue)

To quantify the change in the NP's (pebble shaped) dimension upon W deposition, ImageJ software was used, by measuring, for each sample, the mean diameter dimension of 60 nanoparticles. The results are shown in figure 5.2 relative for the CNs grown at 600 °C (left) and 700 °C (right). For each sample, the solid line indicates the resulting Gaussian distribution curve, as a function of W thickness. In particular, in the case of the CNs grown at 600 ºC the average dimension size goes from (66 ± 1.99) nm (Fig. 5.2, left black) before W deposition to (125 ± 4.5) nm (Fig. 5.2, left red) after depositing 100 nm and (170 ± 4.8) nm (Fig. 5.2, left blue) after the deposition of 500 nm W, respectively. In the case of the CNs grown at 700 °C we found that the average dimension size goes from (100 ± 1.09) nm (Fig. 5.2, right black) before W deposition to (170 ± 5.9) nm (Fig. 5.2, right red) and (210 ± 6.4) nm (Fig. 5.2, right blue) after the deposition of 100nm and 500nm of tungsten, respectively

The change in the lateral dimension goes together with a change in the sample's roughness, which has been measured via AFM. Fig. 5.3 shows the AFM images acquired on the 3 samples after the deposition of 100 nm together with some significant line roughness profiles.

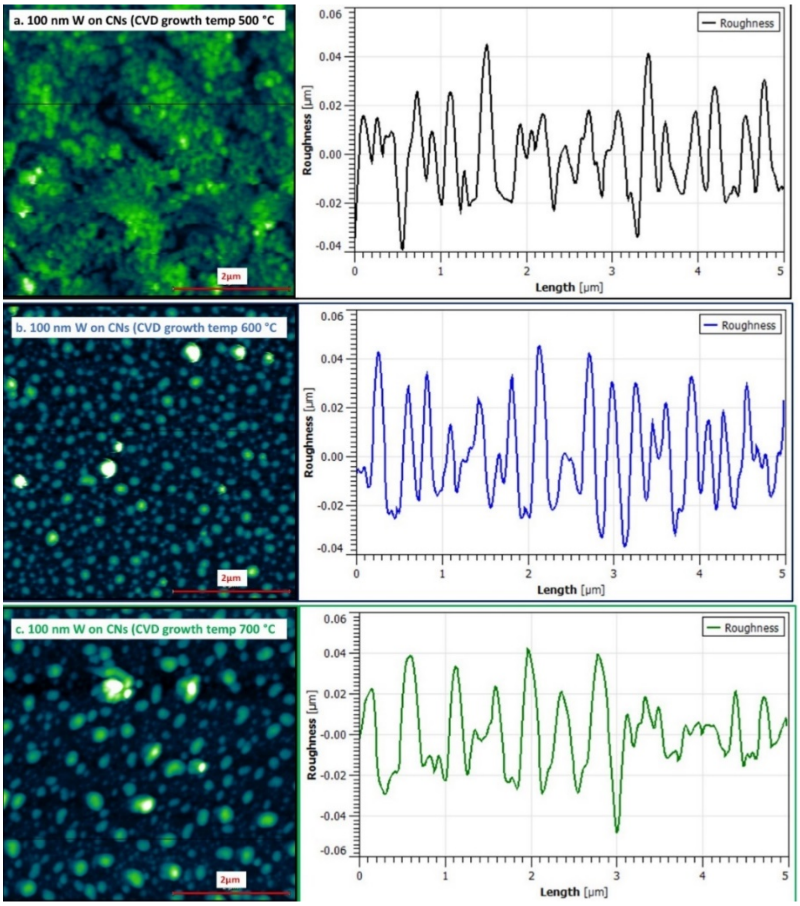

Figure 5. 3 2D Images and roughness profile of the samples obtained from the AFM images from Gwyddion software from top to bottom for 100 nm tungsten deposited on CNs grown at 500 °C, 600 °C and 700 °C from top to bottom

The resulting roughness, as extracted by the Gywddion software, are plotted in figure 5.4 as a function of the growth temperature of the CNs. The plot shows the comparison of roughness before and after depositing W on CNs. Even if the original morphology is preserved, it is clear that after 100nm of W deposition, within the experimental error, for all the nanostructures, the roughness decreased from about (18 ± 1.5) nm to about (13 ± 02) nm.

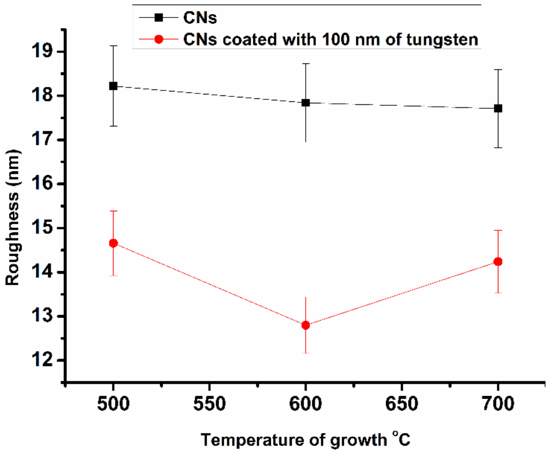

Figure 5. 4: Roughness of the sample Vs CVD growth temperature before and after depositing 100 nm W, as revealed by AFM measurements

As seen in the case of W deposition on the flat SiO_2 substrate, XRD showed the presence of only α W, as shown in figure 4.3. In figure 5.5 the peaks appearing at 39.9° corresponds to the (110) plane of the body centred cubic (bcc) phase of α-W, which is the thermodynamically stable phase of W [1,2]. At ~35.5°, the peak (200) indicating that another phase of W called β-W is also present. The strongest peak at 29.3° refers to Si (111), substrate. In the figure 5.5, inset shows the two peaks stated above. I. Djerdj et al., reported that presence of both phases of W, depends on argon (Ar) pressure during deposition. Low Ar pressure facilitates the α-W phase as compared to β-W [3].

The presence of both a and β phases of tungsten may be attributed to the CNs template.

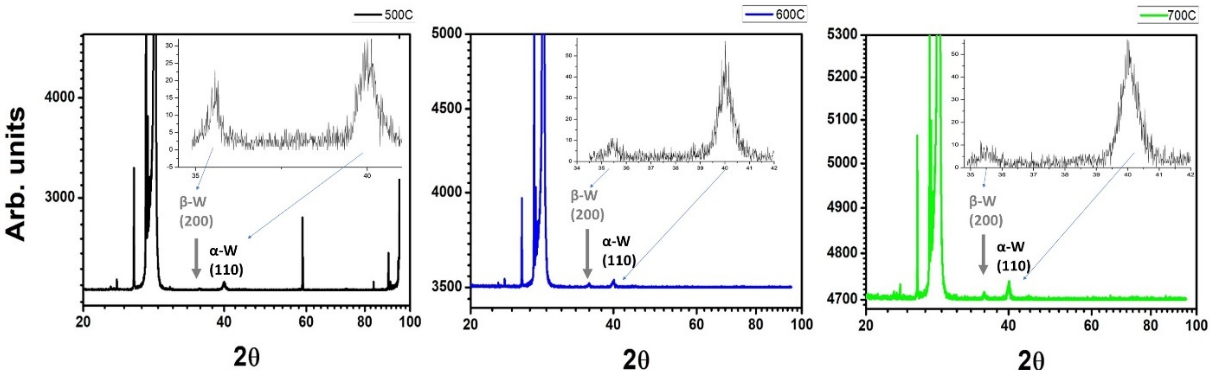

Figure 5. 5: XRD spectra showing presence of α-W and β-W in 100 nm of tungsten film deposited on CNs grown at 500 °C (black), 600 °C (blue) and 700 °C (green).

As discussed in chapter 4, the grain size is calculated using Scherrer formula. In all the three cases, the grain size is smaller for α-W as compared to β-W. Furthermore, as the grain size for α-W showed increasing trend on CNs grown at higher temperature, whereas β-W showed the decreasing trend. This is summarized in the table 5.1

Serial No.	W film thickness (nm)	CVD growth temperature (° C)	Grain size (α-W) (nm)	Grain size (β-W) (nm)
1	100	500	10.10	36.22
2	100	600	11.38	20.26
3	100	700	12.99	19.37

Table 5. 1 Grain size calculated using Scherrer formula for the CNs deposited with 100 nm of tungsten

To analyse the composition and chemical state of the samples, we performed XPS measurements. Fig. 5.6 shows the XPS spectra after the 100 nm W deposition. All spectra are acquired after air exposure at RT in normal emission geometry, calibrating the binding energy scale at the Fermi level. Various oxidation states of tungsten have been identified in various studies. In an article by Martin Wilken et. al., it is stated that various stable oxides and suboxides of tungsten can exist on the surface such as WO, WO_2, W_2O_3,

W_4O_3, $W_{17}O_{47}$, $W_{18}O_{49}$, and WO_3 (in an oxygen-deficient form WO_{3-x}) [4]. Tungsten when exposed to air can adsorb oxygen from the atmosphere and can lead to W^{6+}, W^{5+}, W^{4+}, W^{3+}, and W^{2+} along with W^0 states. The BEs relating to the various oxidation states change noticeably in the literature, depending on the energy reference. From the previous studies [5–7], we adopted the following values for the W 4f: W^{6+} (35.6 ± 0.2) eV, W^{5+} (34.8 – 35.3) eV, W^{4+} (33.7 – 34.6) eV, W^{3+} (32.6 – 33.6) eV, W^{2+} (31.4 – 32.4) eV, and W^0 (30.5- 31.2) eV [4,8].

All the spectra were fitted using Donjach-Sunjic line shapes superimposed by a Shirley background The XPS spectra of W4f was taken. In the spectra for W4f, as shown in figure 5.6 (table A1.16), peak appearing at 30.9 eV and ~ 33 eV are associated with $W4f_{7/2}$ and $W4f_{5/2}$ of metallic tungsten respectively. Moreover, as noted spin orbit coupling of ~ 2.1 eV between the mentioned peaks are in accordance with the literature, suggesting the presence of W^0 state of W [9].

The BE observed at 31.8 eV corresponds to W^{2+} [7]. After deconvolution, the doublet found in our samples at peak positions ~ 34.7 eV and 36.8 eV, and 35.5 eV and 37.6 eV are in line with $W4f_{7/2}$ and $W4f_{5/2}$ referring to W^{5+} and W^{6+} respectively [10], as shown in figure 5.6. After deposition of W on CNs, we observed that along with the presence of metallic tungsten, WO_{3-x} states are also present.

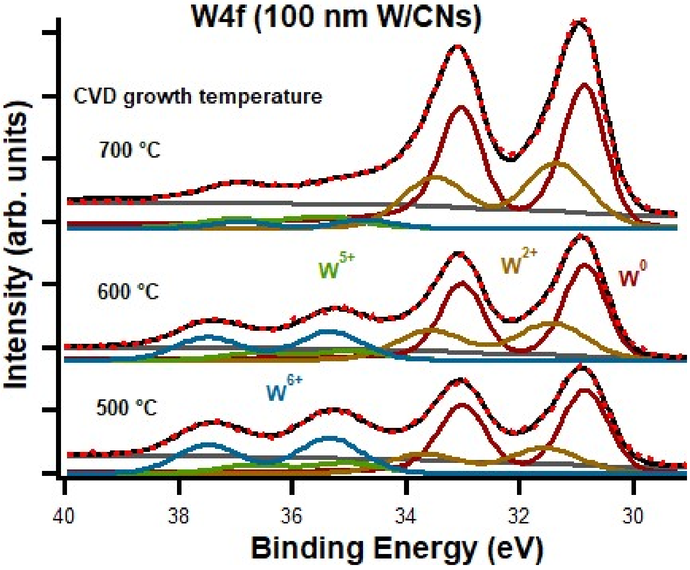

Figure 5. 6: XPS spectra of W after depositing 100 nm of W on CNs

We have shown in this section that CNs as template can be used to obtain nanostructured tungsten via DCMS. The CNs that we have obtained (elongated more like peapods) are different from already reported, nanospheres, nano onions, nano flowers etc. As we have deposited W at RT, and did ex-situ characterization, presence of various tungsten oxide states was observed. We calculated the thickness of the oxide film on W film after air exposure by using the formula already discussed in chapter 4 [11,12].

The thickness of oxygen film adsorbed form the atmosphere in 100nmWO_x/CNs@500C, 100nmWO_x/CNs@600C and 100nmWO_x/CNs@700C is 9.59 Å, 16.08 Å and 10.07 Å, respectively.

The hybrid that we obtained can be considered as a capsule, with a core of CNs surrounded by tungsten film. The SEM and AFM characterizations revealed variation in surface roughness associated with the CNs morphology. From XRD analysis, $\alpha - W$ was dominant as compared to $\beta - W$.

These hybrid NS can find application in photoelectrochemical decomposition of water as a renewable energy source, in gas sensing applications, and can be investigated as a material for stability for the plasma facing wall in the fusion machines.

5.2 DCMS of Tungsten (bias: 0, -50eV) on CNTs

The CNTs shown in chapter 3 are used as templates to deposit W via DCMS, exploiting the optimised conditions stated in chapter 4 section 1. W was deposited on the CNTs with and without applying bias to the substrate. In this section the following abbreviations will be used to define the samples under discussion:

100nmWO_x(G)/CNTs@600C, 100 nm tungsten deposited (keeping substrate grounded) on CNTs grown at 600 °C on SiO_2/Si(100) substrate.

100nmWO_x(B)/CNTs@600C, 100 nm tungsten deposited (applying -50 V biasing to the substrate) on CNTs grown at 600 °C on SiO_2/Si(100) substrate.

100nmWO_x(G)/CNTs@700C, 100 nm tungsten deposited (keeping substrate grounded) on CNTs grown at 700 °C on SiO_2/Si(100) substrate.

100nmWO_x(B)/CNTs@700C, 100 nm tungsten deposited (applying -50 V biasing to the substrate) on CNTs grown at 700 °C on SiO_2/Si(100) substrate.

In chapter 3 we have seen that the CNTs grew at 600 °C and 700 °C are approximately 6 - 12 µm long.

Figure 5.7 shows the CNTs forest grown at 600 °C before (left) and after (right) 100nmWO$_x$(G)/CNTs@600C. After deposition the CNTs were uniformly covered by W, maintaining their morphology at micrometric scale.

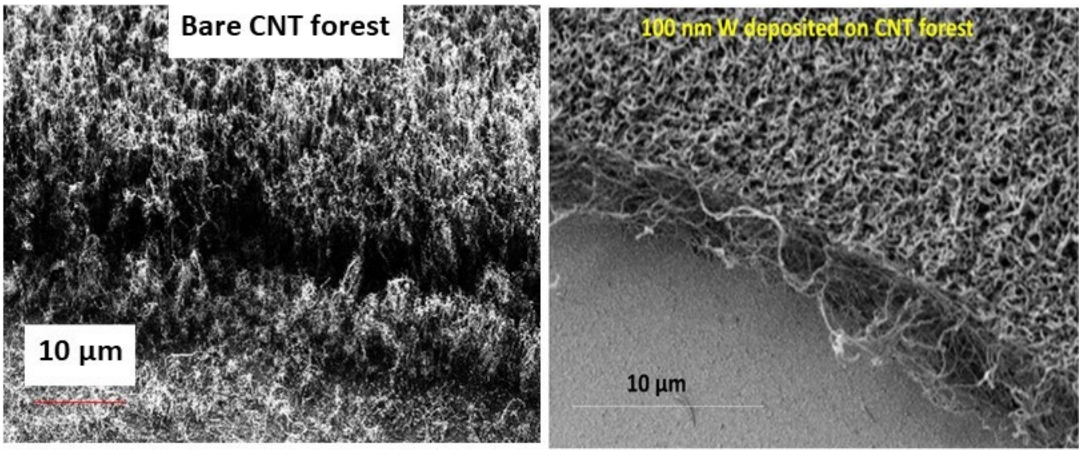

Figure 5. 7 SEM image showing the growth of forest and 100 nm W coating the forest

To estimate the density of the forest, we did the manual counting of CNTs from a SEM image. We counted the roots of the CNTs along one dimension, and then assumed that there will be the same number of CNTs will be in the second direction. Taking a square of no. of CNTs and dividing it by the area, gives us the no. of CNTs/unit area. For the CNT forest grown at 600 °C we found the density to be 463 CNTs/ µm^2 whereas for the forest grown at 700 °C it was only 28 CNTs/ µm^2.

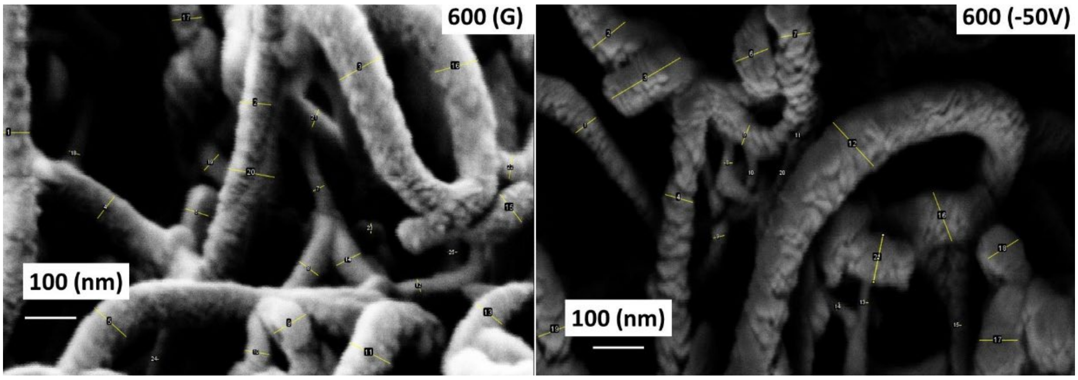

Figure 5. 8: SEM images of the CNT forest grown at 600 °C coated with 100 nm of W (left) without (G) and (right) with biasing (-50V) the substrate

Figure 5.8, acquired using higher magnification, shows in more detail the morphology of the W coating as a function of CVD growth temperature and DCMS bias [14]. We used ImageJ software to calculate the diameter of the tungsten coated CNTs. In figure $100nmWO_x(G)/CNTs@600C$ (left) and $100nmWO_x(B)/CNTs@600C$ (right) showed that the diameter is approximately the same for both the cases on CNTs forest grown at 600 °C.

But the diameter distribution increased after coating 100 nm of W as shown in figure 5.9 on CNT forest grown at 700 °C. The only reasonable explanation is that the density of the forest was only 28 CNTs/ μm^2 (left image), which allowed more coating of W on CNTs as compared to the denser forest shown in figure 5.8.

Table 5.2 gives the average value of diameter for bare CNTs grown at 600 °C and 700 °C, and for the samples coated with 100 nm of W, with and without biasing via DCMS. From the SEM images and values of diameter calculated using ImageJ software, it was observed that the diameter is not affected by the biasing, but the density of the forest can play a substantial role.

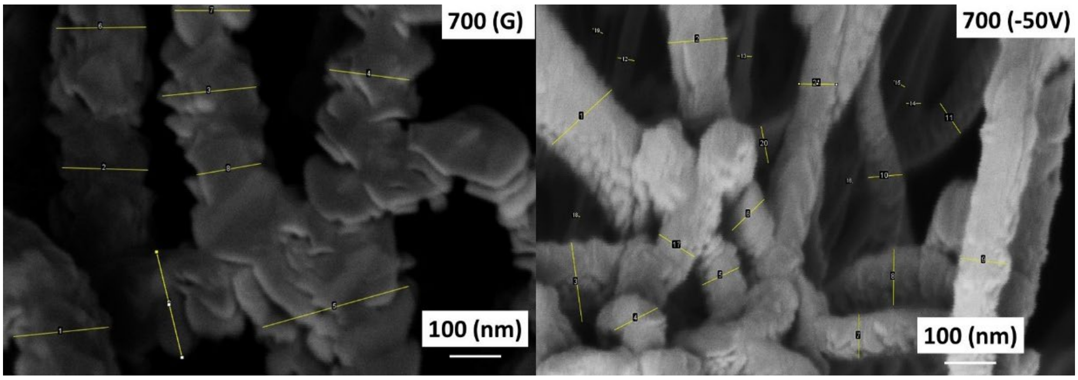

Figure 5. 9 SEM images of the CNT forest grown at 700 °C coated with 100 nm of W (left) without (G) and (right) with biasing (-50V) the substrate

CVD Temperature (°C)	CNT diameter (nm)	CNT+100nm W diameter No BIAS	CNT+100nm W diameter -50eV BIAS
600	13.3 ± 4.5	52 ± 10	53.29 ± 6.8
700	20 ± 7.5	188.1 ± 26.7	74.5 ± 11.8

Table 5. 2 Average diameter of CNTs before and after deposition of 100 nm of W without and with biasing.

As already discussed, to calculate the crystalline grain size, Scherrer formula will be used for the XRD peaks. Table 5.3 gives the grain size as calculated. In figure 5.10 the inset shows the magnified peaks for (α and β) tungsten, as observed in the spectra attained. From the figure both the phases of tungsten were present when deposited (with and without biasing) on CNTs grown at 600 ºC. After analysing the spectra for the samples $100nmWO_x(G)/CNTs@700C$

and 100nmWO$_x$(B)/CNTs@ only α-W was observed, along with Si (100) peak (strongest peak at 69.5°) [13,14].

The α and β phases of tungsten depend upon the thickness of the film. β − W is found mostly when the film thickness is less than 10 nm whereas α − W is predominant in thicker W films [15]. In the previous section both phases of W were present, but in case of CNTs forest we found that when deposited on CNTs grown at 700 °C, only α-W appeared.

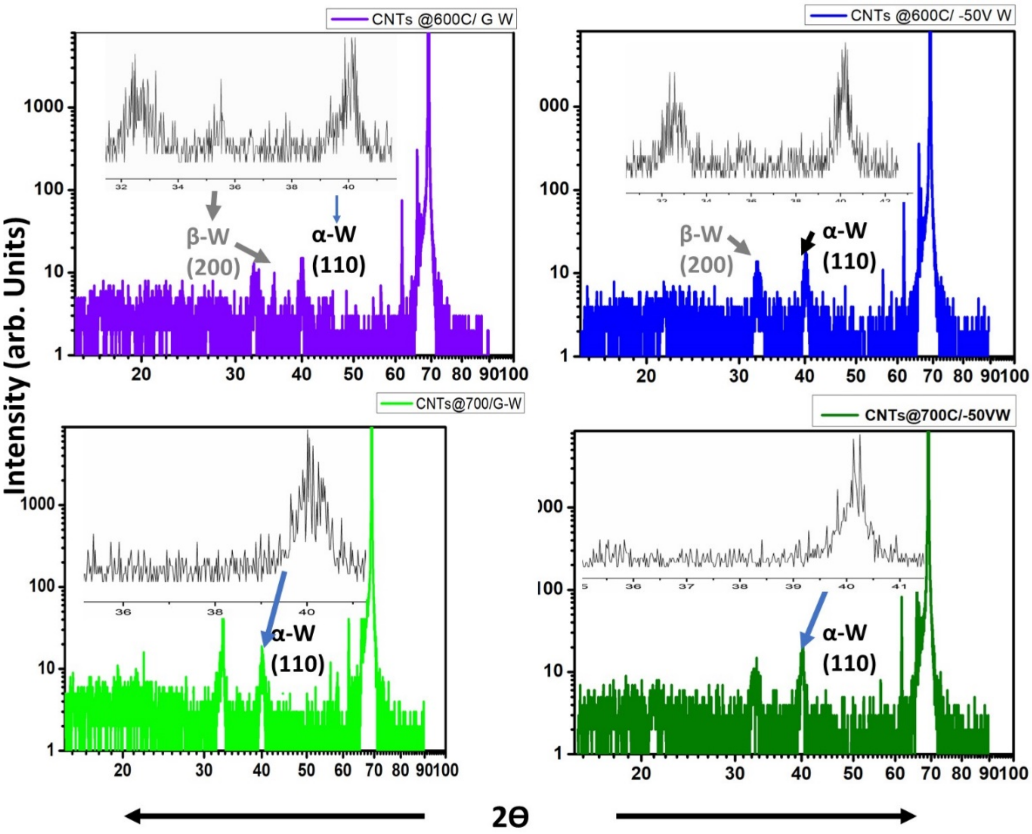

Figure 5. 10 XRD showing the presence of α-W and β-W in all the samples

	α-W	β-W
CNT forest grown at 600°C/W (G)	8.96	19.81
CNT forest grown at 600°C/W (B)	17.33	9.01
CNT forest grown at 700°C/W (G)	11.33	-
CNT forest grown at 700°C/W (B)	12.11	-

Table 5. 3 Grain size calculated using Scherrer formula

For analysing chemical and compositional state of the sample XPS characterization was performed. A Shirley background and Doniach-*Sunjic* line shapes were used to fit all the spectra from XPS. The XPS spectra of W4f was taken. For W4f, as shown in figure

5.11(table A1.17), first doublet feature is shown for all the samples. Peak appearing ~ (30.9 ± 0.2) eV and ~ (33.04 ±0.2) eV is associated with $W4f_{7/2}$ and $W4f_{5/2}$ metallic tungsten respectively. Deconvolution of W4f core level spectra indicates the presence of W^{2+}, W^{5+} and W^{6+} oxidation state. For all the spectra $W4f_{7/2}$ and $W4f_{5/2}$ appearing at ca. (32 -32.5) eV, (34.9 35.4) eV and (35.6 - 35.9) eV were corresponding to the above-mentioned states of W, respectively [5,16]. W^{3+} state has also been observed in 100nmWO_x(G)/CNTs@600C. Deposition of W on CNTs are producing more oxygen deficient sites as compared to W film on bare silicon substate.

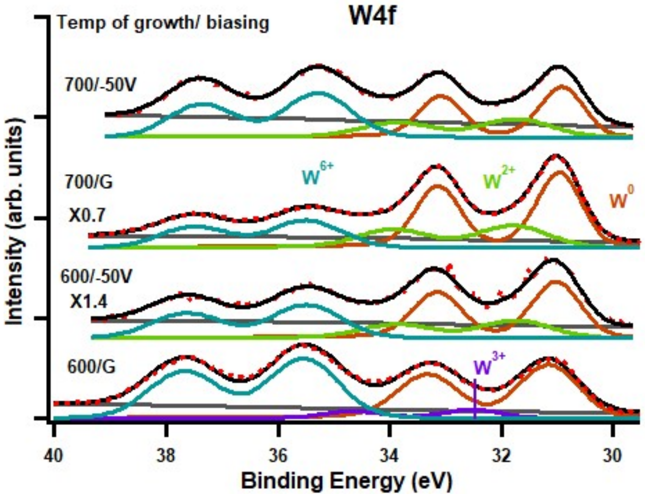

Figure 5. 11: XPS spectra for W4f of for the hybrid material of W-CNT forest.

We calculated the thickness of the oxide film for the samples after air exposure, using the formula mentioned above. For 100nmWO_x(G)/CNTs@600C the thickness was calculated to be 18.12 Å, and similarly for 100nmWO_x(B)/CNTs@600C it was 12.95 Å, on 100nmWO_x(G)/CNTs@700C it was calculated to be 9.51 Å, and for 100nmWO_x(B)/CNTs@700C it was 3.09 Å.

UPS He II (40.8 eV) photon energy was used to measure the valance band, figure 5.12. From the spectra it was observed that all the spectra have a peak in the range of (5.1 - 7.6) eV, indicating W5d-O2p hybridization. Presence of peak at 10 eV is usually assigned to hydroxyl group.

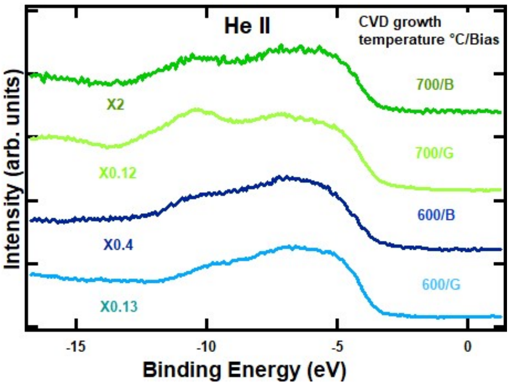

Figure 5. 12 UPS He II (hv = 40.8 eV) valance band spectra for the W-CNTs hybrid samples

We deposited 100 nm of W on various CNTs forests grown at 600 °C and 700 °C on SiO_2/Si(100). It was observed that deposition of W is not affected by the substrate biasing, but the density of the forest can play an important role in the coating thickness. When deposited on CNTs α-W is present in all the samples but β-W is only found on denser forest. Chemical analysis by XPS showed the presence of different states of tungsten oxide along with metallic tungsten.

5.2.1 500 nm of W deposited on short CNTs (~1 μm)

In section 5.2 we discussed the hybrid material comprising of 100 nm of W on CNTs on SiO_2/Si (100) substrate. The length of the CNTs reported in previous section were ranging from 6 – 12 μm. In this section the length of the CNTs used to deposit W is ~1 - 2 μm on Al_2O_3/Si(100) substrate as already discussed in chapter 3, and thickness of W was increased from 100 nm to 500 nm. SEM and XPS analysis were done to check the morphology and chemical composition of the hybrid [13].

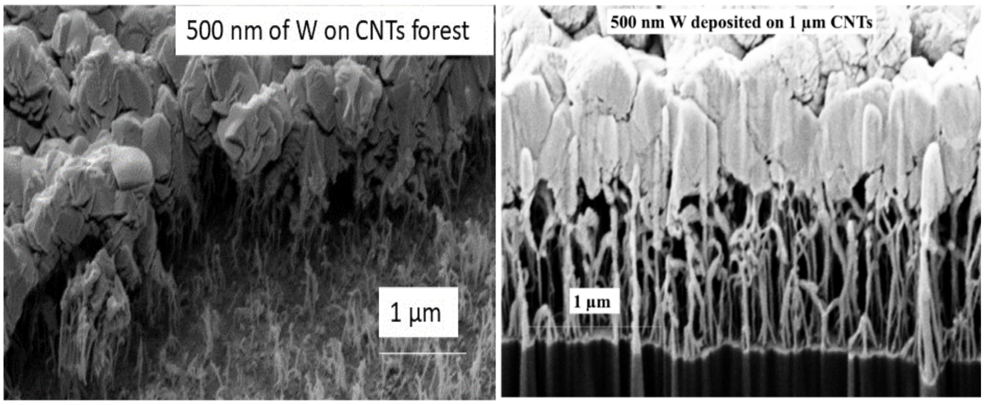

Figure 5. 13: SEM images showing HM9 (left), showing that W covered CNTs, but FIB (right) gave the insight that most of the deposition is on top of CNTs and the core of the forest does not receive W

Figure 5.13 shows the SEM and FIB images of the MWCNT forest after 500 nm W coating. SEM image referring to figure 5.9 reflects uniform deposition around the CNTs when deposited 100 nm of W. The density of the forest calculated for image 5.13 (right) was 7474 CNTs/µm^2. This density is 17 times more than what we have calculated for CNTs on SiO_2/Si substrate. When deposited with 500 nm of W using the same sputtering conditions as used in section 5.2, it was observed that W was heavily coated on top of the forest instead of penetrating into the forest. CNTs forest preserves its orientation and surface area, but around the W/CNTs junctions, cluster formation is observed. Because of this aggregation, W atoms instead of penetrating into the forest, they make a film on upper part of the forest. To observe the morphology and the coating infiltration depth within the CNTs forest, we performed FIB. Due to changing the thickness of the W film coating, uniformity and the penetration depth changed was seen in SEM/FIB images (not shown). The coating thickness reduced within the forest. The W film is concentrated on top of the forest, indicating a low diffusion of W inside the CNTs forest, which was also visible with FIB images [17].

The XPS spectra of W4f core level is shown in figure 5.14 and table A1.18. It can be noted that four components are present, after deconvolution. Main doublet peak at W4f$_{7/2}$ and W4f$_{5/2}$ at 30.9 eV and 33 eV refers to W^0, other contributing doublets are W^{2+}, W^{5+} and W^{6+} at peak position 31.8, 34.7 and 35.5 eV respectively [5,16].

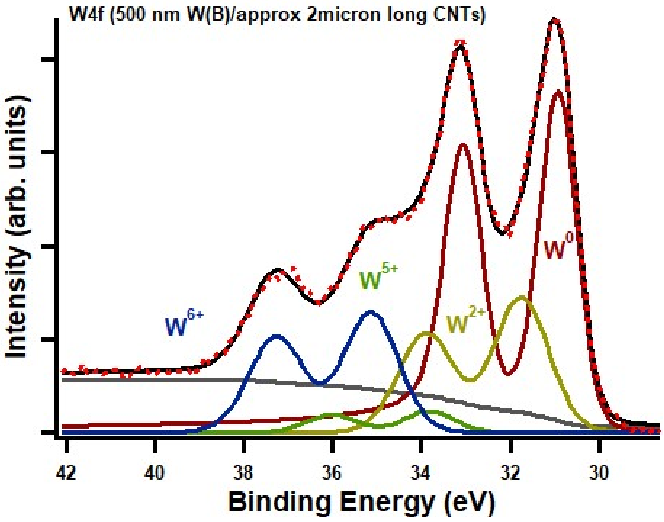

Figure 5. 14: XPS high resolution spectra for W4f

From the data discussed in section 5.2.1, it is shown that after air exposure the W film oxidized. The thickness of oxide layer was calculated using equation 1 from chapter 4, gave us 8 Å. This thickness is approximately 10 orders of magnitude more than the plain W film. The shape and size of W particles on CNTs vary with the thickness of the film. With 100 nm coating of W on CNTs, W covered the surface of the CNTs and was also able to penetrate the forest to reach the surface of the substrate. With the increased thickness of the film, W coating tends to form a roof on top of the forest. The penetration of W into the forest is an inverse relation with the density of the forest. If the length of the forest is in microns and is dense, the chance of aggregating W at CNTs junction favours the roof formation more than that of a shorter length forest and with reduced density of the CNTs, i.e., in nanometres. In the latter case, it proceeds to form a W-CNT matrix.

In addition, we deposited tungsten on CNTs by varying the sputtering parameters, like, power, substrate temperature and step wise deposition (100 nm- stop (recover pressure)-100nm), to avoid agglomeration. But in all the cases we acquired the same results, i.e., top of CNT forest covered with agglomerated W particles.

5.3 W deposition on CNTs via cluster source

The hybrid sample was prepared by supersonic cluster source for W deposition on CNT forest, already discussed in chapter 2 and 4 on CNTs. From the SEM image (figure 5.15), the tips of the CNTs are covered with clusters of W. These clusters have arranged in a way which resembles a beaded necklace.

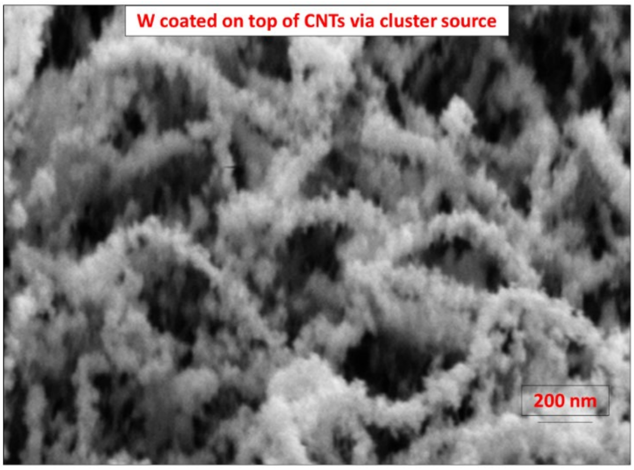

Figure 5. 15: SEM image of W nanoclusters arranged on CNTs, like beaded string

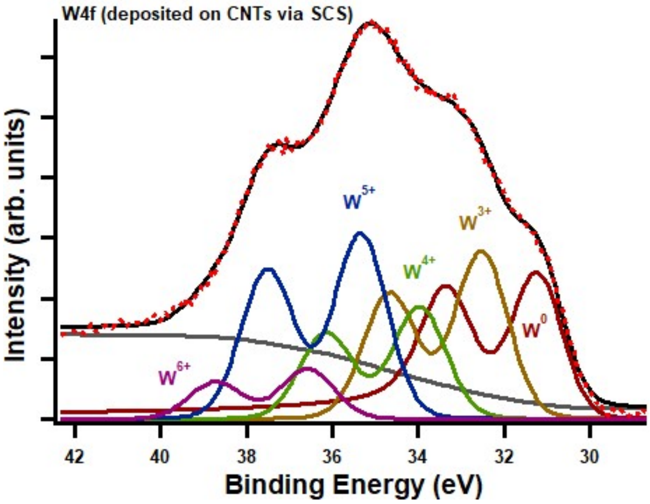

Figure 5. 16: in-situ XPS spectrum for W4f

In-situ XPS measurements were done to analyse the chemical state of the sample. To identify different states of W, deconvolution of W4f region is shown in figure 5.16 and table A1.19. W4f peak area was defined by Shirley type background subtraction, across the BE range. The spectrum for W4f was fitted with Voigt (GL convolution) line shape. It is observed that the peak position of W^0 is shifted towards higher BE as compared to already reported in previous section. This increase may be because of the grain size of the nanoclusters deposited on the CNTs. As grain size may affect plasmonic effect, hence resulting in a very slight shift in BE, and peak broadening. W^0 doublet is at 31.40 eV ($W4f_{7/2}$) and 33.5 eV ($W4f_{5/2}$), W^{3+} doublet is present at peak position 32.5 eV ($W4f_{7/2}$) and 34.6 eV ($W4f_{5/2}$). Moreover, W^{4+}, W^{5+}, and W^{6+} peaks were observed at 34 eV, 35.3 eV, and 35.6 eV respectively [18–20].

The VB spectrum of the sample is measured using He II radiation and is reported in Figure 5. 17. The energy region between 3-12 eV is governed by the presence of different characteristics of the O2p-W5d hybridization [21,22]. The π band appears ~ 4.5 eV. It is usually derived from the O2p p-DOS and is very sensitive to the O contents [21,22]. The feature shown at 7 eV is generated by the W5d-O2p σ bond. At around 9 eV a visible small feature can be attributed to the O2p-W6s bond [21,23,24].

The hybrid prepared in section 5.3 is different from the previously discussed in section 5.1 and 5.2, as here we do not form a matrix of CNs/CNTs and W, or thick coating of W covering the forest, instead the hybrid consists of W nano clusters covering CNTs forest like snowflakes covering the trees.

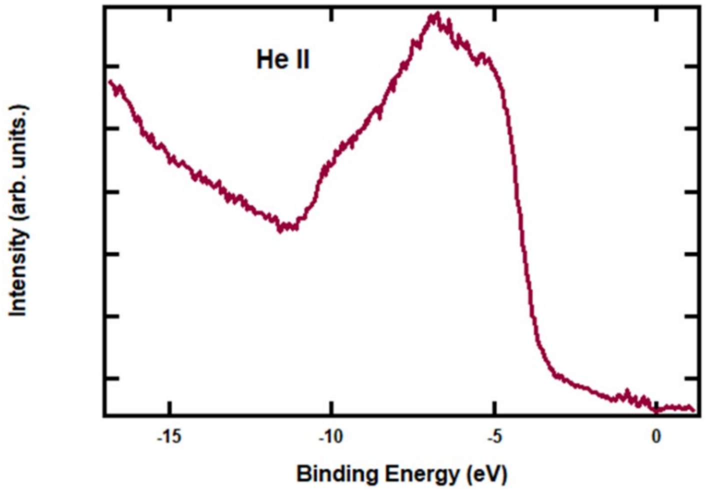

Figure 5. 17 He II (hv= 40.8 eV) spectrum for hybrid material comprising of CNTs and W nanoclusters

5.4 Summary

The W-C hybrids were grown using CNs/CNTs as template for W film via sputtering and W nanoclusters via SCS. The structural morphologies changed with the thickness of W coating. Also, when the procedure was changed for depositing W, W grains were different in shape and sizes and the surface coverage was different.

5.5 Reference

[1] G.V. Krishnamurthy, M. Chirumamilla, S.S. Rout, K.P. Furlan, T. Krekeler, M. Ritter, H.W. Becker, A.Y. Petrov, M. Eich, M. Störmer, Structural degradation of tungsten sandwiched in hafnia layers determined by in-situ XRD up to 1520 °C, Sci Rep 11 (2021). https://doi.org/10.1038/s41598-021-82821-0.

[2] B. Girault, P. Villain, E. Le Bourhis, P. Goudeau, P.-O. Renault, X-ray diffraction analysis of the structure and residual stresses of W/Cu multilayers, 2006. https://doi.org/10.1016/j.surfcoat.2006.08.034.

[3] I. Djerdj, A.M. Tonejc, A. Tonejc, N. Radić, XRD line profile analysis of tungsten thin films, in: Vacuum, 2005: pp. 151–158. https://doi.org/10.1016/j.vacuum.2005.08.017.

[4] M. Wilken, E. Ciftyürek, S. Cwik, L. Mai, B. Mallick, D. Rogalla, K. Schierbaum, A. Devi, CVD Grown Tungsten Oxide for Low Temperature Hydrogen Sensing: Tuning Surface Characteristics via Materials Processing for Sensing Applications, Small 19 (2023). https://doi.org/10.1002/smll.202204636.

[5] W. Lisowski, A.H.J. van den Berg, G.A.M. Kip, L.J. Hanekamp, Characterization of tungsten tips for STM by SEM/AES/XPS, Fresenius J Anal Chem 341 (1991) 196–199. https://doi.org/10.1007/BF00321548.

[6] A. Katrib, V. Logie, N. Saurel, P. Wehrer, L. Hilaire, G. Maire, Surface electronic structure and isomerization reactions of alkanes on some transition metal oxides, 1997.

[7] K. Mašek, P. Blumentrit, J. Beran, T. Skála, I. Píš, J. Libra, V. Matolín, Pt-doped tungsten oxide surface: Photoemission and RHEED study, in: Surface and Interface Analysis, 2010: pp. 540–544. https://doi.org/10.1002/sia.3362.

[8] S. Santucci, C. Cantalini, M. Crivellari, L. Lozzi, L. Ottaviano, M. Passacantando, X-ray photoemission spectroscopy and scanning tunneling spectroscopy study on the thermal stability of WO_3 thin films, J. Vac. Sci. Technol. A 18 (2000).

[9] K. Sardar, S. Thakur, S. Maiti, N. Besra, P. Bairi, K. Chanda, G. Majumdar, K.K. Chattopadhyay, Amalgamation of MnWO4nanorods with amorphous carbon nanotubes for highly stabilized energy efficient supercapacitor electrodes, Dalton Transactions 50 (2021) 5327–5341. https://doi.org/10.1039/d1dt00267h.

[10] R. Ghasempour, A.I. Zad, Hybrid multiwalled carbon nanotubes and trioxide tungsten nanoparticles for hydrogen gas sensing, J Phys D Appl Phys 42 (2009). https://doi.org/10.1088/0022-3727/42/16/165105.

[11] M.R. Alexander, G.E. Thompson, X. Zhou, G. Beamson, N. Fairley, Quantification of oxide film thickness at the surface of aluminium using XPS, in: Surface and Interface Analysis, 2002: pp. 485–489. https://doi.org/10.1002/sia.1344.

[12] S. Tanuma, C.J. Powell, D.R. Penn, Calculations of electron inelastic mean free paths. V. Data for 14 organic compounds over the 50–2000 eV range, Surface and Interface Analysis 21 (1994) 165–176. https://doi.org/10.1002/sia.740210302.

[13] J.F. Lin, O. Pitkänen, J. Mäklin, R. Puskas, A. Kukovecz, A. Dombovari, G. Toth, K. Kordas, Synthesis of tungsten carbide and tungsten disulfide on vertically aligned multi-walled carbon nanotube forests and their application as non-Pt electrocatalysts for the hydrogen evolution reaction, J Mater Chem A Mater 3 (2015) 14609–14616. https://doi.org/10.1039/c5ta02908b.

[14] N.V. Pulagara, I. Lahiri, Carbon nanotube-tungsten nanowire hierarchical structure for augmented field emission performance, Nanotechnology 33 (2022). https://doi.org/10.1088/1361-6528/ac659f.

[15] J.-S. Lee, J. Cho, C.-Y. You, Growth and characterization of α and β -phase tungsten films on various substrates, Journal of Vacuum Science & Technology A: Vacuum, Surfaces, and Films 34 (2016). https://doi.org/10.1116/1.4936261.

[16] C.B. Rodella, D.H. Barrett, S.F. Moya, S.J.A. Figueroa, M.T.B. Pimenta, A.A.S. Curvelo, V. Teixeira Da Silva, Physical and chemical studies of tungsten carbide catalysts: Effects of Ni promotion and sulphonated carbon, RSC Adv 5 (2015) 23874–23885. https://doi.org/10.1039/c5ra03252k.

[17] A.M. Gheitaghy, R.H. Poelma, L. Sacco, S. Vollebregt, G.Q. Zhang, Vertically-aligned multi-walled carbon nano tube pillars with various diameters under compression: Pristine and nbtin coated, Nanomaterials 10 (2020) 1–17. https://doi.org/10.3390/nano10061189.

[18] S.B.X.Y. Zhang, Q. Pessemesse, L. Lätsch, K.M. Engel, W.J. Stark, A. Van Bavel, A.D. Horton, P.-A. Payard, C. Copéret, Supplementary Information Role and Dynamics of Transition Metal Carbides in Methane Coupling, 2023. https://doi.org/10.26434/chemrxiv-2022-0q8rj.

[19] C. Liu, Y. Wen, L. Lin, H. Zhang, X. Li, S. Zhang, Facile in-situ formation of high efficiency nanocarbon supported tungsten carbide nanocatalysts for hydrogen evolution reaction, Int J Hydrogen Energy 43 (2018) 15650–15658. https://doi.org/10.1016/j.ijhydene.2018.06.087.

[20] S. Jeon, K. Yong, Synthesis and characterization of tungsten oxide nanorods from chemical vapor deposition-grown tungsten film by low-temperature thermal annealing, J Mater Res 23 (2008) 1320–1326. https://doi.org/10.1557/jmr.2008.0158.

[21] A. Braun, S. Erat, X. Zhang, Q. Chen, T.W. Huang, F. Aksoy, R. Löhnert, Z. Liu, S.S. Mao, T. Graule, Surface and bulk oxygen vacancy defect states near the Fermi level in 125 nm $WO_{3-\delta}/TiO_2$ (110) films: A resonant valence band photoemission spectroscopy study, Journal of Physical Chemistry C 115 (2011) 16411–16417. https://doi.org/10.1021/jp202375h.

[22] R.D. Bringans, H. Hochst, H.R. Shanks~, Defect states in WO, studied with photoelectron spectroscopy, Phys Rev B 24 (1981). https://doi.org/Phys. Rev. B, 24 (1981), pp. 3481-3489, 10.1103/PhysRevB.24.3481.

[23] E. Papalazarou, M. Gatti, M. Marsi, V. Brouet, F. Iori, L. Reining, E. Annese, I. Vobornik, F. Offi, A. Fondacaro, S. Huotari, P. Lacovig, O. Tjernberg, N.B. Brookes, M. Sacchi, P. Metcalf, G. Panaccione, Valence-band electronic structure of V_2O_3: Identification of v and O bands, Phys Rev B Condens Matter Mater Phys 80 (2009). https://doi.org/10.1103/PhysRevB.80.155115.

[24] A. D’elia, C. Cepek, M. De Simone, S. Macis, B. Belec, M. Fanetti, P. Piseri, A. Marcelli, M. Coreno, Interplay among work function, electronic structure and stoichiometry in nanostructured VO: X films, Physical Chemistry Chemical Physics 22 (2020) 6282–6290. https://doi.org/10.1039/d0cp00216j.

Chapter 6

Hybrid Materials as EtOH Gas Sensors

This chapter presents the electrical response to EtOH vapors of three significant samples described in the previous chapter, for their possible application as chemiresistors. The sample's electrical resistance variation was monitored during exposure in UHV to EtOH vapors. The results obtained have been tested several times to check the reproducibility of our findings and are compared to that of two reference samples: a CNT forest (from now named as CNT) and a continuous 100 nm film of WO_x (from now named as WO_x) deposited by DCMS on a Si(100) support.

The novel materials synthetized in this thesis tested as possible chemiresistors to EtOH are:

- a nanostructured WO_x film deposited via SCBD on a Si(100) support (from now named as NS-WO_x) (see chap. 4.3);
- a nanostructured WO_x film deposited via SCBD on a CNT forest (from now named as NS-WO_x/CNT) (see chap. 5.3).
- a CNT forest coated with an almost continuous WO_x film 25 nm thick deposited via DCMS (from now named as WO_x/CNT).

In this chapter we first describe method used for gas sensing, and then we will present the results of the samples listed above.

Gas sensing mechanism involves the adsorption of molecules of gas on the surface of the sensing material, resulting in the change in electrical signal. In literature there are different models used to explain the working principle of a chemical gas sensor depending on the nature of the interaction between the gas and the sensor. The most common models are (i). physical adsorption/desorption model (weak interaction between gas and sensing material), (ii). chemical adsorption/desorption model (strong gas-sensor interaction). A particular case of the chemical adsorption/desorption is the oxygen model invoked to explain the sensing of oxidizing and reducing gases on a semiconductor [1].

It is known that the response strongly depends on the operating temperature of the sensor [2].

As materials for sensor fabrication, semiconductors are investigated. In particular, it is known that in n-type material the majority charge carriers are electron, whereas in p-type holes are the majority charge carriers. These charge carriers, on interacting with the gas, will change the resistance of the sensing material (chemi-resistive method), depending on the type of gas (reducing or oxidising).

When the charge carriers transfer occurs, due to the adsorption of gas molecules on the material, band bending takes place. In the figure 6.1, band bending phenomena for p-type and n-type semiconducting materials are shown when exposed to oxygen. After the exposure to oxygen, in p-type material electrons are extracted as a form of oxygen ions on the surface of the material, resulting in accumulation of holes on the surface, hence increasing conductivity. Whereas in the case of n-type materials a depletion layer is formed on the surface therefore decreasing conductivity [3].

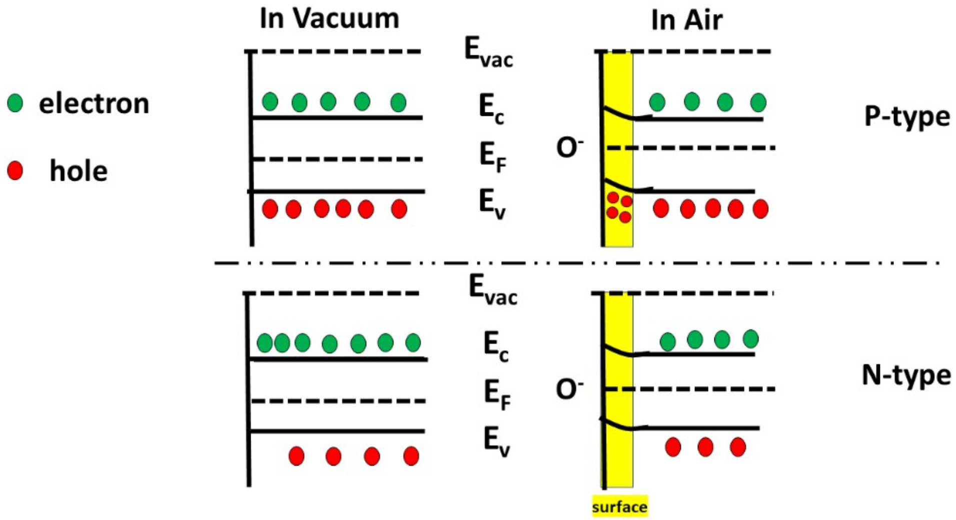

Figure 6. 1 P-type (above) and N-type (below) semiconducting material on adsorption of oxygen in which EVAC, EC, EF, EV represents the energies of vacuum level, conduction band, Fermi level and valance band.

Target gases are categorised as reducing and oxidizing. When the molecules of the gas interact with the sensor material, majority charge carries vary the resistance of the gas sensor based on the type of gas being targeted. For an n-type sensor material, exposed to oxidizing gas, the resistance will increase, which is attributed to the formation of electron depletion layer. In case of p-type material if the same gas is targeted, the resistance will decrease as shown in figure 6.1 [4].

When the n-type gas sensor is exposed to the reducing gas, the reaction between the adsorbed gas molecules and the active oxygen sites on the surface takes place. This results in the release of free electron in the bulk, resulting in the decrease of resistance. In case of p-type gas sensor, when exposed to the same gas, the resistance will increase [5].

6.1 Methods: Ethanol Exposure, Resistance Measurement

The sample's electrical resistance has been measured at RT in UHV conditions (base pressure: 2×10^{-9} mbar) using a conventional multimeter connected to the samples through the sample holder (see chap. 2.4). The electric contact has been done through two tantalum foils in direct contact with two sample's borders (contact area: about $1 \times 5 \text{mm}^2$). For all samples, before EtOH dosing, the stability of the resistance was measured, giving values in the range of ohm to Mohm.

EtOH was dosed at pressure of 2×10^{-5} mbar (corresponding to about 20 ppb in 1 atmosphere pressure) through a leak valve from a home-made stainless steel UHV cylinder. Typical dosing time were of about 40-60 minutes, corresponding to a total dose of about **$5\text{-}7 \times 10^4$ L**. EtOH cleanness was achieved via several cycles of pumping while the cylinder was frozen using liquid Nitrogen. EtOH cleanness was monitored after the cleaning procedure and during all the exposures using a residual gas analyzer. We monitored as a function of time the single ionized molecular ion of EtOH, nitrogen, water, and oxygen. To reach the required EtOH partial pressure the cylinder was annealed at about 100 °C during dosing.

Because of the low EtOH sticking coefficient and the consequently low pumping efficiency, the pressure recovery time was long. It took approximately one hour and 30 minutes to reach low 10^{-7} mbar after stopping the flow of EtOH. Therefore, the material recovering time was not possible to measure and it is not significant in all our findings.

The electrical resistance relative response as a function of dose, the sensitivity S, is defined as:

$$S = [(\Delta R)/R_o] \times 100 \qquad \text{Equation 6. 1}$$

where $\Delta R = R_d - R_o$, R_d is the resistance during dosing and R_o is the initial resistance, i.e., before dosing [6].

To understand if any chemical changes are detectable after EtOH uptake, we performed in-situ XPS photoemission before and after EtOH exposure, but no changes in the C 1s, O 1s core levels and in the UPS spectra were visible on all samples. We note that we were able to perform photoemission only after the pressure in the chamber was almost completely recovered (at least in the range 10^{-7}-10^{-8} mbar), so if the molecules are physiosorbed only during exposure, due to the low sticking EtOH coefficient, no changes are expected to be observed. Only in-operando measurements done on a high pressure XPS equipment may be able to revel any chemical changes responsible of the resistance changing due to EtOH adsorption. The weak physisorption is in contrast with the oxygen model.

We finally note that, by assuming the response $\Delta R/R_0$ is proportional to the number of molecules adsorbed on the surface, and since the partial pressure is proportional to the dose of the gas injected in the chamber, it is possible to relate the resistance relative response versus dose to the adsorption isotherms on the different surfaces investigated, as already done in the past [7].

6.2 Reference samples: Carbon nanotubes forest and WO_x film on Si(100) via DCMS

Fig 6.2, top shows the resistance relative response versus dosing time of a CNTs forest (red) and that of a continuous WO_x film 100 nm thick deposited at RT via DCMS in oxygen environment (oxygen pressure: 3 sccm) (black). The initial resistance R_0 of the CNTs film was 23.9 ± 0.3 kΩ, while that of the WO_x film was (1.3 ± 0.05) kΩ. For both samples, EtOH was dosed at the pressure of $2\text{x}10^{-5}$ mbar for 40 minutes, obtaining a total dose of $4.8\text{x}10^{4}$ L. The SEM image of the CNTs forest is shown in the figure 6.2 (bottom), while the WO_x film is not shown because it was featureless in SEM. The detailed description of the CNTs synthesis and structure is given in chapter 3.2, while that of the WO_x film in chapter. 4.2. The resistance measurements have been done at RT, in both cases the dose has been stopped after 40 minutes, as indicated by the arrow in the figure 6.2 (top). It is clear that the response of the CNT forest increased as a function of total dose, without reaching saturation, and it stopped and started to decrease as soon as EtOH is stopped.

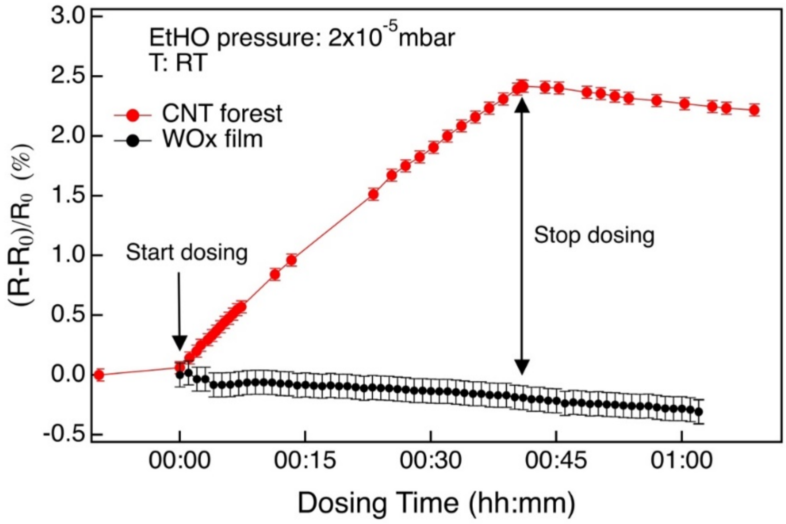

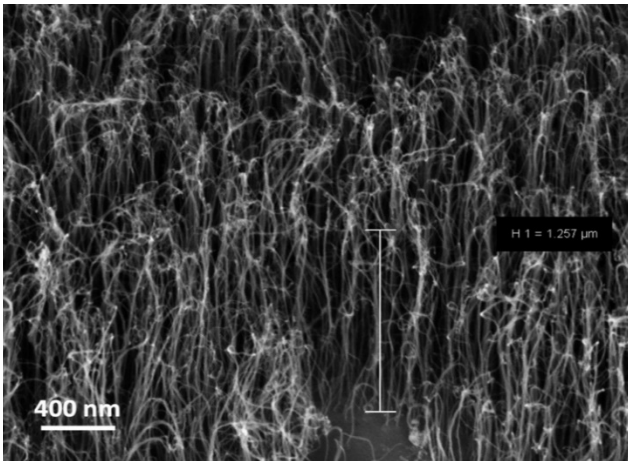

Figure 6. 2 (top) Sensitivity of the CNTs (red) and WO_x film (black) to EtOH when dosed at RT, (bottom) SEM image of the CNTs used for sensing

Beside the conditions of exposure were not conventional because we operated in UHV, we can compare these results with those obtained in conventional chemiresistors, the behavior observed in the CNT sample is in line with the literature results, with the CNTs behaving as a p-type semiconductor when exposed to a reducing gas like EtOH [8]. After 40 min of exposure, corresponding to a total dose of 4.8×10^4 L, the sample showed about 2.5 % sensitivity. This result may be compared to the MWCNTs have been used as EtOH gas sensors at different operating temperatures, gas concentration and atmosphere. Chun-Shin reported 0.03% sensitivity towards chamber pressure of EtOH vapours at 50 mTorr at RT [9]. Others have exposed the MWCNTs sensors to a comparatively higher concentration, like Wang et al. used layer by layer self-assembled method and used 30 kppm concentration of EtOH vapours at RT in a sealed flask set up. They reported 4.1 % sensitivity and 10 s response time [10,11]. In another work, Young and Lin used CVD method to synthesis VACNTs, exposed them to 800 ppm EtOH concentration at RT and observed 1.67 % sensitivity[11].

The electrical resistance response to EtOH of the WO_x film, instead, was not evident within our experimental conditions: only a slight decreasing of the resistance was seen, which continued also after the dosing was stopped, due to instability of our experimental apparatus, mostly due to the electric contacts. It is well known that **only crystalline WO_x** respond at RT, while defective samples need high working temperatures (≥300 °C) and show less sensitivity [12,13].

WO_x films grown at elevated temperature show response even at RT, due to increased crystallite size [14]. Whereas, WO_x gas sensors have shown optimistic results for sensing harmful volatile organic compounds (VOCs). The advantageous features of these sensors are their excellent response, sensitivity, and recovery. With all the advantages stated, there is still room for improvement in the field of gas sensing, as most of the metal oxide gas sensors including WO_x require high operating temperature (100 °C – 500 °C) and show poor selectivity amongst the same class of gases, like volatile organic compounds [15].

To understand if any chemical changes are detectable after EtOH uptake, we performed in-situ XPS photoemission before and after EtOH exposure, but no detectable changes in the C 1s, O 1s core levels and in the UPS, spectra were visible on both the WO_x film and the CNT forest. Reason already discussed in this section 6.1.

To confirm the reproducibility of our results, we performed several times the same experiment on the same sample. Fig. 6.3 shows the results obtained on the CNT forest discussed above with those obtained by exposing the same sample to EtOH in the same conditions for longer time. To be sure to complete reset the CNTs forest, we performed an annealing at about 250 °C before the exposure. The results are fully reproducible, and it seems that the CNTs forest does not reach the saturation after about 195 minutes (total dose: 2.3×10^5 L).

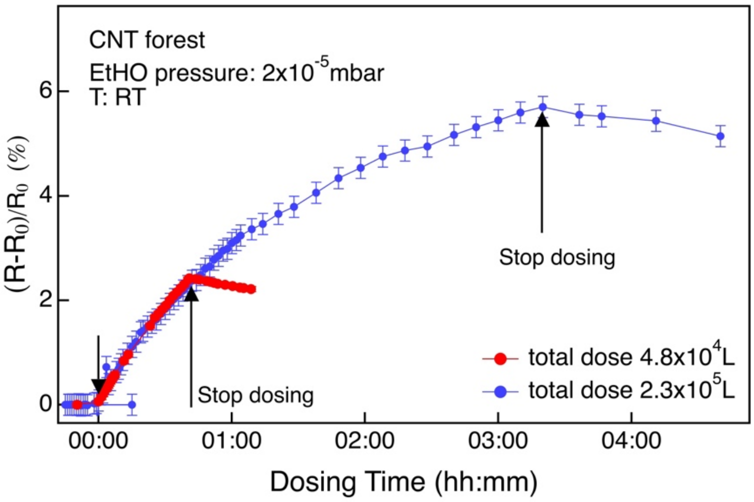

Figure 6. 3 Dosing CNTs with EtOH for 40 min (red) and for 195 min (blue) to get to the saturation, point in vacuum conditions at RT

The above results are used as references to test and compare the response of the novel materials discussed in the next paragraphs.

6.3 Effect of nano structuring: Nanostructured WO_x deposited via SCS

Figure 6.4 top shows the resistance relative response versus dosing time of a nanostructured WO_x film deposited via SCS, the SEM image of the sample is shown in Fig. 6.4, bottom. Also in this case, EtOH was dosed at the pressure of $2x10^{-5}$ mbar for 40 minutes, obtaining a total dose of $4.8x10^4$ L. The starting R_0 resistance of the sample was 0.15 MΩ. The structural and chemical characterization of this sample is found in chap. 4.3, figures 4.7 – 4.12. We recall that in this case the WO_x single NP's dimension are in the range of less than 1 nm, as revealed by TEM (fig. 4.8 and 4.9). The as deposited stoichiometry includes several W different oxidation states, but after air exposure the sample was completely oxidized, as revealed by in-situ and ex-situ XPS in figure 4.12. Despite the data is noisy, it is clear that in this case the resistance response reached a saturation after about 17 minutes and, even if the pressure recovering is slow as discussed before, the resistance recovery is faster than that in the case of CNTs, which may indicate that this material is a good candidate for chemi-resistor applications. In addition, the response, at the total dose of $4.8x10^4$ L, was about 5.5%, significantly higher than that found for CNT at the same dose, (about 2.5%).

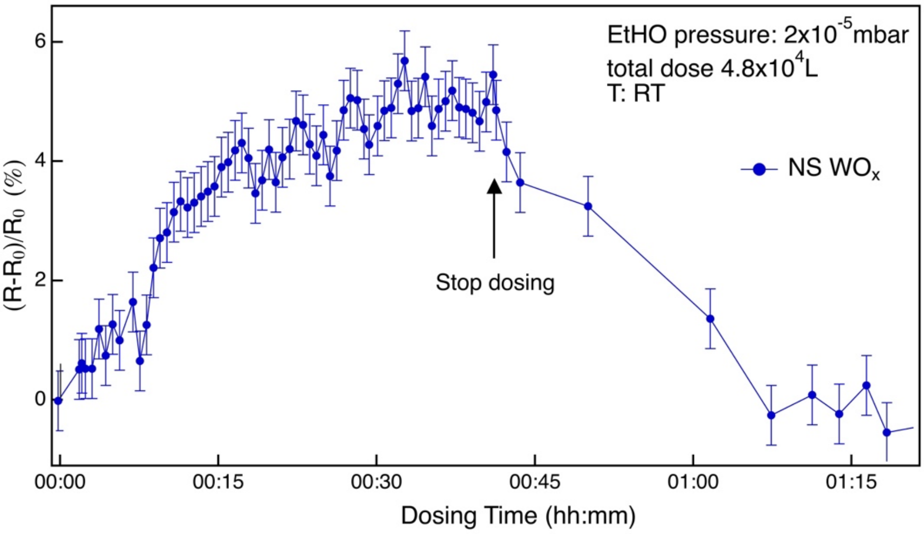

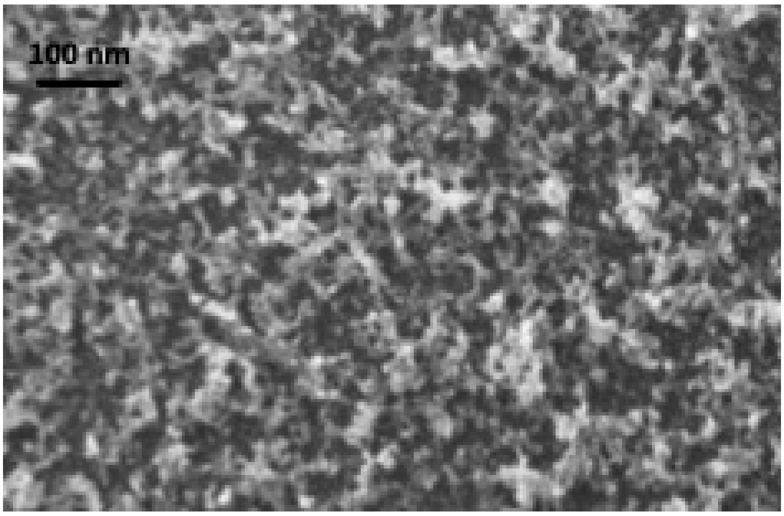

Figure 6. 4 (Top) Response of WO_x clusters deposited on Si(100) support via SCS at RT, when dosed with 20 ppb EtOH, (bottom) SEM image of the clusters decorated on Si(100) substrate

As in the case of CNTs, the resistance increased, indicating a p-type behavior. We recall that stoichiometric WO_3 thin film, functioning as a gas sensor, adhered to the intrinsic n-type property [14] and demand operating temperatures within the range of 300 °C – 350 °C. In contrast, when the material is non-stochiometric WO_3 (i.e., WO_{3-x}) it may exhibit a p-type behaviour within the temperature range RT (25 °C) - 200 °C, as here observed [16].

The surface morphology plays a very important role in gas sensing, in case of nanoclusters the availability of defective sites to adsorb gas molecules are readily available. The good response of our NS WO_x is due to the high density of defects and to the high porosity of the sample, which can be achieved only by using the particular synthesis techniques used here.

Also in this case, we performed *in-situ* photoemission before and after EtOH exposure did not show any difference, and only in-operando measurements done on a high pressure XPS equipment during exposure may be able to revel any changes due to EtOH adsorption.

To confirm that defects play and important role in the sample response to EtOH, we tested the same sample in the same exposure conditions after annealing at 280 °C for 10 minutes, as shown in figure 6.5.

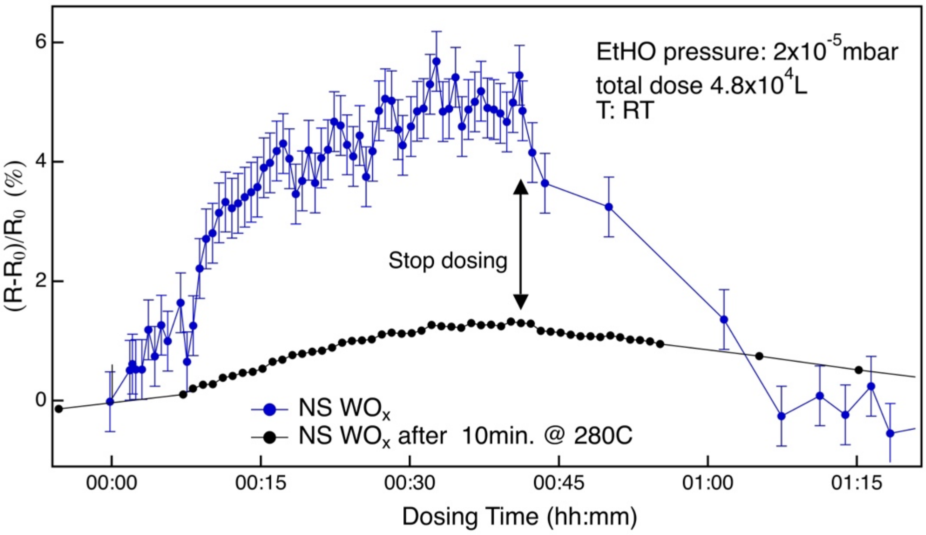

Figure 6. 5 EtOH dosing response at RT (blue) and after annealing (black) the sample at 280 °C for 10 min and then dosing the EtOH in the sample conditions.

Clearly, the response after 4.8 x 10^4 L total dose decreased from about 5.5% to 1.4%. In this case, thus defects play an important role, increasing gas sensitivity. The nanoclusters exhibit a larger surface to volume ratio. As a result of which they demonstrated higher reactivity and sensitivity to environmental changes. Furthermore, in the case of WO_x the surface is oxygen deficient, which can readily trap EtOH gas molecules. Because of these oxygen deficient sites, holes are the majority charge carrier, owing to the p-type nature of the device. Therefore, showing a good response at RT [16].

6.4 Hybrids: CNTs forest covered with WO_x films deposited via DCMS and SCS

Figure 6.6, top shows the resistance relative response versus dosing time of a CNTs forest covered with a 25 nm WO_x film deposited via DCMS (purple spectra, the empty dots spectrum is multiplied by 5) and a NS WO_x film deposited via SCS (green). The responses were compared to the NS WO_x film discussed in paragraph 6.3 (blue spectrum) and to the two reference responses: of the CNTs forest (red) and of the WO_x film deposited via DCMS (black), reported in paragraph 6.2. The SEM images of the hybrid samples are shown in Fig. 6.6, bottom and their complete morphological and chemical description is given in paragraph 5.2 and 5.3.

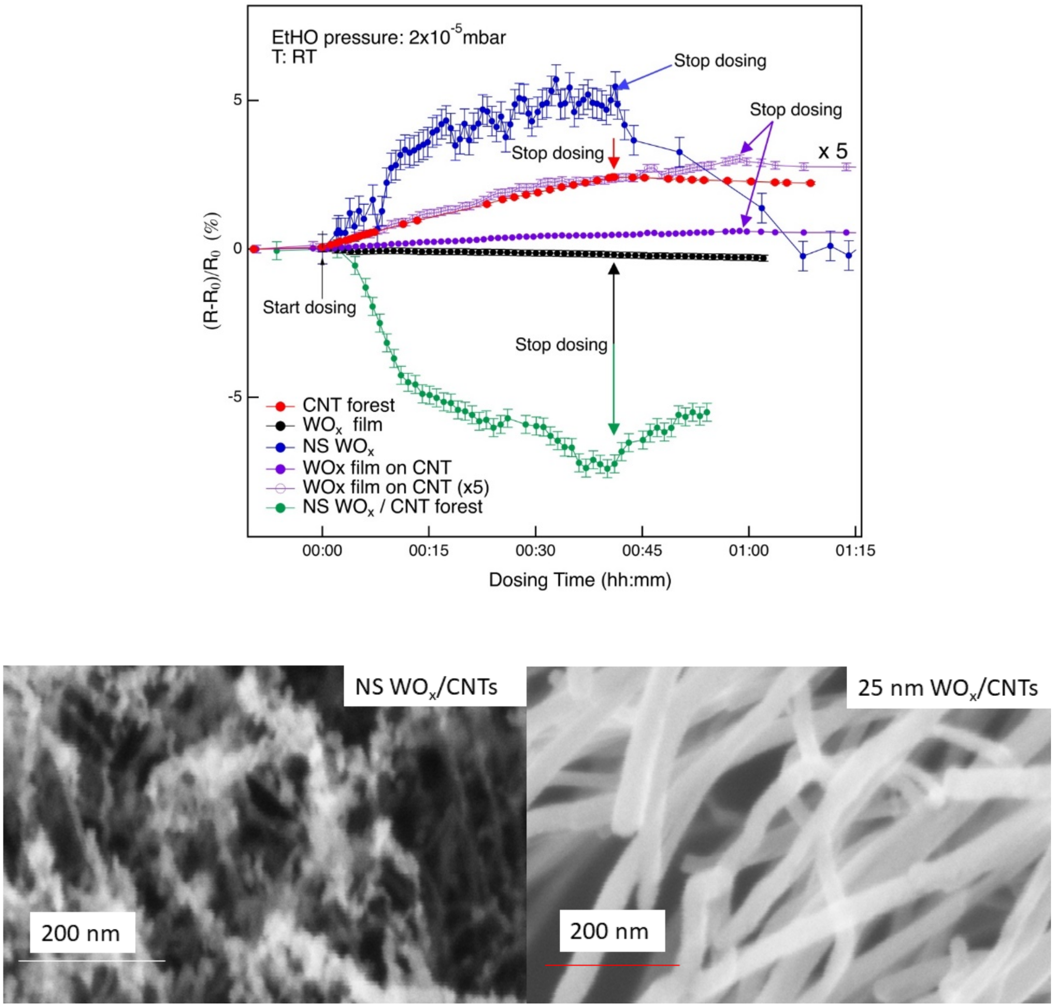

Figure 6. 6 (top) Sensitivity of the samples are shown when dosed with EtOH at RT in vacuum condition. (bottom) SEM images of the CNTs forest decorated with NS WO_x (left) and WO_x film (right).

Also in this case, EtOH was dosed at the pressure of $2x10^{-5}$ mbar, obtaining a total dose of $7.2x10^4$ L for the DCMS WO_x/CNT film and $4.8x10^4$ L for the NS-WO_x/CNT film deposited via SCS. The starting R_0 resistances of the two hybrid samples were 760 Ω for the former, from now called as WO_x/CNT, and 1.15 MΩ for the latter, from now called as NS-WO_x/CNT.

It is obvious that WO_x/CNT behaved as a p-type semiconductor, following a curve that is the same of the one observed for the bare CNTs forest, but with a significant lower response to EtOH: after a total dose of $4.8x10^4$ L (40 minutes exposure) the CNTs forest has the response of about 2.4%, while the hybrid WO_x/CNT only 0.47%, about 5 times lower. In this case it seems that, in the experimental conditions we explored, the response is due to the covered CNTs, suppressed by the WO_x film which may reduce the active sites, decreasing the sensitivity. The NS-WO_x/CNT, instead, is the one showing at the same dose the highest response, about -7.3%.Beside both the CNT and the NS-WO_x components behave as p-type semiconductors, it has to be noted that when are combined together into the hybrid, the new material shows a n-type behavior, which may be ascribed to a chemical bonding (charge transfer) between the WO_x nanoparticles and the CNTs. The possibility to obtain n-type behavior in CNTs is an important open issue in literature which has important technological implications for their use in many electronic applications. The main difficulty in getting reliable n-doped CNTs lies in the fact that these systems are not stable in air, and many strategies have been explored to overcame this problem [17,18]. The possible charge transfer between the highly reactive WO_x nanoparticles and the CNTs of this hybrid system, which is stable and persist also after many days of air exposure, could not be confirmed via photoemission, because the NS-WO_x thickness in this sample was higher than the surface sensitivity of the techniques here used (XPS and UPS), and further investigations are scheduled to disentangle this point.

All the samples that we have tested for EtOH gas sensing NS WO_x/CNT forest showed a very promising response. Unlike WO_3 gas sensor, which requires high operating temperature or like already reported as discussed above WO_x sensors requiring high concentration of gas for response, this HM showed response at RT and very low concentration of gas.

6.5 Reference

[1] H. Ji, W. Zeng, Y. Li, Gas sensing mechanisms of metal oxide semiconductors: A focus review, Nanoscale 11 (2019) 22664–22684. https://doi.org/10.1039/c9nr07699a.

[2] S.D. Lawaniya, S. Kumar, Y. Yu, H.G. Rubahn, Y.K. Mishra, K. Awasthi, Functional nanomaterials in flexible gas sensors: recent progress and future prospects, Mater Today Chem 29 (2023). https://doi.org/10.1016/j.mtchem.2023.101428.

[3] C. Wang, L. Yin, L. Zhang, D. Xiang, R. Gao, Metal oxide gas sensors: Sensitivity and influencing factors, Sensors 10 (2010) 2088–2106. https://doi.org/10.3390/s100302088.

[4] R.C. Pawar, J.W. Lee, V.B. Patil, C.S. Lee, Synthesis of multi-dimensional ZnO nanostructures in aqueous medium for the application of gas sensor, Sens Actuators B Chem 187 (2013) 323–330. https://doi.org/10.1016/j.snb.2012.11.100.

[5] M. Latino, G. Neri, chemoresistive metal oxide gas sensor: working principles and applications, 98 (2021) 41. https://doi.org/10.1478/AAPP.98S1A41.

[6] M. Righettoni, A. Tricoli, S. Gass, A. Schmid, A. Amann, S.E. Pratsinis, Breath acetone monitoring by portable Si:WO 3 gas sensors, Anal Chim Acta 738 (2012) 69–75. https://doi.org/10.1016/j.aca.2012.06.002.

[7] P.N. Mbuyisa, F. Rigoni, S. Nappini, E. Magnano, S. Pagliara, G. Drera, L. Sangaletti, A. Goldoni, M. Ndwandwe, C. Cepek, Fast-tracking of NH3 interaction with ZnO nanorods and C/ZnO hybrid nanostructures by operando spectroscopy, Appl Surf Sci 590 (2022) 153067. https://doi.org/10.1016/j.apsusc.2022.153067.

[8] Verma Gulshan, Gupta Ankur, Recent development in carbon nanotubes-based gas sensors, Journal Of materials nanoscience 9 (2022) 3–12.

[9] C. Yeh, Carbon Nanotubes Gas Sensor for Ethanol Detection, International Journal of Science and Engineering 2 (2012).

[10] K. Wang, D. Zhang, J. Tong, B. Xia, Ethanol gas sensor based on self-assembled multi-walled carbon nanotube film, Applied Mechanics and Materials 241–244 (2013) 881–884. https://doi.org/10.4028/www.scientific.net/AMM.241-244.881.

[11] S.J. Young, Z.D. Lin, Ethanol gas sensors based on multi-wall carbon nanotubes on oxidized Si substrate, Microsystem Technologies 24 (2018) 55–58. https://doi.org/10.1007/s00542-016-3154-2.

[12] G. Adilakshmi, A. Sivasankar Reddy, P. Sreedhara Reddy, C. Seshendra Reddy, Electron beam evaporated nanostructure WO3 films for gas sensor application, Mater Sci Eng B Solid State Mater Adv Technol 273 (2021). https://doi.org/10.1016/j.mseb.2021.115421.

[13] M. Ahsan, M.Z. Ahmad, T. Tesfamichael, J. Bell, P.K.D.V. Yarlagadda, Ethanol sensitivity of thermally evaporated nanostructured WO3 thin films doped and implanted with Fe, in:

Applied Mechanics and Materials, 2013: pp. 1938–1945. https://doi.org/10.4028/www.scientific.net/AMM.333-335.1938.

[14] T. Mpanza, C.L. Ndlangamandla, B.D. Ngom, S.S. Nkosi, T.P. Jili, C.T. Thethwayo, P.N. Biyela, N.G. Cebekhulu, P.S. Mkwae, S.A. Ogundipe, Tungsten oxide thin film for room temperature nitrogen dioxide gas sensing, MATEC Web of Conferences 374 (2023) 01003. https://doi.org/10.1051/matecconf/202337401003.

[15] A. Mirzaei, S.G. Leonardi, G. Neri, Detection of hazardous volatile organic compounds (VOCs) by metal oxide nanostructures-based gas sensors: A review, Ceram Int 42 (2016) 15119–15141. https://doi.org/10.1016/j.ceramint.2016.06.145.

[16] Y. Yao, M. Yin, J. Yan, S. (Frank) Liu, P-type sub-tungsten-oxide based urchin-like nanostructure for superior room temperature alcohol sensor, Appl Surf Sci 441 (2018) 277–284. https://doi.org/10.1016/j.apsusc.2018.02.004.

[17] S. Horike, Q. Wei, K. Akaike, K. Kirihara, M. Mukaida, Y. Koshiba, K. Ishida, Bicyclic-ring base doping induces n-type conduction in carbon nanotubes with outstanding thermal stability in air, Nat Commun 13 (2022). https://doi.org/10.1038/s41467-022-31179-6.

[18] L. Brownlie, J. Shapter, Advances in carbon nanotube n-type doping: Methods, analysis and applications, Carbon N Y 126 (2018) 257–270. https://doi.org/10.1016/j.carbon.2017.09.107.

Conclusions

The final aim of this thesis was the development of new Carbon-Tungsten nanostructured hybrid materials that potentially can be used in many applications, as, for example, first-wall material in fusion reactors [1], CO_2 reduction [2], H_2 production [3], chemiresistor to many hazardous and toxic gases, like CO, H_2, H_2S [4,5]. All the work has been performed in different laboratories of the IOM-CNR Institute, and it was partially funded by the energy company ENI.

The main purpose of these hybrid materials is to be used in the fusion reactor, but other applications include ethanol gas sensing.

After the correct setting of the CVD apparatus and process conditions, we produced many carbon nanostructures, including isolated SWCNTs, sp^2 dendritic 3-dimentional thin films, carbon nanofibers and CNTs (from low to high density aligned forests) with controlled length and density. We investigated many parameters that affect the CVD synthesis, like catalyst nature and thickness (chapter 3.1 and 3.2), process temperature (chapter 3.1 and 3.2.2), process duration time (chapter. 3.3.1), and process pressure (chapter 3.3.3). All samples were deeply characterized in morphology and stoichiometry (chapter 3). The above CNs were used as substrate to synthetize novel W nanostructures and hybrids produced by using conventional DCMS (chapter 4.1 and 4.2) and a supersonic cluster source, AMPHIRO (chapter 4.3).

Our results shows that the deposition of tungsten via DCMS allows to preserve the pristine morphology of the CNs used as substrate, slightly modifying the starting roughness and morphology (see chap. 5.1). In the case of CNT forest, depending on the tube density and thickness, tungsten can uniformly wet the tubes (CNTs density: lower than 436 Tubes/μm^2; W thickness: lower than 100 nm), or can form a non-uniform coating along the tubes, (tube density: higher than ~ 8000 Tubes/ μm^2; W thickness: higher than 200 nm), up to the formation of a W film on top of the CNTs carpet (chap. 5.2.1, fig.5.17). In all cases, the starting CNTs morphology was preserved, as observed by SEM, thus proving an effective method to obtain different hybrid C/W nanostructures exploiting the well-known carbon ability to form nanostructures. The use of the cluster source AMPHIRO allowed to obtain nanostructured WO_x films, whose building blocks were clusters of dimensions of less than 1nm (chap. 5.3). In-situ and ex-situ photoemission has shown that, by using the appropriate gas mixture environments during the cluster synthesis, the nano/sized WO_x clusters films present a variety of different oxidation state, not stable in conventional bulk systems (chap. 4.3, paper in preparation). The deposition of this material on CNTs carpet resembles a beaded necklace (chap. 5.3), where the CNTs are decorated by WO_x clusters, structures that, to our knowledge, has never observed in literature.

As preliminary work, we measured the electrical response to EtOH vapors of three significant hybrids for their possible use as chemiresistors, monitoring their electrical resistance variation during exposure in UHV to EtOH vapors (chap. 6.1). The results obtained have been tested several times to check the reproducibility of our findings and are compared to that of two reference samples: a CNT forest and a continuous 100 nm film of WO_x deposited by DCMS on a Si(100) support. The hybrids we choose were: a nanostructured WO_x film deposited via SCBD on a Si(100) support (NS-WO_x), a nanostructured WO_x film deposited via SCBD on a CNT forest (NS-WO_x/CNT) and a CNT forest coated with an almost continuous WO_x film 25 nm thick deposited via DCMS (WO_x/CNT). EtOH was dosed at pressure of $2x10^{-5}$ mbar (corresponding to about 20 ppb in 1 atmosphere pressure) in UHV environment. Our results indicate that the deposition of a continuous W film via DCMS suppresses the well- known ability of the CNTs to respond to EtOH as p-type material. Unlikely to WO_3, the highly defected and porous NS-WO_x film shows a response already at RT, with a higher sensitivity than the CNTs forest (no response has found in the reference continuous WO_x film at RT) and it behaves as p-type material, as already found in defected WO_3 films. The sample that showed the highest sensitivity was NS-WO_x/CNT. Beside both the CNT and the NS-WO_x components behave as p-type semiconductors, the new material shows a n-type behavior, which may be ascribed to a possible charge transfer between the WO_x nanoparticles and the CNTs. We note that the possibility to obtain n-type behavior in CNTs is an important open issue in literature which has important technological implications for their use in many electronic applications The possible charge transfer between the highly reactive WO_x nanoparticles and the CNTs of this hybrid system, which is stable and persist also after many days of air exposure, could not be confirmed via photoemission, because the NS-WO_X thickness in this sample was higher than the surface sensitivity of the techniques here used (XPS and UPS), and further investigations are scheduled to disentangle this point.

Last but not least, the most promising hybrids here synthesized are planned to be studied for hydrogen retention and will be exposed to the GyM linear reactor of ISTP-CNR (Milano) to be tested as first wall material in a fusion reactor.

Reference

[1] L.G. Carpen, T. Acsente, V. Sătulu, E. Matei, S. Vizireanu, B.I. Biță, G. Dinescu, Hybrid nanostructures obtained by transport and condensation of tungsten oxide vapours onto cnw templates, Nanomaterials 11 (2021). https://doi.org/10.3390/nano11040835.

[2] K. Zhao, X. Quan, Carbon-Based Materials for Electrochemical Reduction of CO2 to C2+ Oxygenates: Recent Progress and Remaining Challenges, ACS Catal 11 (2021) 2076–2097. https://doi.org/10.1021/acscatal.0c04714.

[3] G.T.M. Kadja, M. Mualliful Ilmi, S. Mardiana, M. Khalil, F. Sagita, N.T.U. Culsum, A.T.N. Fajar, Recent advances of carbon nanotubes as electrocatalyst for in-situ hydrogen production and CO2 conversion to fuels, Results Chem 6 (2023). https://doi.org/10.1016/j.rechem.2023.101037.

[4] S. Yang, G. Lei, H. Xu, Z. Lan, Z. Wang, H. Gu, Metal oxide-based heterojunctions for gas sensors: A review, Nanomaterials 11 (2021). https://doi.org/10.3390/nano11041026.

[5] S. Wang, Y. Kang, L. Wang, H. Zhang, Y. Wang, Y. Wang, Organic/inorganic hybrid sensors: A review, Sens Actuators B Chem 182 (2013) 467–481. https://doi.org/10.1016/j.snb.2013.03.042.

Appendix

Here we have presented tables of important parameters used to fit XPS data in the thesis.

As grown (Ni2p)			
Name	Ni^0	Ni^{3+}	$Ni(OH)_2$
Position (eV)	852.9	854.6	856.2
Γ	1.04	1.04	1.04
Gauss	0.94	1.4	1.4
asymmetry	0.1	0	0
After annealing at 400 °C			
Name	Ni^0	satellite	
Position (eV)	852.73	859.06	
Γ	1.04	1.04	
Gauss	0.8	1.4	
asymmetry	0.1	0	

A1. 1: Parameters used to fit Ni2p spectra of 1.5 nm Ni deposited on SiO_2/Si substrate, as grown, and annealed at 400 °C

As grown (O1s)			
Name	Ni^{3+}	OH	O_{ad}
Position (eV)	530.89	531.97	533.2
Γ	0.18	0.18	0.18
Gauss	1.4	1.4	1.4
asymmetry	0	0	0
After annealing at 400 °C			
Name	SiO_2	H_2O_{ad}	
Position (eV)	532.88	533.65	
Γ	0.18	0.18	
Gauss	1.4	1.4	
asymmetry	0	0	

A1. 2: Parameters used to fit O1s spectra of 1.5 nm Ni deposited on SiO_2/Si substrate, as grown, and annealed at 400 °C

CNs growth temperature (400 °C)		
Ni2p		
Name	Ni^0	Satellite
Position (eV)	852.67	858.65
Γ	0.21	0.21
Gauss	1.3	1.3
asymmetry	0.13	0.25
CNs growth temperature (500 °C)		
Name	Ni^0	Satellite
Position (eV)	852.56	858.48
Γ	0.21	0.21

Gauss	1.3	1.3
asymmetry	0.3	0.3
CNs growth temperature (600 °C)		
Name	Ni^0	Satellite
Position (eV)	853.02	859.26
Γ	0.21	0.21
Gauss	1.3	1.3
asymmetry	0.17	0.11
CNs growth temperature (700 °C)		
Name	Ni^0	Satellite
Position (eV)	852.98	859.20
Γ	0.21	0.21
Gauss	1.3	1.3
asymmetry	0.16	0.12

A1. 3: Parameters used to fit XPS data for Ni2p for the CNs grown using different growth temperatures using Ni as catalyst on SiO_2/Si substrate

CNs growth temperature (400 °C)		
C1s		
Name	Sp^2-C	CO
Position (eV)	284.03	285.34
Γ	0.08	0.08
Gauss	1.12	1.4
asymmetry	0.03	0.03
CNs growth temperature (500 °C)		
Name	Sp^2-C	CO
Position (eV)	284.03	285.27
Γ	0.08	0.08
Gauss	1.06	1.34
asymmetry	0.03	0.03
CNs growth temperature (600 °C)		
Name	Sp^2-C	C-O-C
Position (eV)	284.37	285.19
Γ	0.08	0.08
Gauss	1.14	1.4
asymmetry	0.03	0.03
CNs growth temperature (700 °C)		
Name	Sp^2-C	C-O-C
Position (eV)	284.3	284.88
Γ	0.08	0.08
Gauss	0.96	0.81
asymmetry	0.03	0.03

A1. 4: Parameters used to fit XPS data for C1s for the CNs grown using different growth temperatures using Ni as catalyst on SiO_2/Si substrate

As grown (Fe2p)			
Name	Fe^{2+}	Fe^{3+}	
Position (eV)	710.24	711.98	
Γ	0.67	0.67	
Gauss	1.4	1.4	
asymmetry	0	0	
After annealing at 600 °C			
Name	Fe^{0}	Fe^{2+}	Fe^{3+}
Position (eV)	707.3	710.24	711.3
Γ	0.67	0.67	0.67
Gauss	1.4	1.4	1.4
asymmetry	0.42	0	0

A1. 5: Parameters used to fit Fe2p spectra of 1.5 nm Fe deposited on SiO_2/Si substrate, as grown, and annealed at 600 °C

As grown (Fe2p)				
Name	Fe^{2+}	Fe^{3+}	Fe^{3+} ions on the surface	
Position (eV)	710.76	711.2	714.06	
Γ	0.67	0.67	0.67	
Gauss	1.4	1.4	1.4	
asymmetry	0	0	0	
After annealing at 600 °C				
Name	Fe^{0}	Fe^{2+}	satellite	Satellite
Position (eV)	706.62	709.74	711.18	712.88
Γ	0.67	0.67	0.67	0.67
Gauss	1.18	1.4	1.4	1.4
asymmetry	0.46	0	0	0

A1. 6: Parameters used to fit Fe2p spectra of 1.5 nm Fe deposited on Al_2O_3/Si substrate, as grown, and annealed at 600 °C

Fe2p			
CNTs growth temperature (600 °C)			
Name	Fe^{0}	Fe^{2+}	Fe^{3+}
Position (eV)	706.6	710	711.9
Γ	0.67	0.67	0.67
Gauss	1.4	1.4	1.4
asymmetry	0.27	0	0
CNTs growth temperature (700 °C)			
Name	Fe^{0}	Fe^{2+}	Fe^{3+}
Position (eV)	706.9	710.3	711.9
Γ	0.67	0.67	0.67
Gauss	1.4	1.4	1.4
asymmetry	0.27	0	0

A1. 7: Parameters used to fit XPS data for Fe2p for the CNTs grown using different growth temperatures using Fe as catalyst on SiO_2/Si substrate

C1s			
CNTs growth temperature (600 °C)			
Name	**Sp^2**	**Sp^3**	**C-O**
Position (eV)	284.16	285.21	286.01
Γ	0.08	0.08	0.08
Gauss	0.98	0.8	1.3
asymmetry	0.03	0.03	0.03
CNTs growth temperature (700 °C)			
Name	**Sp^2**	**Sp^3**	**C-O**
Position (eV)	284.16	285.21	286.01
Γ	0.08	0.08	0.08
Gauss	0.98	0.8	1.3
asymmetry	0.025	0.03	0.03

A1. 8: Parameters used to fit XPS data for C1s for the CNTs grown using different growth temperatures using Fe as catalyst on SiO$_2$/Si substrate

C1s		
CNTs growth temperature (600 °C)		
Name	**Sp^2**	**Sp^3**
Position (eV)	284.012	284.931
Γ	0.08	0.08
Gauss	1	1.4
asymmetry	0.03	0.03

A1. 9: Parameters used to fit XPS data for C1s for the CNTs grown using different growth temperatures using Fe as catalyst on Al$_2$O$_3$/Si substrate

O1s			
CNTs growth temperature (600 °C)			
Name	**HO-C=O**	**C=O**	**C-O**
Position (eV)	530.82	531.18	533.54
Γ	0.18	0.18	0.18
Gauss	1.5	1.5	1.5
asymmetry	0	0	0

A1. 10: Parameters used to fit XPS data for O1s for the CNTs grown using different growth temperatures using Fe as catalyst on Al$_2$O$_3$/Si substrate

100 nm WO_x film grown by DCMS				
As grown (W4f)				
Name	W^0	W^{4+}	W^{6+}	Satellite
Position (eV)	30.99	31.97	35.16	36.99
Γ	0.11	0.11	0.11	0.11
Gauss	0.92	0.99	1.3	1.4
asymmetry	0.05	0	0	0
After annealing at 600 °C				
Name	W^0	W^{4+}	W^{6+}	Satellite
Position (eV)	30.96	32	35.06	36.46
Γ	0.11	0.11	0.11	0.11
Gauss	0.93	1.03	1.3	1.4
asymmetry	0.05	0	0	0

A1. 11: Parameters used to fit W4f spectra of 100 nm tungsten deposited on Si substrate, as grown, and annealed at 600 °C

O1s			
As grown			
Name	**WO_x**	**OH**	**$H_2O_{ad\ atom}$**
Position (eV)	530.33	531.26	533.78
Γ	0.18	0.18	0.18
Gauss	1.4	1.4	1.4
asymmetry	0	0	0
After annealing at 600 °C			
Position (eV)	530.33	531.26	533.44
Γ	0.18	0.18	0.18
Gauss	1.4	1.4	1.4
asymmetry	0	0	0

A1. 12: Parameters used to fit O1s spectra of 100 nm tungsten deposited on Si substrate, as grown, and annealed at 600 °C

100 nm WO_x film grown by DCMS				
As grown (W4f)				
Name	W^{2+}	W^{5+}	W^{6+}	Satellite
Position (eV)	31.4	34.74	35.43	41.08
Γ	0.11	0.11	0.11	0.11
Gauss	0.80	1.4	1.05	1.4
asymmetry	0.05	0	0	0

A1. 13: Parameters used to fit W4f spectra of 100 nm tungsten oxide deposited on Si substrate

O1s		
As grown		
Name	**WO_x**	**OH**
Position (eV)	530.6	531.7
Γ	0.18	0.18
Gauss	1.4	1.4
asymmetry	0	0

A1. 14: Parameters used to fit O1s spectra of 100 nm tungsten oxide deposited on Si substrate

WO_x Nanoclusters deposited via PMCS					
In-situ (W4f)					
Name	W^{2+}	W^{3+}	W^{4+}	W^{5+}	W^{6+}
Position (eV)	31.2	32.49	33.89	35.31	36.5
Γ	0.11	0.11	0.11	0.11	0.11
Gauss	1.22	1.32	1.4	1.4	1.27
asymmetry	0.05	0	0	0	0
After air exposure for 6 months					
Name	W^{5+}	W^{6+}			
Position (eV)	35.51	36.45			
Γ	0.11	0.11			
Gauss	1.24	0.8			
asymmetry	0	0			

A1. 15: Parameters used to fit W4f spectra of tungsten oxide deposited on Si substrate via PMCS, in-situ and after air exposure for 6 months